POLITECNICO DI TORINO

Collegio di Ingegneria Chimica e dei Materiali

Master of Science Course
in Materials Engineering for Industry 4.0

Master of Science Thesis

Cellulose acetate as novel precursor to synthesize laser induced graphene

Tutors

University Tutor
Prof. Andrea Lamberti

External Tutors
Prof. Javier Martínez Rodrigo
Prof. Yu Kyoung Ryu

Candidate

Angelica Bisceglie

October 2024

To my family and my love,

who have always believed in me,

even when I didn't.

Acknowledgement

I would like to dedicate this section to all those who have supported me throughout my thesis project.

My sincere gratitude goes to Prof. Javier Martinez for providing me with the opportunity to conduct my project within the exceptional environment of ISOM, and to Prof. Andrea Lamberti for his guidance and support throughout my thesis work.

My heartfelt thanks go to Prof. Ryu for believing in my ideas, for her unwavering support, assistance, and positivity, for always being available, and for imparting to me the fundamental principles of scientific rigor.

A sincere and profound thank you to Dr. Luisa Baudino and Dr. Pietro Zaccagnini for their kindness and availability, as well as for welcoming and guiding me from the very first days in the DISAT laboratories.

I would also like to express my gratitude to Dr. Andrés Velasco, who mentored and supported me in the initial stages of my thesis, sharing his passion and knowledge.

My thanks also extend to the technical staff at ISOM: to Manu for his patience, especially during the early stages of the project, and to Eliram and Jesus for their constant assistance. Special thanks to Oscar and Fernando for their ongoing readiness to help.

Finally, my most sincere appreciation goes to Prof. Marco Sangermano. Thank you for guiding me through every step of this Erasmus experience and for your constant help and support. Your guidance was essential in allowing me to fully and peacefully experience one of the most enriching periods of my life, both professionally and personally.

Abstract

Laser-induced graphene (LIG) is a three-dimensional porous graphene-like material, rapidly synthesized by directly irradiating carbon-rich precursors. Its simple production process, time efficiency, eco-friendliness and low cost have made LIG and its derivatives highly attractive for a wide range of applications. The increasing need to reduce environmental impact, alongside the urgent demand to drastically cut CO_2 emissions, has driven efforts to promote a circular economy, encouraging the exploration of sustainable materials and innovative processes. Biodegradable materials derived from natural resources, such as lignocellulosic materials, are being investigated for the production of LIG, offering a promising opportunity to mitigate plastic pollution, especially in advanced technological applications like energy storage. In alignment with the United Nations Sustainable Development Goals (SDGs), particularly SDG 7 (Affordable and Clean Energy) and SDG 13 (Climate Action), this thesis focuses on converting cellulose acetate into LIG and using the resulting material as electrodes for supercapacitors. This approach promotes the use of environmentally friendly materials and provides a green alternative for future energy systems.

This work initially examines the effects of lasing parameters on Kapton®, with a successive optimization of focal plane distance, laser power, and scanning speed for cellulose acetate (CA). The materials generated from the lasing process were characterized using Raman spectroscopy, SEM imaging, and sheet resistivity measurements via the Van der Pauw method, as well as static sessile drop tests. Once optimal conditions for producing high-quality CA-LIG were identified, proof-of-concept supercapacitors were fabricated and electrochemically characterized using cyclic voltammetry (CV) and galvanostatic charge-discharge (GCD) measurements.

While this work underscores the potential of cellulose acetate-derived LIG for sustainable energy storage, further refinement of laser parameters and device architecture is required to minimize resistive losses and enhance overall efficiency.

Index

1. Introduction

The continuous use of fossil fuels and other non-renewable energy sources has led to numerous undesirable consequences. Fossil fuels - coal, oil, and gas - are by far the largest contributors to global climate change, accounting for over 75% of global greenhouse gas emissions and nearly 90% of all carbon dioxide emissions [1].

Greenhouse gas emissions are rapidly accelerating global warming, disrupting weather patterns, and posing significant risks to all forms of life on Earth [1]. There is an urgent need to slow and reduce them to combat climate change. Scientific consensus suggests limiting global temperature rise to 1.5°C above pre-industrial levels to avoid severe impacts. The Earth is already 1.1°C warmer than in the late 1800s, with emissions still rising [2]. Under the Paris Agreement [3], countries aim to keep warming well below 2°C, ideally 1.5°C, by cutting emissions 45% by 2030 and achieving net zero by 2050 [2,4].

Global economic growth drives rising energy demand, making emission reduction challenging. Renewable energy sources, such as solar and wind, are essential for lowering emissions. However, their intermittent nature necessitates efficient storage solutions to ensure a stable and reliable energy supply, allowing for a perfect match between energy generation and energy consumption [5].

Supercapacitors, known for their high power, rapid charge and discharge capabilities and long cycle life [6], are emerging as a key energy storage technology. They have garnered increasing interest in fields requiring long lifetime and fast charge/discharge rates, such as biomedical and sensing applications [6], where an energy storage device can power bio, physical, or chemical sensors. However, their low energy density is a major drawback, driving extensive research to enhance their charge storage capabilities. The performance of supercapacitors mainly depends on the properties of the electrodes material, such as porosity, hydrophilicity, reactive sites and chemical stability, as well as on the chosen electrolyte. Consequently, the integration of advanced nanostructured materials like graphene has significantly enhanced the performance of these energy storage devices [7].

Graphene, a single layer of carbon atoms arranged in a hexagonal lattice, exhibits exceptional properties, including high electrical conductivity, mechanical strength, and thermal stability [8]. Its application in energy storage devices, particularly supercapacitors,

has garnered significant attention. In fact, graphene and its derivatives have been shown to improve the energy density and efficiency of supercapacitors [9]. Research into graphene synthesis has evolved to prioritize methods that are both economically and environmentally sustainable [10]. A breakthrough in this field was the discovery of laser induced graphene (LIG), where a laser is used to convert polymeric precursors into graphene, eliminating the need for expensive and hazardous processes. Yet, the most commonly used precursors for LIG are synthetic polymers.

Recent advancements have focused on applying LIG technology to green substrates derived from renewable resources with minimal environmental impact [11,12]. This approach aligns with the global push towards sustainable materials and processes. On the other hand, the European Union is updating its legislation on waste management to promote a shift to a more sustainable model known as *circular economy*, a type of production and consumption that involves reusing, repairing and recycling existing materials and products as long as possible [13].

Cellulose acetate (CA) is a biodegradable material derived from cellulose, one of the most abundant organic polymers on Earth. Despite its renewable origins, used and unused filters made of CA fibers may take over a decade to decompose and are a significant contributor to marine pollution, accounting for nearly 10% of the total plastic waste in marine environments, primarily due to their use in cigarette filters [14-16]. The repurposing of used CA for advanced technological applications is of general interest, designing a path for a new possible way to upcycle this waste material.

The primary objective of this thesis was to develop and optimize the fabrication of laser induced graphene from cellulose acetate, focusing on achieving the optimum microstructure and material quality. To do this, the impact of lasing parameters was initially studied on another well-documented substrate, a polyimide commercialized as Kapton®. The second goal was to explore the use of CA-based LIG electrodes in energy storage applications. A proof-of-concept supercapacitor was fabricated, and its electrochemical performances were evaluated in different configurations and electrolyte solutions.

Chapter 2 provides a review of the state of the art, spacing from the materials to the applications. It presents graphene and graphene-derived materials, along with their properties and how these properties depend on the synthesis processes. The fundamentals of

laser induced graphene writing are then presented, including its mechanism and parameters. The evolution from synthetic to green precursors is discussed, with a particular focus on paper and cellulose acetate. Finally, an overview of the main applications of laser induced graphene is given, with a focus on supercapacitors.

Chapter 3 details the main techniques used during this thesis, both for the fabrication of materials and devices, as well as their characterization. Special attention is given to the laser-writing technique and the definition of the variation of the focal plane, as it is a crucial parameter studied for obtaining CA-based LIG.

Chapter 4 presents the results, divided into three main parts. The first part concerns the preliminary studies conducted on the well-known Kapton® substrate, a crucial step before moving on to cellulose acetate. The second part focuses on the optimization process for obtaining LIG from cellulose acetate. The final part presents the results obtained by the supercapacitor.

Chapter 5 summarizes the conclusions and proposes future work to further optimize the electrode material and enhance the performances of the device.

2. State of the art

Graphene, renowned for its exceptional electrical, mechanical, and thermal properties, has spurred significant interest alongside its derivatives, such as graphene oxide and reduced graphene oxide [17,18]. The evolution of graphene synthesis has progressed from traditional methods like mechanical exfoliation and chemical vapor deposition to innovative techniques. Among these, laser induced graphene (LIG) stands out, using localized heat from a laser beam to transform carbon precursors into graphene. This method's efficiency is influenced by various parameters, including laser power and precursor type. Recent advancements focus on green precursors, more specifically lignocellulosic materials [19], aiming to make the process more eco-friendly. The resultant LIG can find applications in diverse areas, including energy storage, sensors, electronics, and environmental remediation [20], highlighting its potential to drive future technological advancements.

2.1 Graphene and graphene-like materials

One of the exceptional peculiarities of carbon is its ability to exhibit a broad range of metastable phases that can be formed under near-ambient conditions, along with their extensive domains of kinetic stability [21].

Carbon-based materials and some of its most famous allotropes have been used for several purposes since prehistoric times. Diamond, consisting of sp^3 hybridized carbon atoms arranged in three-dimensional tetrahedral cells, has been the benchmark for maximum hardness on the Mohs scale for nearly two centuries. Graphite, a dense tridimensional stack of parallel layers of sp^2 carbon atoms, has been known since ancient days and is still used as drawing tool and as solid lubricant.

Our knowledge and understanding on sp^2-hybridized carbon has received an incredible boost in the last four decades. New carbon nanostructures have been discovered and further explored, attracting increasing attention from various fields of engineering and scientific research, from nanoelectronics and drug delivery to electrochemistry and sensing technologies [21]. The first nanostructure to be discovered in 1985 by H. W. Kroto *et al*. was C_{60}, more usually known as *fullerene*, a zero-dimensional (0D) nanoparticle [22]. Less than ten years later, in 1991, S. Iijima reported the synthesis of a novel form of finite carbon

structure, the carbon nanotubes (CNTs) [23], a one-dimensional (1D) nanomaterial that consists in a small sheet of sp^2 carbon atoms folded onto itself. But it was only twenty years ago that the planar, two-dimensional (2D) graphene sheet was isolated for the first time by Geim and Novoselov [24]. However, the bidimensional structure had been mathematically theorized many years before [25] and then used to describe the properties of many carbon-based materials [24]. Since then, the building block of graphite has attracted considerable attention.

The thinnest material known, graphene consists of a single layer of sp^2 hybridized carbon atoms arranged in a tightly packed, two-dimensional (2D) honeycomb lattice. The average interatomic distance is 1.42 Å, contributing to an incredibly large surface area of approximately 2630 $m^2 g^{-1}$ [8, 20, 26]. Each carbon atom forms three σ-bonds with adjacent atoms, creating hexagonal structures due to the three sp^2 electrons. This configuration imparts exceptional mechanical strength, with a breaking strength of 42 N/m and a Young's modulus of approximately 1 TPa [27]. The out-of-plane p_z electron forms a π-bond perpendicular to the plane, allowing it to easily hop between neighboring atoms, overcoming an energy barrier of 3 eV [28]. This unique structure endows single-layer graphene with intriguing properties, including chemical inertness, excellent in-plane thermal conductivity (~5000 W $m^{-1} K^{-1}$) [29], zero band-gap and high electrical conductivity [8, 20, 28].

Researchers have been focusing on exploring how to tune these properties with different synthesis techniques, introducing structural changes, defects and impurities [30, 31]. This has led to a new family of 3D graphene materials, often called *graphene-like materials* [31], *disordered graphene*, *porous graphene* [32], where the final aim is to avoid the restacking of graphene layers during the application. Depending on the dimensional scale, these architectures can be classified either as 3D graphene macrostructures, which are >100 μm in one or more dimensions or 3D graphene microstructures, with a size of <100 μm in all directions [31].

2.1.1 Traditional synthesis methods

The synthesis of graphene materials conventionally relies on either a bottom-up or a top-down approach. The bottom-up strategy uses chemical pathways to grow monolayer graphene from individual carbon atoms on a catalyst surface, allowing for highly controlled synthesis processes. Among the most relevant techniques available in bottom-up production

are chemical vapor deposition (CVD), epitaxial growth, and thermal pyrolysis. These methods fallow for the production of graphene with almost no defects and superior quality. In contrast, the top-down approach involves the breakdown of multi-layered graphite to isolate a graphene monolayer and the reduction of raw graphite. This technique is generally simpler and more cost-effective but tends to yield materials with a higher defect density, lower homogeneity, and greater difficulty in obtaining single layers [33, 34]. The most established top-down techniques include mechanical exfoliation, liquid-phase exfoliation (LPE), solid-phase exfoliation, and the chemical oxidation-reduction of graphite oxide (GO) [35].

Despite remarkable advancements and inherent advantages, both families of techniques face challenges, including the need for sophisticated infrastructures, demanding operating conditions, costly precursors or complex multi-step synthesis routes. These factors hinder their scalability for widespread commercial production. As a result, it is crucial to develop simple, cost-effective and scalable methods for producing and patterning graphene-like materials.

2.2 Laser induced graphene

A significant advancement in graphene synthesis was achieved with the development of laser-induced graphene (LIG), a bottom-up approach that directly converts carbon-based precursors into a 3D porous carbon structure through laser irradiation. LIG is formed by irradiating commercial polymeric films, transforming the substrate into a foam-like material composed of disordered graphene sheets that resemble graphene but lack long-range lattice order [36, 37]. The laser direct writing technique is a single-step, fast, and scalable process that does not require masks, catalysts, or chemicals, making it a controllable, non-toxic, and flexible method for manufacturing. This transformation occurs via a rapid photochemical and thermal-pyrolytic process, leading to the liberation of gases responsible for the porous structure. As a result, LIG exhibits excellent porosity, high chemical resistance, and good thermal and electrical conductivity. These features make it an ideal candidate for a wide range of applications, including biochemical [38-40] and chemical sensors [26, 41], supercapacitors [42-44] and microfluidic devices [45, 46].

2.2.1 Laser induced graphene: synthesis mechanisms

Multiple parameters play a critical role in the efficient transformation of a polymeric substrate into LIG, with the choice of precursor material and the laser specifications being particularly influential. When the laser beam is focused on a suitable organic substrate, it must generate a localized thermal energy sufficient to induce the conversion of the polymer surface into a non-uniform, porous, graphene-like architecture. The underlying photophysical mechanisms governing this transformation can be comprehensively described by two primary and interrelated models: the photochemical and photothermal effects [19, 47].

Photothermal effects occur as a result of localized heat gradients generated by the laser beam, causing the substrate to reach extremely elevated temperatures (exceeding 2000 °C). This intense heating facilitates bond cleavage, molecular rearrangements, and, under excessive exposure, can lead to the complete ablation of the exposed substrate, as illustrated in *Figure 2.1(a)*. The onset of photothermal effects is primarily determined by the operational parameters of the laser, including laser power, pulse repetition rate, and pulse duration, which collectively regulate the thermal profile of the process [19]. In contrast, photochemical effects are initiated through electronic excitation by incident photons possessing sufficient energy to induce isomerization, bond cleavage, and formation, without significantly raising the substrate temperature, as depicted in *Figure 2.1(b)* [10]. The efficiency of bond breaking via photochemical effects is largely influenced by the laser wavelength and its interaction with specific bonds present within the chemical structure of the precursor material [19].

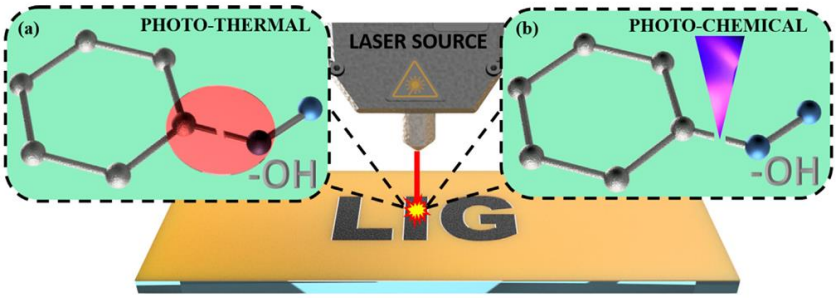

Figure 2.1: *Laser scribing on a polymeric substrate utilizing photothermal and photochemical effects: (a) thermal-induced breakage of C - OH bonds; (b) photon-induced dissociation of C - OH bonds [10].*

In LIG synthesis, both photochemical and photothermal mechanisms can contribute to breaking and rearranging bonds, depending on the laser source's wavelength and irradiation parameters. The role of photochemical processes in LIG synthesis remains uncertain, hence it is believed that photothermal processes play a major role in carbonization and graphitization. The generated temperature gradients not only complement the breaking of bonds but also speed up the reorganization of atomic vacancies, improving the rearrangement of carbon atoms and, consequently, promoting graphitization. When the laser radiation hits the substrates, it must generate phonons with enough energy to break weaker chemical bonds, resulting in microablation and release of volatile compounds. This causes ionization and plasma discharge, evident through bright flashes on the irradiated substrate. This plasma flash acts as a barrier to further laser penetration, generating highly localized temperatures that drive carbonization and graphitization [19]. During the process, the cleaved dissociated sp^3 carbon bonds undergo amorphization [37], condensation and aromatization to form sp^2 carbon-rich lattice domains, eventually leading to the formation of LIG [11, 19].

Different laser sources have been used in literature, from ultraviolet (UV) to infrared (IR) wavelengths, as shown in *Figure 2.2*. UV lasers (200-400 nm) have the highest photon energy, higher than the dissociation energies of the chemical bonds of several substrates, which can lead to the cleavage of bonds before their rearrangement in graphene-like structures. Their energy is concentrated in a small volume of the material, thus giving a small amount of transformed thickness in the range of some μm [47]. CO_2 lasers emit lower-energy photons in the infrared range, with a 10.6 μm wavelength strongly absorbed by the C-C bonds in carbon precursors [48], and are less effective at directly breaking covalent bonds. However, they generate substantial heat in the substrate, triggering thermochemical reactions that ultimately lead to breaking covalent bonds and to graphitized layers from some tens to hundreds of μm [10, 47]. Therefore, it is possible to state that the longer IR wavelengths of CO_2 lasers are more likely to induce photothermal processes while shorter UV wavelengths trigger photochemical effects. For this reason, CO_2 lasers are the most commonly used.

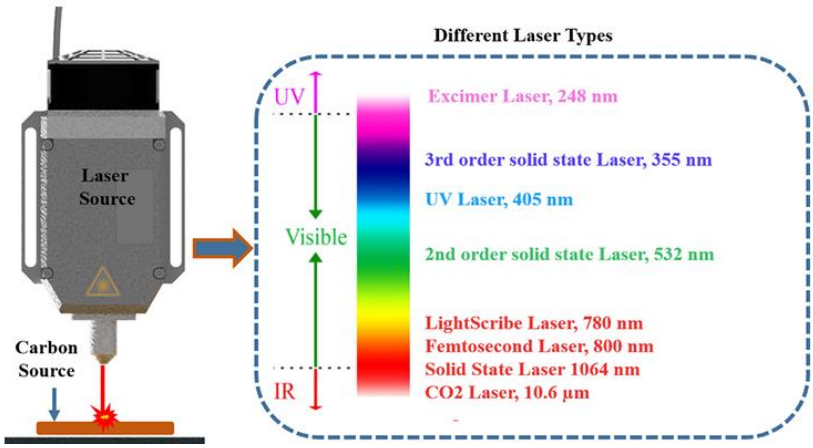

Figure 2.2: *Representation of the different laser types used in the fabrication of LIG-based structures [10].*

2.2.2 Precursors

Synthetic precursors

The pioneering synthesis of LIG was conducted in 2014 by J. Lin *et al.* [36] on a film of polyimide (PI), specifically poly-oxydiphenylene-pyromellitimide, commercially available with the name "Kapton®" by DuPont™. The chemical structure of PI, depicted in *Figure 2.3*, is particularly conducive to LIG formation due to its aromatic sp^2 carbon content, which facilitates the creation of hexagonal graphene structures. Additionally, PI exhibits high thermal and chemical stability, enabling it to endure the thermal gradients the substrate experiences during the lasing process [10, 19].

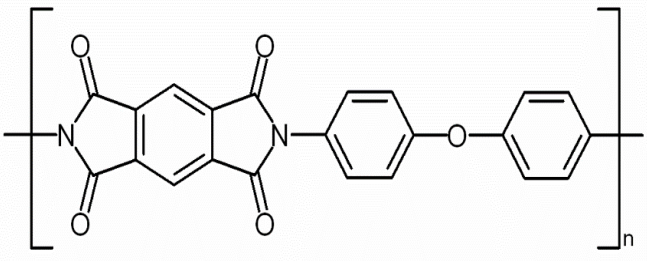

Figure 2.3: *Chemical structure of poly-oxydiphenylene-pyromellitimide (PI), commercially known as Kapton® (DuPont™).*

Since then, efforts have been undertaken to widen the spectrum of carbon-based materials capable of producing LIG, broadening the technological applications of the resultant structures. The fundamental prerequisite to obtain LIG was thought to be the content of aromatic repeating units. For this reason, subsequent studies have indicated the potential for

utilizing phenolic resins (PRs) as viable substrates. PRs demonstrate elevated chemical and thermal stabilities, and their physicochemical characteristics can be readily adjusted due to their easy synthesis from appropriately selected formaldehydes and phenols [49-50]. Other polymeric materials that have been successfully transformed into LIG include para aramid fabrics, marketed as "Kevlar®" by DuPont™, and poly(ether) sulfone (PES) films. The former shows excellent mechanical properties, while the latter is notably easy to prepare due to its excellent solubility in several organic solvents [51]. Additionally, LIG was derived from S1818 positive photoresist, an aromatic thermoplastic polymer commonly utilized in traditional photolithography. This enabled precise control over morphology and achieved micron-scale feature resolution [52].

Green precursors: issues and solutions

In recent years, researchers have started to shift towards the use of more sustainable LIG precursors, thus addressing environmental challenges. Since its discovery, LIG has been synthesized from various green precursors, including wood, cork, potato skin, coconut shells, and pomelo peels [12]. Nearly all bio-derived precursors evaluated thus far for LIG production are lignocellulosic materials [11, 53], comprising lignin, whose chemical structure is shown in *Figure 2.4*, cellulose, depicted in *Figure 2.5*, and hemicellulose.

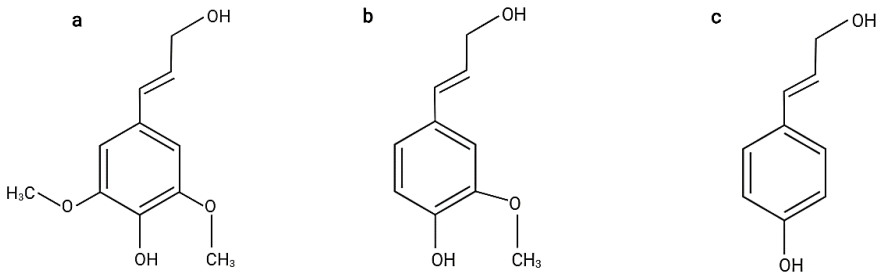

Figure 2.4: *Chemical structure of the three precursors (lignols) of lignin: a) sinapyl alcohol, b) coniferyl alcohol, c) paracoumaryl alcohol [54].*

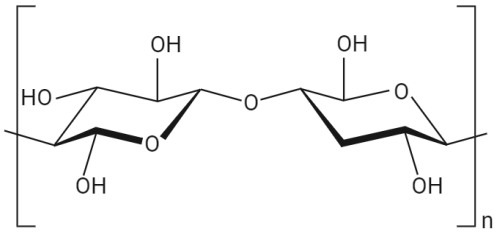

Figure 2.5: *Chemical structure of cellulose [54].*

Variations in the relative composition among different natural raw materials impact the carbonization processes and their conversion success [11]. Lignin, for example, contains numerous benzene rings covalently bonded to other functional groups, forming an amorphous, branched aromatic polymer. This plays a crucial role in graphene formation: direct conversion of coconut shells [12], wood [55] and cork [56], all rich in lignin, has been accomplished without the need for substrate material pretreatment. However, lignin/cellulose-based precursors generally exhibit lower thermal and fire stability compared to synthetic polymeric substrates. Therefore, pretreatment of the precursor is needed to prevent complete ablation upon laser irradiation.

In particular, paper stands out as a particularly attractive option due to its versatility, low cost, lightweight nature, and biodegradability. Initially, LIG was produced from paper by soaking it in a Mo^{2+}- containing hydrogel and then performing a single pass with a CO_2 laser. This process resulted in a porous 3D structure with a sheet resistivity of less than 50 Ω/sq, suitable for various devices [57].

An additional step to further reduce sheet resistivity and improve graphene quality has been taken by pretreating the precursors with fire retardants (FR) and subjecting them to multiple raster engraves and/or a defocus of the laser. In this way, paper and other materials rich in polysaccharides such as potato skins and muslin cloth have produced good-quality LIG [12, 58-59].

In the specific case of paper, the incorporation of a fire retardant, such as phosphate- or boron-based compounds, induces phosphorylation or borylation of cellulose. This modification catalyzes dehydration and oxygen elimination reactions within the cellulose, inhibiting its decomposition into levoglucosan and other volatile compounds under rapid heating in ambient conditions [60]. Consequently, during the first irradiation step with a defocused laser, an amorphous char rich in aromatic content is produced (*Figure 2.6*) [61]. This amorphous char is then transformed into graphene through a second laser pass conducted near the focal plane. Through this approach a sheet resistivity of 30 Ω/sq was achieved, and the resulting LIG could be used as a mechanical sensor [59]. Another study confirmed the two-step mechanism, again using defocused and focused irradiation after treating the sample with a phosphate-based fire retardant. The same strategy was

successfully applied to transform Xylan film into LIG [62]. This suggests that other green polymers with structures similar to cellulose could also be converted into LIG.

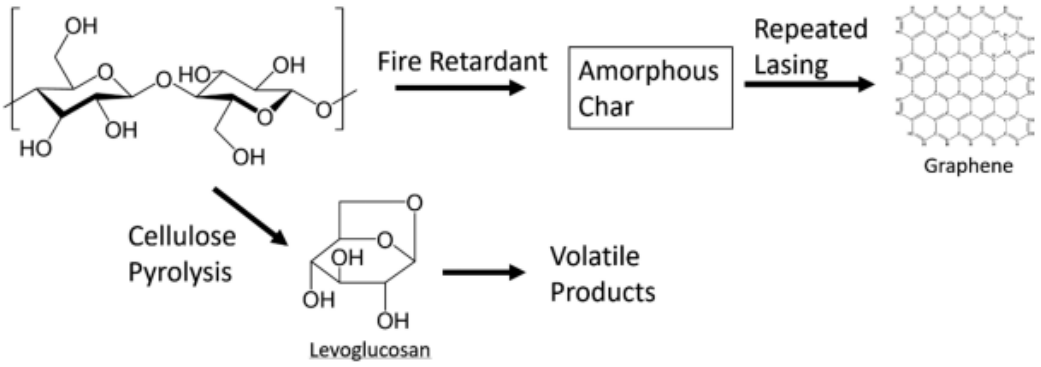

Figure 2.6: *Diagram illustrating the comparison between the laser processing of untreated paper undergoing pyrolysis and fire-retardant-treated paper resulting in the formation of amorphous char and LIG through multiple passes [61].*

Cellulose acetate (CA), a cellulose ester derived from the partial acetylation of cellulose, showed in *Figure 2.7*, is widely used in various industrial applications, including eyewear frames, cigarette filters, and timing layers in photography. However, the waste generated from CA-based products is poorly biodegradable, posing significant environmental challenges.

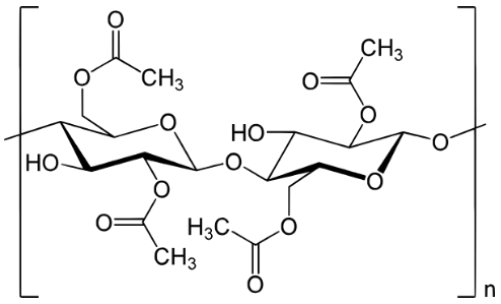

Figure 2.7: *Chemical structure of cellulose acetate (CA) [54].*

Research has already shown that CA can be effectively used in the synthesis of carbon nanotubes (CNTs) through a one-pot process, where the carbonization occurs in a nitrogen atmosphere allowing the material to crosslink with a glass substrate [63]. Furthermore, graphene can be produced by annealing a nickel foil coated with a CA laminated film in a furnace under an argon flow, and subsequently transferring the graphene onto various substrates [64]. Additionally, it was demonstrated that CA microspheres can be converted

into activated carbon using activation agents such as KOH or H_3PO_4, followed by a carbonization process. The resulting porous carbons have been successfully used as electrode material in symmetric double-layer supercapacitors [65]. Moreover, literature has documented the successful transformation of CA into monolayer graphene through a custom chemical vapor deposition system. These advancements highlight the potential of CA as a versatile and sustainable precursor for producing LIG and other carbon-based materials [66].

2.2.3 Operational parameters

LIG synthesis is governed by lasing parameters, specifically fluence, power, scanning speed, operational distance and lasing environment. These parameters together control the interaction of the beam with the polymer substrate and hence dictate the efficiency and quality of the conversion process from polymer to graphene.

Fluence is defined as the optical energy density at the surface of the substrate, measured in J cm^{-2}. It determines the outcome of the irradiation process, affecting the resulting temperatures and energy necessary for carbonization and graphitization. Indeed, in order to obtain LIG, a fluence threshold has to be overcome. This factor depends from other operational variables, as is possible to see from *Equation (1)* [42]:

$$Fluence = \frac{P}{u_x \cdot s} \tag{1}$$

where P is the source power, u_x is the lateral scan speed and s is the beam diameter. Thus, by properly tuning the value of these constants, different morphologies may be obtained [67-68], as shown in *Figure 2.8*.

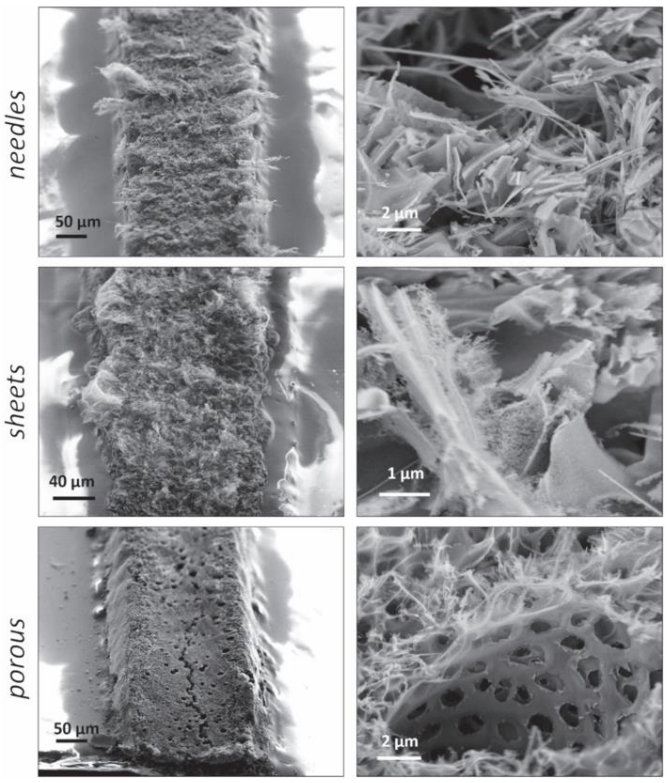

Figure 2.8: *FESEM images at low (left) and high (right) magnification for samples produced under different lasing conditions. Power was tuned in different samples to avoid complete conversion. Needles, obtained at scan speed of 160 mm s^{-1} and frequency of 4 kHz; sheets, obtained at scan speed of 200 mm s^{-1}, and frequency of 4 Hz; porous, obtained at scan speed of 160 mm s^{-1}, and frequency of 20 kHz [68].*

Laser source power, which is the optical power of the laser beam measured in watts (W), determines the energy delivered onto the surface of the substrate and, consequently, the generated temperature ramp. In order to obtain LIG, the laser power must exceed a threshold to promote the necessary bond cleavage and reorganization, otherwise the irradiated area will maintain its insulating properties. Higher lasing powers lead to increased localized temperatures in the irradiated polymer, enhancing the breaking of the bonds and reducing the amount of oxygen in the final material, resulting in more extensive carbonization and graphitization; yet excessive laser powers lead to the degradation of the LIG [59].

Scanning speed plays an essential role in the spread of the irradiating energy. Fast scanning speeds can lead to a smaller interaction time between the laser and the material and decrease in the density of energy per unit area of the substrate, possibly resulting in incomplete carbonization or an unevenly patterned LIG structure. Slower speeds can increase the local

heating effect and enable proper carbonization and graphitization. However, too low speeds can cause ablation of the polymer substrate [19].

Operational distance (z) refers to the defocusing of the laser beam, resulting in a change in the spot size. The laser beam profile, determined by the optical set-up, dictates the spot size at various focal planes. In defocused irradiation, larger spot sizes spread the power over a wider area compared to the focal plane; however larger spot sizes generate superposition patterns between consecutive laser pulses. Consequently, the same irradiated area receives multiple laser pulses within a single raster cycle [19, 67].

Number of passes, a crucial factor for renewable substrates, allows for a significant enhancement of LIG derived from these sources. With multiple passes, the carbonaceous precursor is first converted into amorphous carbon and subsequently transformed into graphene. The amorphous carbon, consisting of sp^2 carbon clusters embedded in an sp^3 carbon matrix, selectively absorbs IR radiation while minimizing depolymerization or ablation [20].

The *lasing environment* can either be ambient atmosphere or a controlled atmosphere containing nitrogen (N_2), argon (Ar), or hydrogen (H_2). Controlling the atmosphere composition is vital for managing the degree of graphitization of specific substrates, thereby avoiding their combustion. A controlled atmosphere enhances the reducing action of laser writing by eliminating oxygen-containing groups through photothermal or photochemical effects, maintaining surface stability without introducing new carbon-oxygen bonds. In contrast, oxygen presence leads to increased volatile compound formation and porosity due to heightened oxidation and combustion [19]. LIG fabricated in Ar and H_2 atmospheres usually exhibits superhydrophobic behavior while the one prepared in presence of O_2 generally displays superhydrophilicity, as observable from the wettability tests reported in *Figure 2.9* [48, 69].

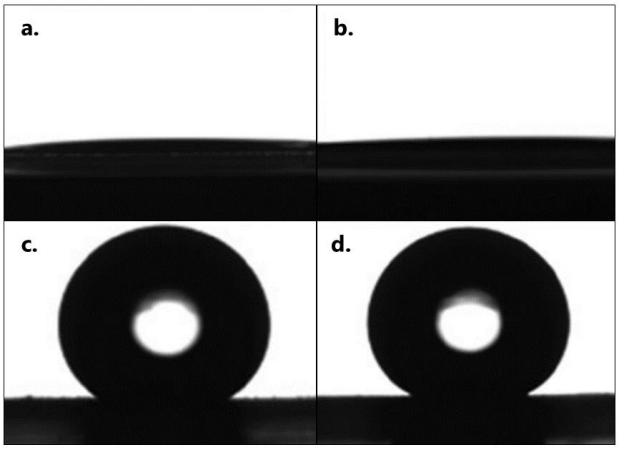

Figure 2.9: *Contact angle measurements on LIG surfaces prepared under different lasing atmosphere conditions: (a) Air, contact angle of 0°, (b) O_2, contact angle of 0°, (c) Ar, contact angle of 152°, (d) H_2, contact angle of 157°. Adapted from [69].*

To conclude, the localized heat generation in the substrate and thus the resulting extent and quality of the conversion from polymer to graphene-like material, are contingent upon the interaction of these parameters with the optical properties of the material, namely absorption, transmission, and reflection [47].

2.3 Supercapacitors and other applications

The laser scribing technique offers a selective, cost-effective, chemical-free, and maskless patterning technology that significantly reduces raw material usage and minimizes environmental impact. This versatile method is applicable across both academic and industrial settings. Additionally, the unique properties of laser induced graphene, compared to its bulk counterpart, graphite, create new opportunities for a variety of applications, from biosensor to physical sensors to energy harvesting and storage applications, as shown in *Figure 2.10*.

This section will provide an overview of the major fields of application for LIG, presenting literature examples for various uses. The energy-related applications are of particular interest in this thesis, especially the use of LIG in supercapacitors. Therefore, a more detailed description will be provided for this specific application.

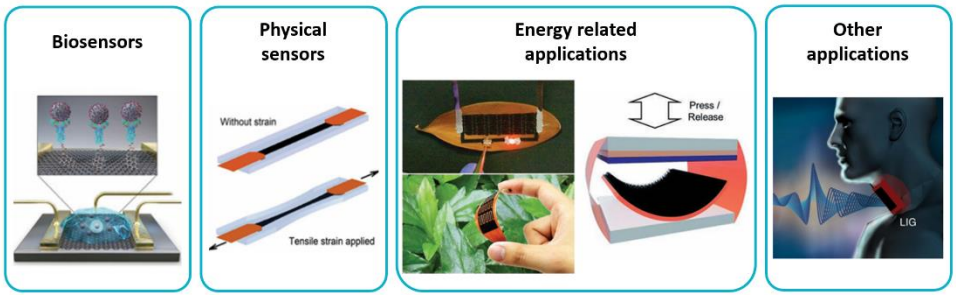

Figure 2.10: *Main fields of application for laser induced graphene include biosensors, such as the configuration of bio-FETs (field-effect transistors) [48]; physical sensors, exemplified by strain gauge sensors [48]; energy harvesting, storage and generation with supercapacitors and triboelectric nanogenerators (TENGs) among others [48]; and other uses like thermoacoustic actuators [70].*

2.4.1 Supercapacitors

Supercapacitors (SCs) are high-power energy storage devices that rely on the electrostatic-driven adsorption and desorption of electrolyte ions onto the electrode surface. As shown schematically in *Figure 2.11*, a SC consists of two electrically isolated electrodes connected through an electrolyte, which serves as ion-conducting medium. The charge storage process occurs at the interface between the electrode and the electrolyte. During charging, positive and negative charges accumulate on the respective electrodes. The ions in the electrolyte, both positive and negative, are attracted to the oppositely charged electrodes, accumulating at the surface. This process, governed by the laws of diffusion and electrostatic attraction, leads to the formation of an electric double layer [71].

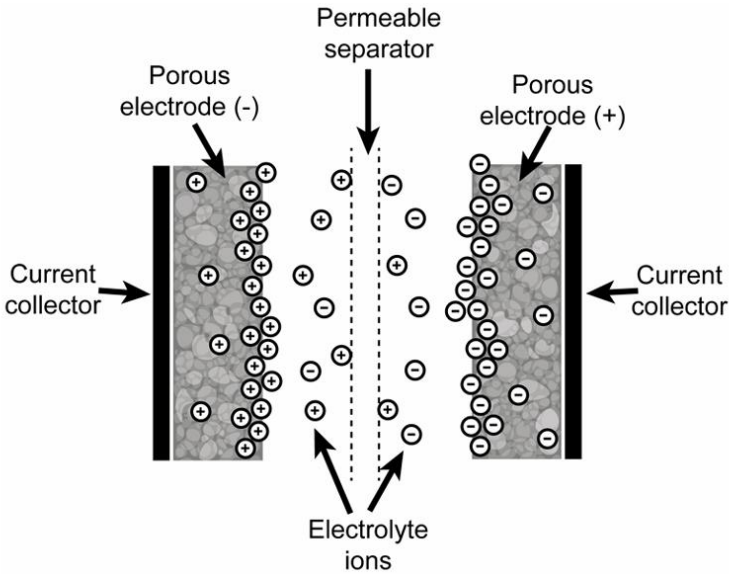

Figure 2.11: *Schematic drawing of a supercapacitor [72].*

As the surface becomes charged, ions in the electrolyte respond and reposition themselves to maintain electroneutrality. Initially, a layer of ions arranges close to the surface, forming a structure as thick as the ionic radius and the presence of solvent molecules allow. A layer of polarized solvent molecules covers the electrode surface, with some ions losing their solvation shell and becoming specifically adsorbed on the surface, forming the inner Helmholtz plane (IHP). Next, solvated ions, which are completely surrounded by solvent molecules, arrange as closely as possible on top of this inner layer, forming the outer Helmholtz plane (OHP). Beyond this compact Helmholtz layer, a second diffuse layer of ions is attracted to the surface, partially shielded by the first layer. *Figure 2.12* shows a schematic illustration of the ionic arrangement and the evolution of the potential.

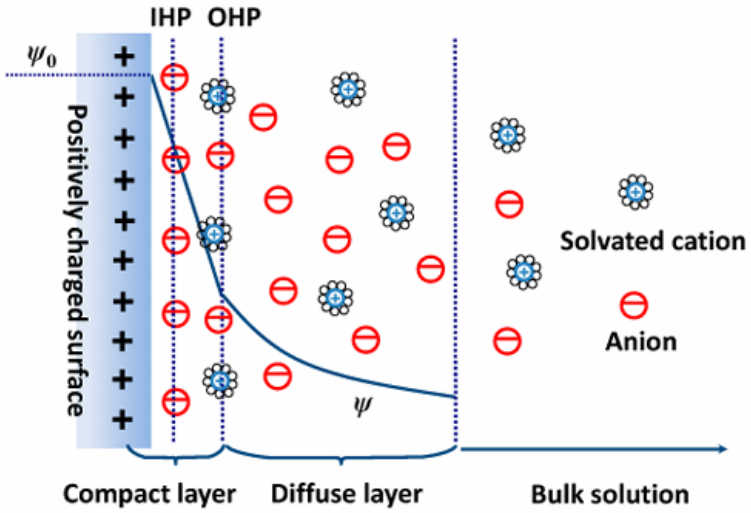

Figure 2.12: *Schematic illustration of the ionic arrangement in a double layer at the solid-liquid interface [73].*

The capacitance of these devices has two main components, namely the *Helmholtz capacitance,* which arises from the compact layers of the inner and outer Helmholtz planes (IHP and OHP), and the *diffuse layer capacitance,* which is due to the diffuse ionic arrangement in the bulk of the electrolyte. The typical structure of a SC consists of two electrodes, with their current collector, separated by a membrane soaked in the electrolyte. Based on the charge storage mechanism of the electrodes, three families of devices can be distinguished [74]:

- **Electrochemical Double-Layer Capacitors (EDLCs)**: two symmetric electrodes allow for an electrostatic charge storage mechanism characterized by the separation of charges

at the electrode-electrolyte interface. This process is very rapid, allowing a quick energy storage and release. The use of electrodes with a high surface area enables a large amount of charge accumulation at the double layer, providing high power density and long-life cycles. Carbon-based materials are the most common example for this kind of electrodes.

- **Pseudocapacitors (PCs)**: an active redox material on the electrodes surface undergoes a faradaic electron transfer process, which is confined to the surface without involving intercalation. This process involves one or more electrons and is characterized by being rapid, reversible, and surface-limited. Although pseudocapacitors may offer higher capacitance, they typically exhibit lower power density and reduced cycling performance. The diminished power density results from the inherently low electrical conductivity of both organic and inorganic pseudocapacitive materials. Moreover, the limited lifespan of pseudocapacitive electrodes arises from the relatively rapid degradation experienced by these materials during repeated electrochemical cycling. Common active redox materials used in pseudocapacitive electrodes include transition metal oxides and conductive polymers.
- **Hybrid supercapacitors (HSCs)**: the integration of both pseudocapacitive and electrochemical double-layer electrodes within an asymmetric device configuration leverages the advantages of both charge storage mechanisms [75]. These devices use the combined effects of redox reactions and electric double-layer capacitance, resulting in a synergistic enhancement of overall energy storage performance [43]. This hybridization leads to improved energy storage capabilities, exploiting the strengths of both mechanisms to optimize the performance of the final device.

Laser induced graphene supercapacitors

Graphene has been considered an ideal electrode material for EDLCs due to its large specific surface area and excellent electrical conductivity [17]. However, these properties deteriorate due to the aggregation and restacking of graphene sheets, producing a reduction in surface area and an increase in the interfacial resistance during fabrication. LIG obtained from polymeric films shows highly porous structures, superior electrical conductivity, and excellent crystallinity. Thus, these LIGs can be used directly as binder-free and flexible SC electrodes without additional metal current collectors [48].

LIG supercapacitors (SCs) have traditionally been assembled in a standard sandwich structure, as illustrated in *Figure 2.13 (a)*. In this design, both electrodes are fabricated as thin films and placed one on top of the other, separated by a membrane that allows for ion transfer while electrically isolating them. Alternatively, interdigitated electrodes (IDEs) offer a different configuration, as shown in *Figure 2.13 (b)*. In this design, the electrodes are fabricated in-plane as two sets of interlocking fingers with alternating polarity. The spatial separation in this geometry provides electrical isolation, eliminating the need for a separator membrane. This configuration enhances electrolyte accessibility by increasing the perimeter of the electrode area, thereby exposing more edges, particularly advantageous for layered materials like LIG. Additionally, IDEs improve ion mobility by removing the separation membrane and allowing a smaller, tunable distance between electrode polarities. This can be optimized for specific electrolyte/electrode systems, further enhancing performance [6, 76].

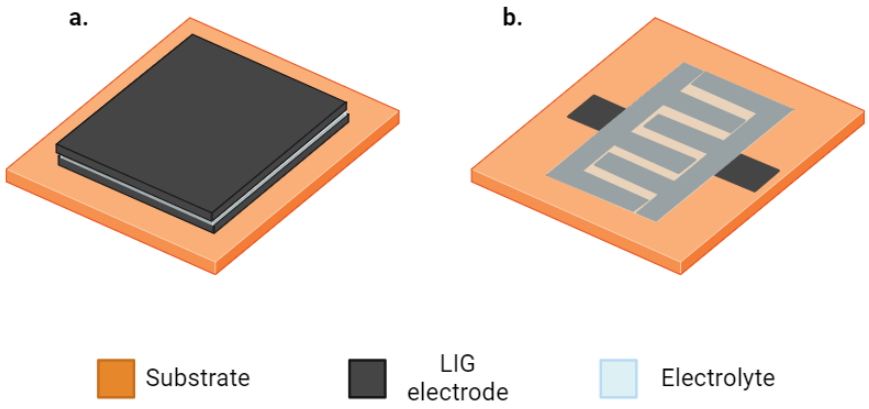

Figure 2.13: *Schematic drawing of the two possible supercapacitor configurations: (a) sandwich architecture, (b) interdigitated electrodes geometry.*

Electrolytes are a crucial element in supercapacitors as they penetrate the porous electrodes, forming interfaces and supplying ionic charges essential for energy storage. They must provide both anions and cations, significantly impacting the device performance. Electrolytes can be classified by their physical state (liquid, gel-like, or solid) or chemical nature, such as acidic (H_2SO_4), alkaline (KOH, NaOH), or neutral (Na_2SO_4) for aqueous types. Non-aqueous options include organic solvents and ionic liquids (ILs).

Aqueous electrolytes are characterized by high ionic mobility and conductivity. Despite their advantages, they have a limited voltage window of about one volt due to water splitting at higher voltages, resulting in lower energy density and electrical leakage. Gel electrolytes improve upon this by trapping water in a polymer matrix, enhancing cyclability and reducing leakage, though with slightly reduced conductivity and ionic mobility. Solid electrolytes exhibit this reduction more significantly. Non-aqueous electrolytes offer a broader voltage window, up to four volts, significantly boosting energy density. However, they require assembly in water-free environments and proper encapsulation due to stability concerns and reduced ionic conductivity. Their larger molecules also struggle to penetrate smaller pores [7].

2.4.2 Other energy related applications

LIG allows for 3D porous electrodes with high crystallinity, hierarchical porosity, large surface area and strong interfaces with the substrates. Unlike conventional electrodes, made by coating a metal current collector with a slurry of active materials, binders, and conducting agents, LIG-based electrodes eliminate the need for binders and conducting agents, thus simplifying the process, and reducing chemical waste.

In nanogenerators, thin LIG electrodes provide conductive channels for electric charges directly on the carbon substrates, ensuring excellent bonding characteristics [53, 77]. In triboelectric nanogenerators (TENGs), LIG effectively converts mechanical movement into electrical energy due to its high conductivity and 3D porous structure. Its direct fabrication on substrates like polyimide and paper simplifies TENG manufacturing by avoiding costly vacuum or toxic wet processes [10-11, 48, 78].

In lithium-ion batteries (LIBs), LIG anodes offer high capacity and power characteristics, featuring increased defects, enlarged structures, and an open-pore structure that enhances ion transport during charging and discharging [79].

2.4.3 Sensors

LIG is an ideal candidate for *biosensing applications* due to its large surface area, high electron density, and optical transparency. LIG biosensors typically consist of a receptor layer of biomolecules and a transducing LIG layer that converts chemical interactions into measurable signals. In biofield-effect transistors (bio-FETs), LIG acts as a conductive

channel, with target biospecies binding altering the drain-source current, indicating their presence [80]. LIG large surface area is also advantageous for impedimetric biosensors, which detect changes in electrochemical impedance spectra (EIS) caused by biomaterial absorption [81].

Real-time monitoring of physical variables like pressure, strain, temperature, and humidity is essential in fields such as robotics, e-skin, healthcare, and IoT. The development of 3D porous LIG has enabled cost-effective fabrication of high-performance *physical sensors*. LIG-based flexible pressure sensors are crucial in biomedical applications, as pressure changes alter the sensing material's electrical properties [82]. Additionally, LIG is highly effective in strain sensing, where displacements between graphene layers alter the contact resistance, achieving greater sensitivity compared to traditional strain gauges [59, 83].

LIG-based sensors are extensively used also for detecting chemicals and quantifying their concentrations. The large surface area of this material offers more active sites for surface chemical reactions, resulting in high sensitivity and rapid response times. Various LIG-based *chemical sensors* have been developed to detect a wide range of chemicals. Also, LIG-based gas sensors have been developed enabling stretchable, wearable devices for detecting gaseous biomarkers and environmental hazards [10, 48].

2.3.4 Actuators and transducers

LIG has also been employed in intriguing applications such as electrothermal actuators and thermoacoustic transducers. In multilayered *electrothermal actuators*, LIG generates high temperatures through the Joule effect, causing structural deformation due to the significant thermal expansion mismatch with other materials [84]. For *thermoacoustic actuators*, LIG's high electrical and thermal conductivity is used: applying an AC voltage to the LIG pattern induces periodic Joule heating, resulting in the expansion and contraction of air, which produces sound waves [70].

3. Methods

The experimental work of this thesis was conducted in two main phases. The first phase, which involved the synthesis and characterization of the electrode material as well as the initial electrochemical tests, was carried out at ISOM (Instituto de Sistemas Optoelectrónicos y Microtecnología), a multidisciplinary research institute located at ETSIT-UPM (Universidad Politécnica de Madrid). The second phase of the project, focused on the electrochemical optimization of the devices, was conducted at the Department of Applied Science and Technology (DISAT) at Politecnico di Torino.

3.1 Fabrication

3.1.1 Fabrication of cellulose acetate membranes and films

Cellulose acetate (CA) was selected as an environmentally friendly substrate for producing laser induced graphene (LIG). Initially, efforts focused on producing CA films. The CA, with an average molecular weight (M_n) of approximately 30,000 and an acetyl content of 39.8 wt.%, was obtained in powder form from Sigma-Aldrich (USA) and used as received. Acetone served as the solvent, while phosphoric acid (H_3PO_4) was employed as both activator and fire retardant [59, 76]. The preparation of the films was done inside a clean room, in the chemical bench and the lithography room.

To fabricate CA films, solutions of varying concentrations ranging from 0.3% to 1.1% (w/v) in 0.2% (w/v) increments were prepared by dissolving the CA powder in acetone. These solutions were subjected to magnetic stirring at room temperature (RT) for 5 minutes to ensure complete dissolution of the solute. Subsequently, the prepared solutions were utilized to produce films via spin coating and membranes via casting techniques.

For spin coating, glass slides cut with a diamond-tipped pen served as supports. The spinning speeds ranged from 1000 to 5000 rpm for 30 seconds, and drying temperatures ranged from 70°C to 120°C for intervals from 10 minutes to 2 hours. To produce thicker membranes, the casting technique was employed [85]. Solutions were prepared similarly and poured into borosilicate Petri dishes of 15 mm diameter. By using glass pipettes, drops of approximately 2 mL of volume were deposited. Two drying methods were tested:

- Single step drying at RT for varying times between 30 minutes and 8 hours.
- Two step drying process, comprising an initial air-drying step followed by thermal treatment on a hot plate. The heating temperatures ranged from 100°C to 250°C in 50°C increments, with films kept on the hot plate for 2 to 8 hours. A temperature limit of 250°C was set to prevent CA degradation, which begins around 330°C [86-87].

Ultimately, commercially available cellulose acetate (CA) membranes (GVS North America, Standford), 47 mm in diameter, thickness of 90-100 μm and pore size of 0.45 μm, typically used in biological applications for protein extraction, were employed. Bis[2-(methacryloyloxy)ethyl] phosphate (BMEP) (Sigma-Aldrich, USA) was used as a fire retardant. This monomer features a centrally located phosphate group flanked by two polymerizable methacrylate groups, capable of spontaneous conversion in acidic environments. BMEP is widely used as a reactive fire retardant incorporated during material production chemical reactions [88-89]. In this study, it was used to soak the CA membrane samples, leveraging its phosphate group and providing both sp^3 and sp^2 carbon atoms to the lased substrate. The membranes were immersed into BMEP for 20-30 seconds, until they were completely permeated. They were then dried using a N_2 blow gun.

3.1.2 Fabrication of laser induced graphene

The main fabrication technique used during the thesis has been direct laser writing, which consists in modifying the surface of a polymeric substrate through laser irradiation. The laser used for fabricating laser induced graphene was a hobby-grade infrared (IR) CO_2 laser with a wavelength of 10.6 μm and a maximum power of 40 W. The laser is guided by mirrors to a moving head that directs it onto the sample surface. This head is controlled by two stepper motors along the X and Y axes, and operated through a computer with an open-source interface, K40 Whisperer. The laser head moves while keeping the sample fixed in place. The laser-sample distance is fixed, as there is no motor for the Z direction, requiring focus adjustment beforehand. The system can move the laser head at a maximum speed of 600 mm s^{-1} in both directions and has two working modes: vector and raster. Vector mode moves the laser along a programmed path, ideal for outlines, while raster mode fills a solid design by irradiating the sample with parallel lines in the X direction. Raster mode includes options to

select the distance between the raster lines (to control the overlap) and the raster direction (top-to-bottom or bottom-to-top).

Initially, the focal plane distance was explored on Kapton®, a substrate with a well-documented conversion process into graphene. This investigation aimed to enhance the understanding of how varying fluence levels influence the morphology of the resulting graphene. Subsequently, the research shifted to cellulose acetate (CA). For both materials, preliminary dosing tests were conducted to identify the optimal parameter ranges that accomplished the transformation of the polymeric substrate into LIG while maintaining the integrity of the resulting material, without the formation of cracks and discontinuities. Based on these trials, specific conditions were selected for the characterization of the obtained material.

Samples were manufactured at various focal distances using aluminum bases of different thicknesses. The focal distance was determined to be 5.2 cm from the laser head through a plane-tilting test, using a methodology already described in the literature [67] and more extensively explained in the next section. In order to ensure some overlap between laser lines even at the focal plane, the inter-line distance was fixed to be 75 µm. Since the fume extraction of the laser system was positioned at the upper edge of the sample, all designs were engraved from the bottom and rastered upwards, as illustrated in *Figure 3.1*. This approach was adopted to prevent the deposition of dust on top of the finished material.

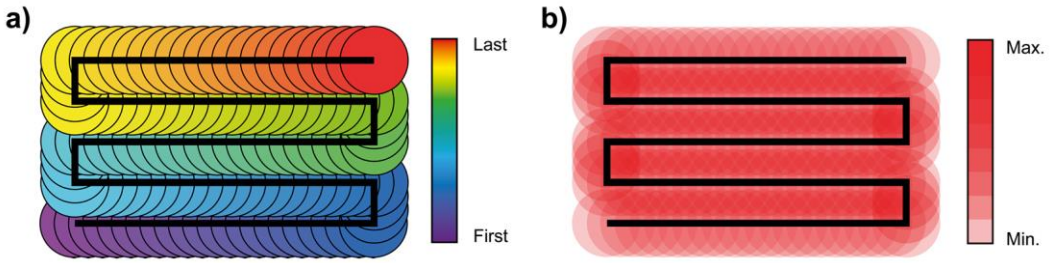

Figure 3.1: *Illustrations depicting the laser trajectory and accumulated laser exposure are as follows: (a) Illustration outlining the laser writing raster procedure. The black line denotes the laser's path, while the shaded region represents the area exposed to the laser radiation. (b) Scheme of the total laser intensity received by the sample through the laser raster process [72].*

3.1.3 Tilting angle test: assessment of focal distance

In this thesis work, one of the parameters explored to obtain laser induced graphene from the already well-known Kapton® was the distance between the sample plane and the focal plane of the laser beam. This was done to assess its effects on the resulting morphology and electrical properties. To accurately determine the focal distance and investigate its impact, lines were produced with constant speed and power during the synthesis process while varying the focal plane. This was achieved by placing the polymer substrate on a tilted surface, where the tilting angle controlled the different levels of fluence obtained.

A schematic of the experiment is shown in *Figure 3.2*, where the sample is laser-irradiated at an angle of 30°. The support was obtained by shaping an aluminum slab. As the laser beam moves horizontally in the x-direction at a speed v, the sample is tilted along the x' direction with an angle γ between x and x'. The spot size varies with the z position, leading to changes in the beam's maximum intensity and average fluence along the x' direction. Tilting the axis normal to the sample z' relative to the beam axis z by an angle γ modifies the distribution of beam intensity and modifies the geometry of the beam spot. Different lines were created by adjusting the laser power.

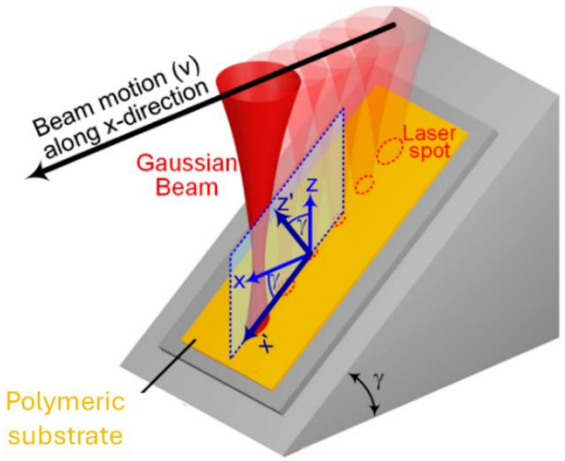

Figure 3.2: *Schematic of the setup employed to obtain a variation in the fluence by lasing a tilted polymeric substrate at an angle of 30°. Lines are fabricated along the x' axis while the laser beam moves in the x axis with speed v. Modified from* [67].

After the laser scribing process, samples were optically characterized to assess changes in the beam size. By accounting for the geometry of the aluminum support and the beam size, the fluence at various distances from the focal plane could be calculated using *Equation 1* from Section 2.2.3. Because the difference between fluence on a flat area and fluence on a

tilted area is negligible [67], the assessment of fluence at every point along the produced lines could be performed. The spot size, determined via optical microscopy in terms of diameter, is influenced by the thermal behavior of the polymeric substrate, making comparisons between different lasing power conditions unfeasible. However, comparisons within the same lasing power were possible. The spot size obtained from the microscope images can be correlated with the distance from the focal plane using simple trigonometric considerations, as shown in *Figure 3.3* and *Equation 2*:

$$y = x' \cdot \sin 30 = 0.5 \cdot x' \tag{2}$$

This allowed the determination of the focal distance, where the beam spot size was the smallest. Estimating the correct focal plane was crucial for subsequent parts of this thesis, guaranteeing that the reference focal plane had the smallest beam size under the selected experimental conditions.

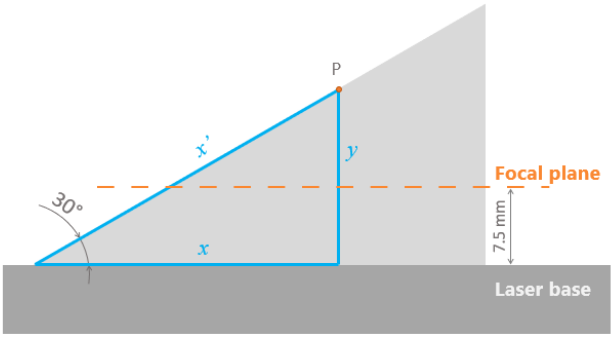

***Figure 3.3**: Trigonometric scheme illustrating the correlation between the spot size at point P and the distance from the base of the laser. The coordinate x' represents the measurable length directly on the sample. Coordinate x corresponds to the direction of laser scribing. Coordinate y indicates the maximum achievable distance from the focal plane (7.5 mm).*

$y = x' \cdot \sin 30 = 0.5 \cdot x'$For optical microscopy observation, the samples were fixed onto a glass slide with adhesive Kapton®. Image processing to determine the laser beam diameter was performed using ImageJ software [90]. The results are detailed in Section 4.1.

3.1.4 Optimization of lasing process

As stated in Section 2.2.3, there is a multitude of laser parameters that can be adjusted during the lasing process. Considering the limitations of the laser equipment and relying on the results in existing literature, the parameters varied across different samples were laser power, scan speed and focal distance.

3.1.5 Cellulose acetate supercapacitor proof of concept

In the final part of this thesis, an electric double-layer (EDL) supercapacitor was developed as proof-of-concept to demonstrate a real-world application of the optimized material. The chosen electrode design is based on a planar interdigitated geometry, illustrated in *Figure 3.4*. This geometry, as previously highlighted, provides a larger surface area exposed to the electrolyte and allows for faster access between oppositely charged electrodes.

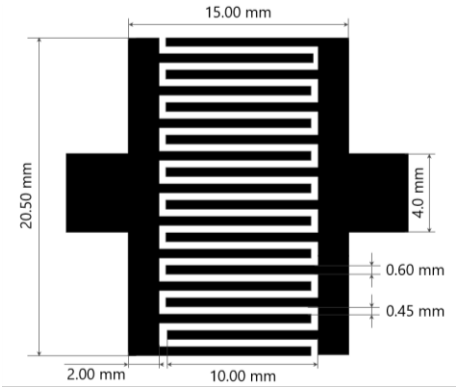

Figure 3.4: *Design used to fabricate the device.*

The supercapacitor prototype was fabricated by producing two symmetric electrodes of LIG derived from cellulose acetate (CA). The CA membrane was immersed in the flame retardant (BMP) and dried with a nitrogen gun. Subsequently, the membrane was placed on a laboratory glass slide, ensuring no bubbles formed between the surfaces. The CA was then introduced into the laser chamber and aligned with the computer control program, where the design was uploaded. The lasing process was conducted under conditions determined to produce the optimal material.

The fabrication of the first device at the ISOM laboratories began with the successful transfer of the design onto the substrate. The subsequent step involved establishing electrical contacts for each electrode to enable connection with the characterization equipment. Conductive silver paste was applied to the contact pads of each electrode, followed by the placement of conductive copper adhesive tape. To protect the active area, LOCTITE EA 3423 (Henkel, Germany), a two-component epoxy adhesive, was used to create a protective layer around the transferred design, effectively sealing the contacts and preventing the copper from exposure to the electrolyte, thereby avoiding corrosion. Finally, several drops of liquid electrolyte were introduced onto the Laser-Induced Graphene (LIG) electrodes. H_2SO_4 1M

was selected as the electrolyte due to its ease of processing. However, the applicable voltage window was limited by hydrolysis reactions occurring above 1.1 V.

At Politecnico di Torino, the device assembly process was optimized. Before conducting two-electrode tests on the device, a three-electrode configuration test was performed using a platinum electrode as the counter electrode and a Ag/AgCl electrode saturated with a 3 M KCl solution as the reference electrode. This configuration enabled a detailed study of the electrochemical properties of the electrode through Electrochemical Impedance Spectroscopy (EIS) and cyclic voltammetry (CV). The CV analysis was particularly useful for identifying the optimal potential window for the subsequent operation of the device. After determining the working potential window, two-electrode tests were conducted on devices prepared with various electrolytes. To reduce the contact resistance between the electrodes and the current collector, a titanium mesh was placed to cover the entire inactive area of the electrodes and secured using adhesive tape. A piece of glass fiber was then cut and positioned over the active area of the device. The assembly was completed by adding another glass slide, which was fixed in place with adhesive tape, ensuring adequate pressure and enhancing the contact between the electrodes and the current collector. The electrolyte was introduced using micropipettes, and continuous wetting of the glass fiber was maintained by immersing part of it into a container filled with the electrolyte.

The initial tests at ISOM were conducted using 1 M sulfuric acid (H_2SO_4) as the electrolyte, with the device tested in a two-electrode configuration. At the DISAT laboratories, further testing of the devices was carried out in a two-electrode configuration using different electrolytes, specifically 0.5 M H_2SO_4, 0.5 M Na_2SO_4 and 1 M KOH, to evaluate the device performances in different aqueous environments.

3.2 Characterizations

Investigating the resulting physicochemical properties of laser induced graphene structures obtained using different synthesis parameters is of extreme importance. It enables the adjustment of the lasing conditions to tune the final properties of the material that are desired for specific applications. In this section, a detailed explanation of the utilized characterization techniques is presented.

3.2.1 Optical microscopy

Optical microscopy was employed for rapid inspection of samples during processing steps. The operating principle is straightforward: visible light is used to magnify the object of interest through a series of optical lenses. The maximum lateral resolution, which represents the smallest distance between two distinguishable points, is determined by the wave nature of light, with an upper limit of 200 nm using visible light. However, as magnification and resolution increase, the depth of focus (DOF) diminishes. The DOF, which indicates the axial range over which features remain sharp, is inversely related to the wavelength of the light source, resulting in a reduced DOF with higher resolution.

Within the characterization facilities of ISOM, a Bresser Researcher ICD 20-80x optical microscope (Bresser, Germany) was utilized for quick inspection of laser induced graphene samples, while a Leica Leitz DMRX (Leica, Germany) was employed to obtain images at higher magnifications.

3.2.2 Scanning electron microscopy

The surface morphology of the obtained LIG can be tuned by changing the lasing parameters. It is well known that the porous structure forms because of the gaseous product escaping from the substrate during the laser ablation [10, 26, 37]. Morphology transitions have been identified when changing the lasing parameters, eventually leading to closed pores because of the melting of the material and the collapse of the structure [67]. Scanning electron microscopy (SEM) is generally employed to evaluate the porous and corrugated surface of the obtained LIG structure; further using of transmission electron microscopy (TEM) may allow to image nano and sub-nano features of the resulting material, with particular focus on LIG sheets and layers features [5, 36].

Scanning electron microscopy offers higher spatial resolution, greater depth of field, and more specific topography information compared to optical microscopy, and it can provide qualitative chemical composition information. SEM uses an electron beam, generated by an electron gun, which is focused and directed by electromagnetic lenses to the sample surface. The specimen is placed on a movable stage within a high-vacuum system to prevent electron scattering. Secondary electrons (SE) are emitted due to inelastic collisions of primary electrons with atoms in the sample's outermost layers, providing topographical information.

SEs are collected preferentially by a positively biased detector, creating three-dimensional-like images that highlight edges and protrusions. For better contrast in chemical composition, backscattered electrons (BSE) are used. BSEs, generated by elastic interactions with deeper atoms, provide elemental contrast as heavier elements backscatter more electrons, appearing brighter in BSE images. Additional signals arise from electron-sample interactions. X-rays, emitted when electrons transition to lower energy states, allow for qualitative elemental analysis using specialized detectors. Auger electrons, released during similar transitions, provide further compositional information. Cathodoluminescence involves high-energy electrons exciting the sample's electrons, which then emit photons as they return to their original state, offering insights into the material's composition and electronic structure.

At ISOM, researchers have access to a FEI Inspect F50 SEM (FEI, United States), which offers a maximum acceleration potential of 30 kV and can achieve magnifications of up to 1 000 000x. Moreover, it has a MonoCL4 add-on (Gatan, United States) for performing cathodoluminescence measurements. During this work, the usual voltage used for Kapton®-lased samples was 5 kV. CA-lased samples' pictures were taken at IMN (Instituto de Micro y Nanotecnologia, Consejo Superior de Investigaciones Científicas) using a FEI Verios 460 (FEI, United States) with a voltage of 2 kV. All the images were obtained using SE.

Prior to introducing the samples into the SEM for imaging, it was essential to establish conductive pathways using copper adhesive tape and silver paste.

3.2.3 Raman spectroscopy

Raman spectroscopy is a powerful technique for identifying chemical species by analyzing light-matter interactions. When near-infrared (NIR) or visible light interacts with a molecule, it excites the molecule from a vibrational state to a virtual state. Depending on how the molecule relaxes, different types of scattering occur [91]:

- Rayleigh scattering (elastic, no energy change)
- Stokes scattering (inelastic, lower energy photon emitted)
- Anti-Stokes scattering (inelastic, higher energy photon emitted)

Rayleigh scattering is the most common, while Anti-Stokes scattering is the least common due to the need for pre-existing vibrational excitation. Raman measurements typically focus on Stokes scattering because of the weak Anti-Stokes signal and filtering processes. The

energy change between incident and scattered photons is expressed in wavenumbers. NIR and visible light are commonly used, with ultraviolet light being less common due to potential sample photodecomposition.

Due to its ability to identify the structural fingerprint of a sample, Raman spectroscopy is a crucial characterization technique for determining the chemical nature and quality of synthesized laser induced graphene and the carbon allotropes formed during the lasing process. By analyzing peak intensities, shapes, positions, and ratios, Raman spectroscopy assesses the quality of the synthesized material and distinguishes between multi-layer, few-layer, and single-layer graphene [10-11], as well as the presence of amorphous carbon, graphene oxide (GO) and reduced graphene oxide (rGO), or other carbonaceous structures [92-93]. In particular, laser induced graphene structures exhibit three well-distinguished peaks (*Figure 3.5*):

- D band (~1300-1500 cm^{-1}): corresponds to disordered regions caused by defective sp^2 carbon bonds or structural defects in the graphene layers.
- G band (~1500-1600 cm^{-1}): associated with the ordered graphite region.
- 2D band (~2650-2700 cm^{-1}): indicates the quality of graphene and the number of graphene layers present.

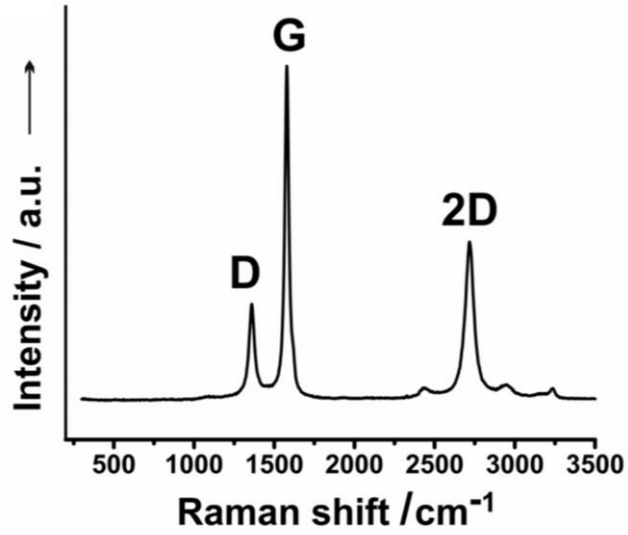

Figure 3.5: *Typical Raman spectrum of a LIG structure obtained from Kapton®. A sharp 2D peak is characteristic of the graphemic structure and indicates the number of graphene layers in the sample. The G band is associated with the ordered graphite region while the D band corresponds to the defective, disordered region [40].*

To compare and assess the quality of different LIG structures, there are two key quantities:

- I_D/I_G ratio: represents the ratio of defective to crystalline structures in the obtained graphene-like material.
- I_{2D}/I_G ratio: corresponds to the number of graphene layers stacked together.

Additionally, other structures obtained from laser scribing of polymeric substrates, such as amorphous carbon, graphene oxide (GO), and reduced graphene oxide (rGO), can be characterized by their specific Raman spectra. The characteristic Raman spectra of carbon solids and nanostructures are illustrated in *Figure 3.6 (a)*, while the Raman spectra of graphene-based materials are shown in *Figure 3.6 (b)*.

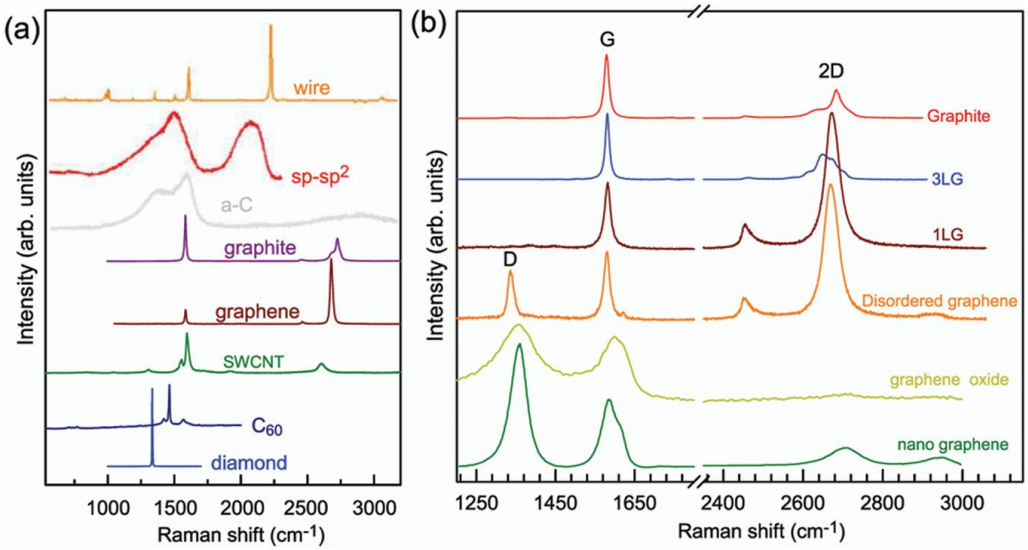

Figure 3.6: *(a) Raman spectra of carbon solids and nanostructures, encompassing various forms such as 1D carbon wires, sp-sp² carbon, amorphous carbon (a-C), graphite, graphene, single-walled carbon nanotubes (SWNT), C_{60}, and diamond. (b) Raman spectra of graphene-based materials, comprising graphite, monolayer graphene (1LG), trilayer graphene (3LG), disordered graphene, graphene oxide, and nanographene. Spectra in (a) and (b) are from [94].*

Raman spectroscopy was performed by using a Horiba LabRAM HR Evolution using a 532 nm laser. Sample inspection occurred through a microscope objective (10x) after calibration of the instrument with a well-known Si sample.

3.2.4 Resistivity measurements: Van der Pauw

Electrical measurements are fundamental for evaluating LIG structures, as these materials are considered promising candidates for energy harvesting, flexible electronics, and

electrochemical sensing due to their conductivity and high porosity, which provides large surface areas [10]. Electrical conductivity is typically evaluated in bulk materials without dimensional constraints. However, due to the limited thickness of LIG films (ranging from a few micrometers to hundreds of micrometers depending on the laser wavelength and irradiation parameters used), sheet resistance becomes a more appropriate measurement for these structures [48]. To measure the intrinsic conductivity of LIG structures, the four-probe method, specifically the Van der Pauw one, is widely utilized.

The four-probe technique, also known as the Kelvin measurement, is one of the most common methods for measuring the electrical resistivity of thin films. Unlike the traditional two-probe setup, the four-probe technique minimizes the impact of contact resistances and parasitic cabling, providing a more accurate assessment of the sample's resistivity. However, resistivity measurements are inherently geometry-dependent and highly sensitive to boundary conditions, requiring the calculation of various correction factors. Consequently, for thin films, resistivity is often expressed in terms of sheet resistivity (R_S), defined as *Equation 3* [95]:

$$R_s = \frac{\pi}{\ln 2}\frac{\Delta V}{I} \tag{3}$$

where I is the injected current and ΔV the measured voltage drop. The Van der Pauw method is highly effective and widely employed within the four-probe mode for determining the sheet resistivities of homogeneous materials, particularly thin films with arbitrary shapes. Successful application of this method relies on several factors, including uniform sample thickness, absence of isolated voids, and precise contacts along its perimeter [96-97]. Commonly used sample shapes include squares, circles, and cloverleaf configurations, with squares and cloverleaf designs often preferred for their practicality and ability to minimize errors at contact points [96, 98]. Additionally, the Greek cross structure is utilized to evaluate the sheet resistivity of discrete semiconductor and metallic materials, allowing for the reduction of errors associated with non-ideal and finite contacts [95].

To measure the sheet resistivity of LIG samples, a modified Greek cross structure has been utilized for LIG derived from Kapton®, as shown in *Figure 3.7 (a)*. This design includes protruding corners forming a square shape, each measuring 1.40 mm, to reduce measurement errors due to sample non-ideality. The connecting arms are 1.00 mm long. For LIG samples

from CA, a square shape was used instead, as illustrated in *Figure 3.7 (b)*. This choice ensures a more uniform heat distribution during the lasing process on this delicate substrate, minimizing defects like hot spots or holes.

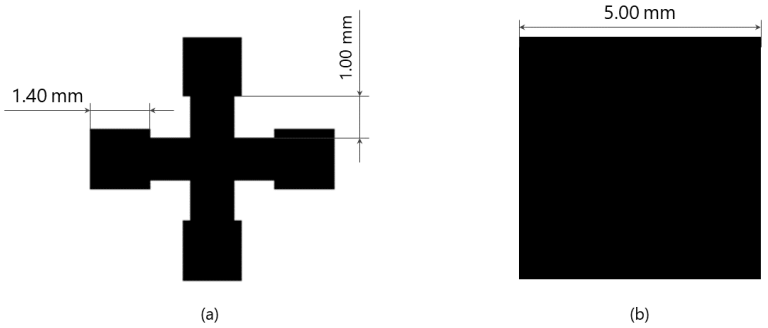

Figure 3.7: *(a) Greek cross shape used for LIG samples from Kapton®, (b) square shape used for LIG samples from CA in sheet resistance measurements through Van der Pauw method.*

The sheet resistance is determined by performing resistance measurements. A direct current (DC) ranging from 0 to 1 mA is applied between two contacts, and the voltage drop across the opposing edges is measured. Using the configurations shown in *Figure 3.8 (a)* and *Figure 3.8 (b)* and applying Ohm's law, the resistance value is calculated, as calculated in *Equation 4*:

$$R_{AB,CD} = \frac{V_{CD}}{I_{AB}} \tag{4}$$

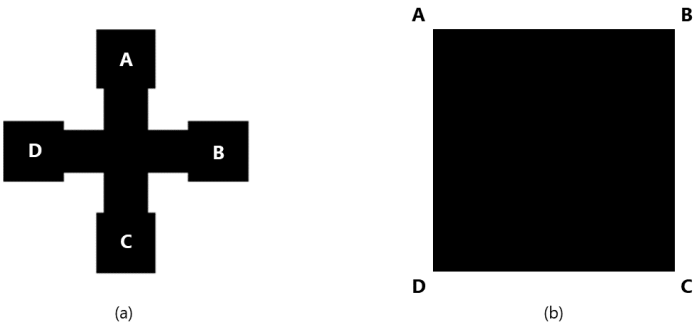

Figure 3.8: *Scheme diagram showing an example of configuration for the measuring of electrical resistivity by Van der Pauw method in (a) LIG samples from Kapton® and (b) LIG samples from CA.*

Due to the reciprocity theorem, it can be asserted that the resistance measured by interchanging the current and voltage contacts theoretically equals ($R_{AB,CD} = R_{CD,AB}$). This suggests that the sheet resistivity can be readily determined by substituting the obtained

resistance into *Equation 3*. To obtain more accurate resistance values, $R_{vertical}$ and $R_{horizontal}$ are defined as outlined in *Equation 5* and *Equation 6* respectively.

$$R_{vertical} = \frac{R_{AB,CD} + R_{CD,AB}}{2} \quad (5)$$

$$R_{horizontal} = \frac{R_{BC,DA} + R_{DA,BC}}{2} \quad (6)$$

The average of these measurements is subsequently employed to calculate the sheet resistivity of the structures using *Equation 3*.

During this project at ISOM, a Karl Suss PSN 6 probe station, equipped with four manual micromanipulators, was used. This probe station is typically linked to a semiconductor parameter analyzer rack comprising two Agilent units, specifically the Agilent 4156C and Agilent 4150B, controlled via the EasyExpert software (Agilent). For this thesis, all the four terminals were employed, being two of them utilized for current application, swiped in the range from 0 to 1 mA with a step of 10 μA, and the other two, for voltage measurement. With the assistance of the EasyExpert software, it was possible to interchange the terminals for current injection and voltage measurement after positioning the probes using the optical microscope.

To minimize resistance at the probe contact and reduce associated errors, silver paste was applied to cover the four corners, as shown in subsequent sections.

3.2.5 Sessile drop method

The static contact angle is geometrically defined as the angle created by the liquid at the three-phase boundary, where gas, liquid and solid, or in some circumstances two liquid and the solid, intersect. The interacting forces that act at the interfaces and reach the equilibrium balancing each other are intermolecular forces, namely cohesive and adhesive forces (*Figure 3.9*). The first ones act on similar molecules, for example hydrogen bonds and Van der Waals forces; the second ones are exerted on molecules that are dissimilar, such as mechanical and electrostatic forces.

The contact angle is measured in the liquid at the liquid-solid interface when a drop is deposited onto the solid surface. In the case of LIG, the exposure of substrates of different

nature to laser action, combined with the variation of process parameters, results in achieving different wettability of the final material, namely obtaining contact angles ranging between 0 and 180°. Both superhydrophobic and superhydrophilic behaviors are interesting to achieve in LIG structures. The first is preferred in the case of graphene-like material used in water/oil separation applications; the latter, instead, is wanted in the case of electrochemical applications due to an enhanced contact with the electrolyte [48].

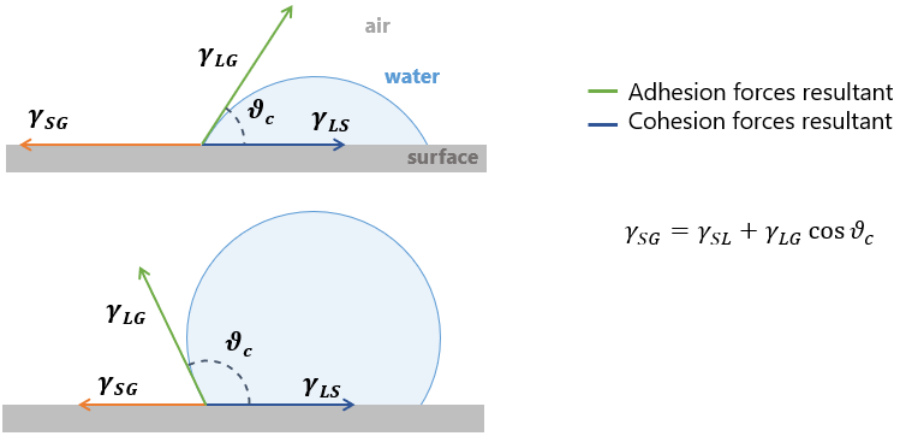

Figure 3.9: *Schematic representation of adhesive and cohesive forces, illustrating their role in determining the contact angle within a liquid drop. When the contact angle (θ_C) is less than 90°, the surface is hydrophilic; conversely, if θ_C is greater than 90°, the surface is hydrophobic. The contact angle is calculated using Young's equation, depicted in the figure. γ_{SG} is the surface energy at the solid-gas interface; γ_{LS} represents the surface energy between the liquid and the solid; γ_{LG} denotes the surface energy at the liquid-gas interface.*

In this thesis, static contact angle measurements were conducted using water as the testing liquid. A video capturing the moment when the drop was deposited onto the sample surface was recorded. Utilizing imaging software, specifically ImageJ [90], the photogram of the precise instant of contact between the water drop and the surface was analyzed and the contact angle (θ_C) was accurately determined.

3.2.6 Electrochemical characterization

To assess the electrochemical properties of the assembled devices, an Autolab PGSTAT204 potentiostat/galvanostat system (Metrohm, Switzerland) was initially employed at the ISOM laboratories to conduct cyclic voltammetry (CV) and galvanostatic charge-discharge (GCD) tests. Subsequently, at the DISAT laboratories of Politecnico di Torino, a multichannel

potentiostat (BioLogic, USA) was used to perform electrochemical impedance spectroscopy (EIS), as well as additional CV and GCD testing.

Electrochemical Impedance Spectroscopy (EIS) is used to evaluate the impedance response of a device across a range of AC voltage frequencies. In this technique, a small AC potential is applied to the device, generating an AC current signal that exhibits a phase shift. The most common representation of EIS data is the Nyquist plot, as illustrated in *Figure 3.10*. In the Nyquist plot representation, the real and negative imaginary components of the complex signal are plotted in a 1:1 scale. The real component of the impedance (Z') is plotted on the x-axis and corresponds to a resistance value, while the negative imaginary component (Z'') is displayed on the y-axis and corresponds to the capacitive and inductive response of the system.

The total resistance in a supercapacitor originates from several sources, including the resistance of the electrolyte, the resistance of the electrode material, the contact resistance between the active material and the current collector, and the resistance of the electrolyte within the porous structure of the active material. Specifically, the intrinsic resistance of the electrolyte ($R_{electrolyte}$) and the diffusion resistance of the electrolyte within the porous structure of activated carbon (R_{diff}) are largely influenced by the properties of both the electrolyte and the electrode materials. In contrast, boundary resistances at interfaces such as electrode-current collector interfaces can be optimized during the electrode fabrication process. All of these factors happen at different time scales, contribute to the overall impedance and can be modeled using an equivalent circuit that fits the measured EIS spectrum. Of particular importance is the intersection of the curve with the x-axis at higher frequencies, which represents the equivalent series resistance (ESR). The ESR is a cumulative measure that includes the active material interface resistance, the electrolyte ionic resistance, the electrode/electrolyte interface resistance, and the electrode-current collector interface resistance [99].

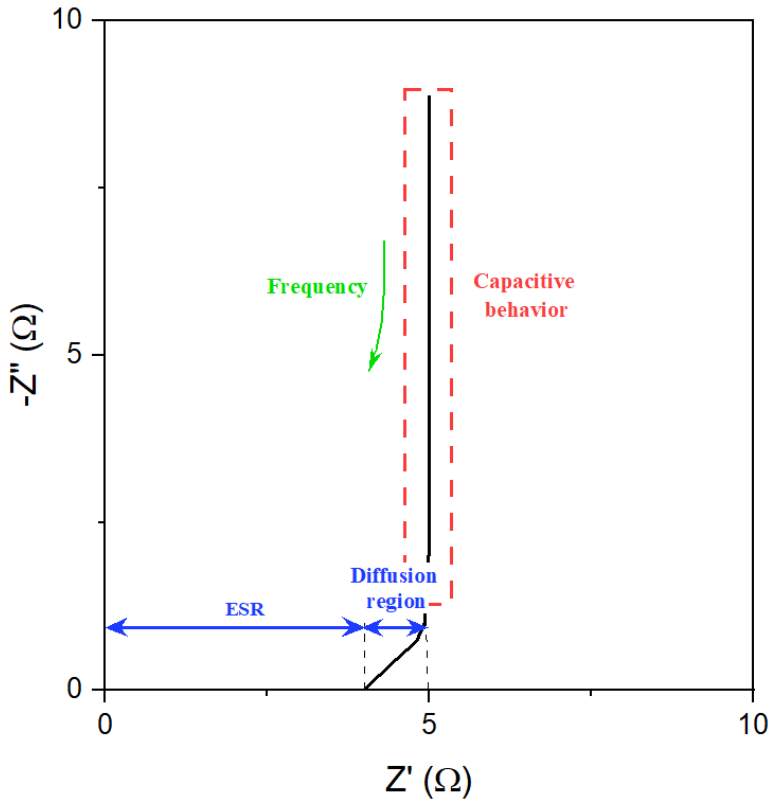

Figure 3.10: *Typical Nyquist plot for an EDLC based on porous carbonaceous material. The intercept with the x-axis at high frequencies corresponds to the equivalent series resistance (ESR), encompassing the resistance contributions from the material interfaces, ionic resistance of the electrolyte, the electrode/electrolyte interface, and the electrode-current collector interface. Moving from high to medium frequencies, the plot exhibits a characteristic diffusion region, representing the electrolyte resistance through the electrode pores. Both resistive contributions are highlighted in blue. The diffusion region is followed by a near-vertical line at lower frequencies, indicative of the device's capacitive behavior, and is represented in red. Adaptation from [99]*

In a typical CV, the current response of the device is measured when a potential is applied. A CV curve, which involves monitoring the current response during two linear potential sweeps in a cyclic manner, is defined as a cyclic voltammogram. Initially, the potential is varied at a defined scan rate (V s^{-1}) from an initial voltage V_1 to a final voltage V_2 during the first linear potential sweep; subsequently, in the second sweep, the potential is reversed from V_2 back to V_1. Ideally, in EDLCs the CV exhibits a rectangular or quasi-rectangular shape. From the shape of the obtained CV, the storage mechanism (electric double-layer capacitance, pseudocapacitance, or hybrid) can be inferred, as shown in *Figure 3.11* [7].

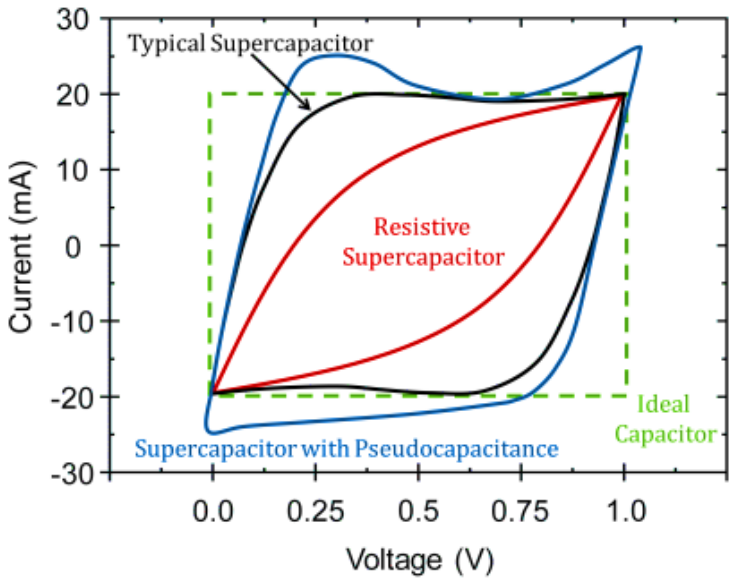

Figure 3.11: *Comparison of CV responses showing distinct characteristics for different supercapacitor types: ideal EDLC, displaying constant current at constant voltage sweep with a perfect rectangular shape (green curve); real EDLCs, affected by internal resistance and exhibiting a modified rectangular shape (black curve); resistive capacitors, with increased internal resistance, showing a greater deviation from the ideal square at the charge-discharge corners (red curve); hybrid supercapacitors, which incorporate pseudocapacitance, featuring curvier and wavier shape (blue curve) [100].*

In the galvanostatic charge-discharge technique, a constant current is applied to the electrode material, and voltage changes are measured over a defined potential range as a function of time. When a constant positive current is applied to the working electrode, the potential increases from an initial voltage V_1 to a final voltage V_2 over time. Subsequently, an equal magnitude constant negative current is applied, resulting in a potential step-down. This measurement simulates the actual operation of the device. Similar to voltammograms, the shape of the GCD profile varies based on the storage mechanism and its kinetics. For an ideal electric double-layer supercapacitor, the GCD profile is a symmetrical triangle for a complete charge-discharge cycle [7]. In real devices, however, there is a characteristic voltage drop when switching from positive (charging) to negative (discharging) currents, causing asymmetry in the GCD curves, as shown in *Figure 3.12*. This asymmetry is due to the resistive elements in the device, including the electrode, the electrolyte, the current collectors and the interface between these components.

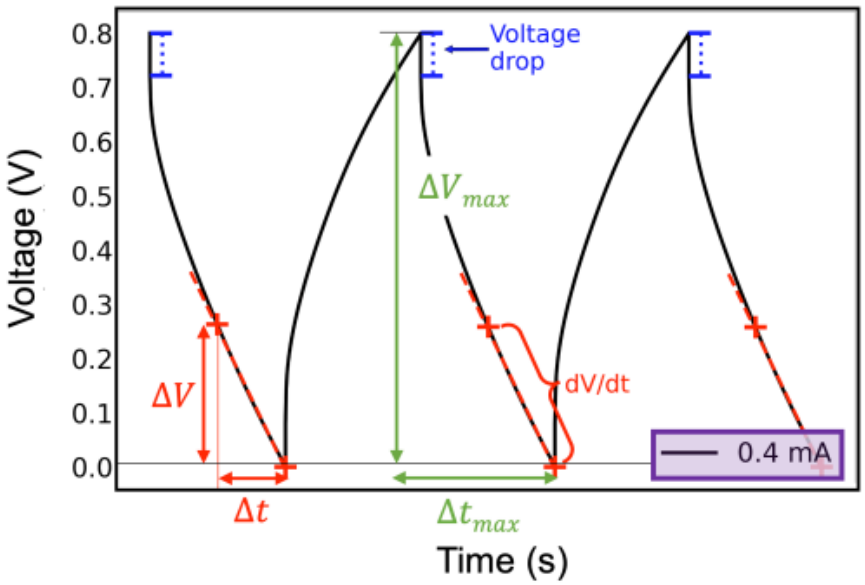

Figure 3.12: *Examples of galvanostatic charge-discharge plots. The highlighted parameters are those extracted for subsequent calculations. Specifically: the potential drop, also referred to as the 'IR drop,' is shown in blue; the slope of the discharge curve, defined by the value dV/dt, is marked in red. This value is calculated over the discharge interval Δt in which a discharge potential ΔV is observed; the total discharge potential and the total discharge time are indicated in green [72].*

From these characterization techniques, relevant performance metrics for the tested devices can be extracted, as outlined in the following equations. More specifically, they were suited for analyzing GCD measurements. In fact, this technique is the most reliable for evaluating the areal capacitance (C_{area}, mF cm^{-2}) of the material, representing the amount of charge stored per unit area over a specific potential window, as shown in *Equation 7*.

$$C_{area} = \frac{I_{discharge}}{S \times \left(\frac{dV}{dt}\right)} \tag{7}$$

Where $I_{discharge}$ is the constant discharge current, S is the total area of both positive negative and positive electrodes, and dV/dt is the slope of the discharge curves, shown in red in *Figure 3.12*. Additionally, the energy density (μWh cm^{-2}) of the device can be determined using *Equation 8*.

$$E_{area} = \frac{1}{2} \times C_{area} \times \frac{(\Delta V)^2}{3600} \tag{8}$$

Where $\Delta V = V_{max} - V_{drop}$ is the discharge voltage, as depicted in red in *Figure 3.12*. $V_{max} = 1\,V$ for aqueous electrolytes; V_{drop} is the voltage difference between V_{max} and the next point in the discharge curve. Finally, the areal power density is evaluated following *Equation 9*:

$$P_{area} = \frac{E_{area}}{\Delta t} \times 3600 \tag{9}$$

Being Δt the discharge time in seconds [101].

At Politecnico di Torino, the potentiostat is equipped with EC-Lab software, providing a useful tool for analyzing data. In particular in this work, GCD allowed for the extraction of discharge energy and discharge charge for each cycle. The capacity C of the device could be correlated to these quantities through *Equation 10*:

$$C_a = \frac{1}{S} \cdot \frac{Q_d^2}{2E_d} \tag{10}$$

Where Q_d is the discharge charge and E_d is the discharge energy [J].

Furthermore, by extracting the discharge time Δt, it is possible to calculate the power density using the following *Equation 11*:

$$P_{area} = \frac{E_{area}}{\Delta t} \text{ x } 3600 \tag{11}$$

Where E_{area} is the discharge energy divided by the active area surface [mm^2].

4. Results and discussion

This thesis experimental methodology was divided into three distinct phases:

- **Determination of the laser focal plane and investigation of defocus effects on Kapton® pyrolysis**. This initial investigation was performed to gain deeper insight into the effects of varying fluence levels on the resulting graphene morphology. The focal plane was established using a tilted angle test, a crucial step for subsequent analyses of changes in morphology, quality, and material properties resulting from the laser writing process. Kapton® was then lased at different distances from the focal plane, and the resulting graphenic materials were characterized using scanning electron microscopy (SEM), Raman spectroscopy, and sheet resistivity measurements via the Van der Pauw method.
- **Exploration of a sustainable and innovative precursor**. Cellulose acetate was the chosen organic material to transform into laser induced graphene. Initially, films and membranes were fabricated in the laboratory. Subsequently, commercial membranes, commonly used in biological applications, were utilized. The laser process was optimized using the knowledge gained from varying the lasing conditions on Kapton®. The processed materials were characterized using Raman spectroscopy, SEM, the Van der Pauw method, and the static sessile drop method.
- **Development of a supercapacitor proof-of-concept**. The optimal conditions identified for producing the best graphenic material from cellulose acetate were employed to fabricate a proof-of-concept supercapacitor. The device performance was evaluated through cyclic voltammetry and galvanostatic charge-discharge tests.
- **Optimization of Device Assembly and Electrolyte Selection.** The device design was retained, but the contact method was improved to minimize resistive contributions. electrochemical characterization through electrochemical impedance spectroscopy, cyclic voltammetry, and galvanostatic charge-discharge were conducted to evaluate device performance across different aqueous electrolytes.

4.1 Laser induced graphene from Kapton®

4.1.1 Tilted angle test

The tilted angle test was conducted on Kapton® due to its well-documented behavior when irradiated by laser and the extensive experience of the research group with this material. *Figure 4.1* (left) shows the samples obtained from the tilted angle test, which were subsequently analyzed using an optical microscope. The green square in the same figure (right) highlights the optical microscope images, taken at 100x magnification, of the section with the smallest diameter in the three samples.

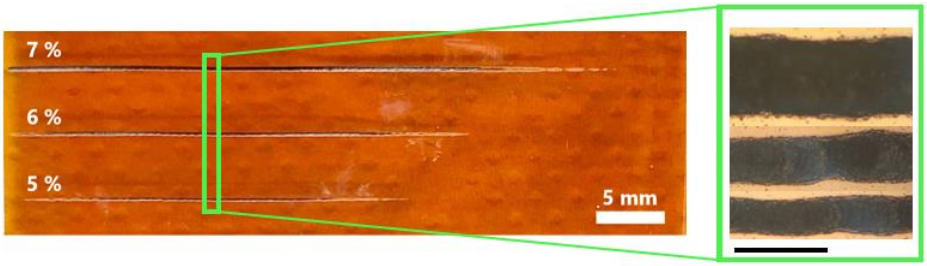

Figure 4.1: *Picture of the samples obtained from the tilted angle test (left). All the three lines were scribed at a scan speed of 70 mm s^{-1}, while the power was varied as indicated: 5%, 6%, and 7%. In the inset square on the right, the optical microscope images are provided. The used magnification was 100x. The black scalebar for the optical images corresponds to 500 µm.*

The beam diameter was evaluated at various points, ensuring that the focal distances used later in the experimental part were considered. The x' coordinates used to identify these points in the optical microscope images were converted to y coordinates using *Equation 3* (Section 3.1.3). The resulting data are displayed as curves in *Figure 4.2*.

Each curve exhibits a minimum, corresponding to the distance from the base of the aluminum support where the focal distance is located. By identifying the position of these minima across three series and averaging the results, the focal plane was determined to be at a distance of 7.50 ± 0.05 mm from the base of the laser setup. It was also observed that the measured laser beam spot size at the focal plane differed from the set-up size of 125 µm, increasing with higher lasing power. This discrepancy is likely due to thermal effects arising from the interaction between the laser and the polymeric substrate, which intensify with increased power as more energy is delivered onto the substrate's surface. Fluence was

evaluated for each series using *Equation 1* (Section 2.2.3) and the beam diameters obtained from the optical images.

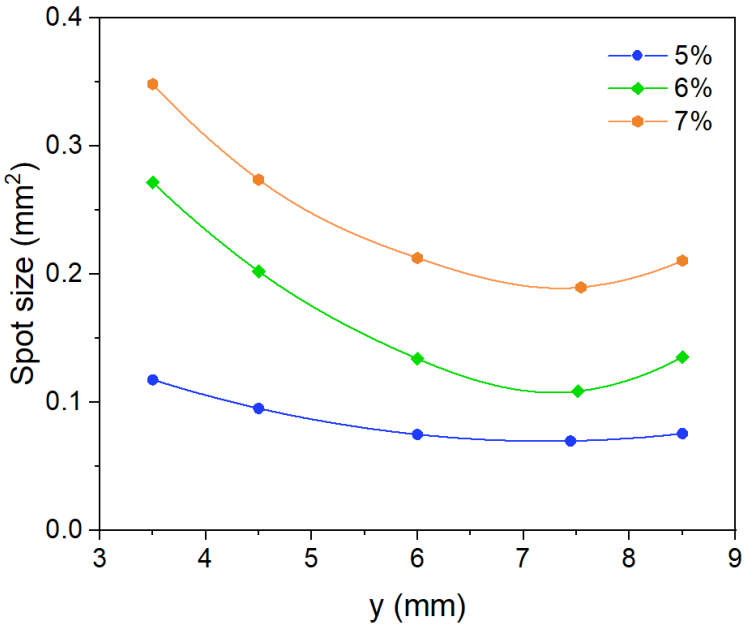

Figure 4.2: *Change of beam spot size (mm^2) when varying the lasing plane keeping constant the other lasing parameters (power and speed). y coordinate refers to the distance of the selected point from the base of the tilted base used.*

As mentioned earlier, comparisons between different lasing powers were not feasible due to the thermal effects induced in the polymeric substrate and the Gaussian profile of the laser beam, which are not accounted for in the equation. Instead, the trend in fluence within the same series was analyzed, as the lasing power and scanning speed remained constant, making the application of *Equation 1* qualitative. An example of this trend is shown in *Figure 4.3*. As expected, fluence decreases with increasing distance from the focal plane, as the energy spreads over a larger area, resulting in lower optical energy delivered per unit surface area. The influence of this phenomenon on the properties of the resulting material was first studied on Kapton® and then applied to cellulose acetate. This approach allows the delivery of the same amount of energy in a more controlled manner, making it suitable for more delicate materials.

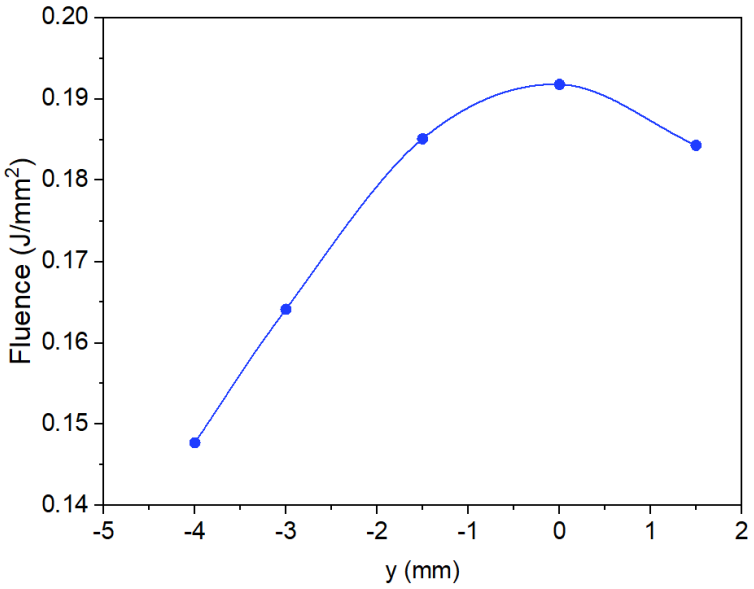

Figure 4.3: *Qualitative trend of optical energy delivered per unit of surface area in the sample produced at lasing power of 5%, and scan speed of 70 mm s^{-1}. y coordinate refers to the distance from the previously evaluated focal plane.*

4.1.2 Lasing process on Kapton® films

In the initial phase of this thesis, the aim was to examine how the distance of the polymeric substrate from the focal plane influences the final properties of the resultant LIG. The polymer under investigation was the widely used Kapton®, which is polyimide (PI). The 125 µm thick PI film was cleaned with isopropanol and affixed to the aluminum slab using a 60 µm thick Kapton® tape with a silicon adhesive to prevent any movement during the lasing process. Ensuring a flat surface was crucial to avoid variations in fluence across the sample due to wrinkles or substrate folding. The PI was thus introduced in the laser chamber and then subjected to lasing with constant speed and power settings (6%, 60 mm s^{-1} for the first series; 7%, 70 mm s^{-1} for the second series) while varying the lasing plane using aluminum plates of different thicknesses (6.5 mm, 6 mm, 4.5 mm, 3.5 mm). The name of the samples and the lasing conditions used for each of them in this preliminary test are detailed in *Table 4.1*.

Table 4.1: *Summary of the laser conditions for samples fabricated in the first phase of experimentation. The sample names indicate the series they belong to (Series 1: 6% of power, 60 mm s^{-1} of scanning speed; Series 2: 7% of power, 70 mm s^{-1} of scanning speed) and the thickness of the aluminum base used. Additional information on the distance from the focal plane is also provided. Samples marked with (*) are the ones that were fully characterized with Raman spectroscopy, SEM imaging and Vand der Pauw conductivity measurements.*

6 %, 60 mm s^{-1}	**7%, 70 mm s^{-1}**	**Base thickness (mm)**
S1-7.5	S2-7.5 (*)	7.5 *focal plane*
S1-6.5	S2-6.5	6.5 *-1.0 mm defocus*
S1-6.0	S2-6.0 (*)	6 *-1.5 mm defocus*
S1-4.5	S2-4.5 (*)	4.5 *-3.0 mm defocus*
S1-3.5	S2-3.5	3.5 *-4.0 mm defocus*

After visually inspecting the samples, it was observed that the most significant macroscopic change occurred farther from the focal plane, particularly greyish areas were noticed. It was then decided to further investigate the influence of power and scanning speed on the plane set 3 mm away from the focal plane. Specifically, the power settings were varied between 4.5% and 7% in 0.5% increments. For power levels between 4.5% and 5.5%, the raster speed was varied from 10 to 90 mm s^{-1} in 10 mm s^{-1} increments, while for power levels between 6% and 7%, the raster speed ranged from 40 to 120 mm s^{-1} in 10 mm s^{-1} increments. This decision was based on the observation that at lower power settings, excessively high speeds resulted in incomplete material transformation due to insufficient thermal energy supplied to the substrate. Conversely, at higher power settings, excessively low speeds led to the complete ablation of the material. All experimental conditions implemented in this second phase are detailed in *Appendix A1.*

The SEM and Raman samples were prepared as 4 mm × 4 mm squares. For the SEM samples, conductive tracks were created using copper adhesive tape to discharge accumulated charges from the electron beam through the metallic support. Additionally, silver paste was applied to enhance conductivity at the tape-LIG contact point. An illustrative image is shown in *Figure 4.4 (a)*. For the Raman spectroscopy samples, the Kapton® film

was affixed to a glass slide using adhesive PI tape. Copper adhesive tape was then placed on each sample to dissipate the thermal stress induced by the laser through the metallic contact during analysis. *Figure 4.4 (b)* shows an example of a sample analyzed using Raman spectroscopy. Regarding the conductivity measurements, cross-shaped samples were prepared. To minimize contact resistance between the probe and the sample, silver paste was applied to the four corners, as depicted in *Figure 4.4 (c)*.

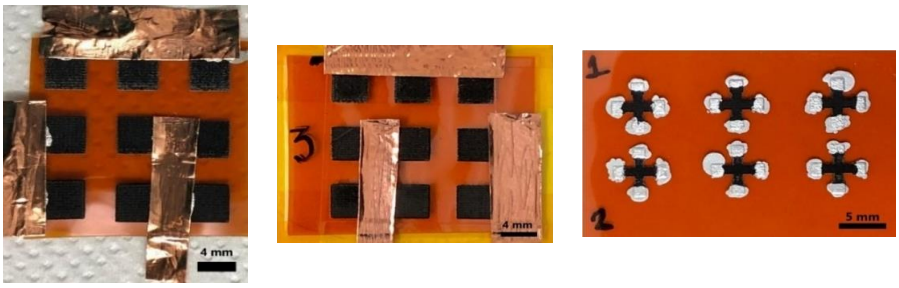

a. **b.** **c.**

Figure 4.4: *(a) LIG samples in square shapes used to perform SEM imaging. Copper adhesive tape was used to make conductive paths while Ag paste was employed to improve the contact between the conductive tape and the sample. The black scalebar corresponds to 4 mm. (b) LIG samples used to perform Raman spectroscopy. Copper adhesive tape was used to minimize the thermal effects induced by the laser when interacting with the LIG. The black scalebar corresponds to 4 mm. (c) LIG samples in cross shape used to perform the Van der Pauw measurement. Silver paste was used to minimize the resistance at probe-sample contact. The black bar corresponds to 5 mm.*

4.1.3 Characterizations

All fabricated samples were morphologically analyzed using SEM. To comprehensively represent the influence of all analyzed parameters — distance from the focal plane, rastering speed, and laser power — the samples marked with (*) in *Table 4.1* and *Table A1* were selected for further characterizations. These additional analyses aimed to evaluate physicochemical properties through Raman spectroscopy and the electrical properties through sheet resistivity measurements using the Van der Pauw method. The selected samples were chosen for their evenly spaced power, rastering speed, and lasing plane parameters, with increments of 0.4 W, 30 mm s^{-1}, and 1.5 mm, respectively.

Focus distance analysis

Figure 4.5 presents the SEM images obtained for samples S2-7.5, S2-6.0, and S2-4.5, which were selected as representative examples to investigate the effect of defocusing. These images were captured at a magnification of 500x. These images reveal the microstructural

differences in the prepared LIG. Sample S2-7.5, fabricated at the focal plane (*Figure 4.5 (a)*), exhibits complete graphitization but with less degassing, as evidenced by the dense areas. It is noteworthy that as the distance from the focal plane increases, the samples appear more homogeneous, more porous and display progressively less evident lasing lines (*Figures 4.5 (b) and (c)*). This is because, while laser fluence is highest at the focal plane and decreases with distance, a defocused laser beam irradiates the same spot multiple times due to the larger spot size, resulting in increased open porosity and degassing.

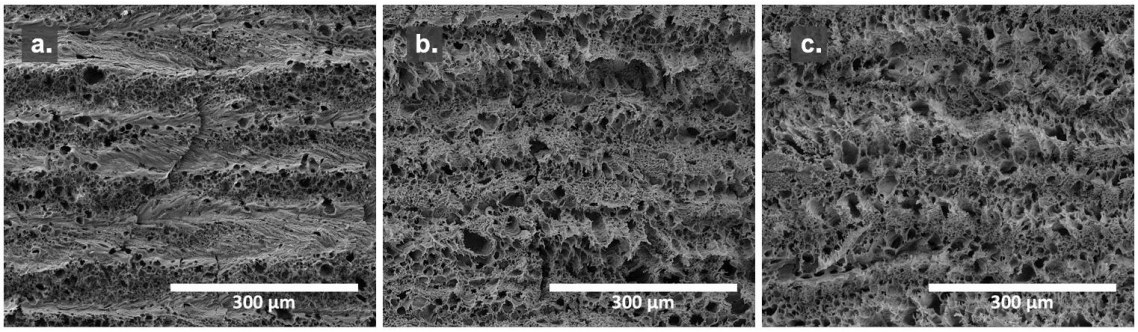

Figure 4.5: *SEM images of LIG samples produced using the same power and speed conditions and varying only the plane of irradiation. (a) S2-7.5, (b) S2-6.0, (c) S2-4.5. Magnification of 500x.*

Raman spectroscopy was utilized to evaluate the material quality of the fabricated samples. *Figure 4.6 (a)* presents the recorded spectra for the three samples, while *Figure 4.6 (b)* illustrates the I_D/I_G and I_{2D}/I_G ratios. Within LIG structures, three characteristic peaks can be identified: the D peak at 1300-1500 cm^{-1}, the G peak at 1500-1600 cm^{-1}, and the 2D peak at 2650-2700 cm^{-1} [92-93]. To compare the various structures obtained under different lasing parameters, the key parameters to be considered are the I_D/I_G ratio, which indicates the proportion of the defective to the crystalline regions, and the I_{2D}/I_G ratio, which provides insight into the number of graphene layers present. As observed in *Figure 4.6 (b),* the I_D/I_G ratio increases with the lasing distance from the focal plane, indicating a more defective graphene under these conditions. Given that polyimide is commonly used to produce LIG at the laser focal plane and that the lasing power and speed were optimized for y = 0, the increased I_D/I_G ratio with defocusing suggests the introduction of defects due to repeated irradiation of the same spot. Nevertheless, an I_{2D}/I_G ratio around 0.5 indicates the formation of high-quality multilayer graphene. This, along with high D peak intensities and I_D/I_G ratios of around 0.5-0.6, points to the presence of edge defects rather than functional groups or untransformed sp^3 carbon atoms, meaning that the graphitization process was successfully completed [102].

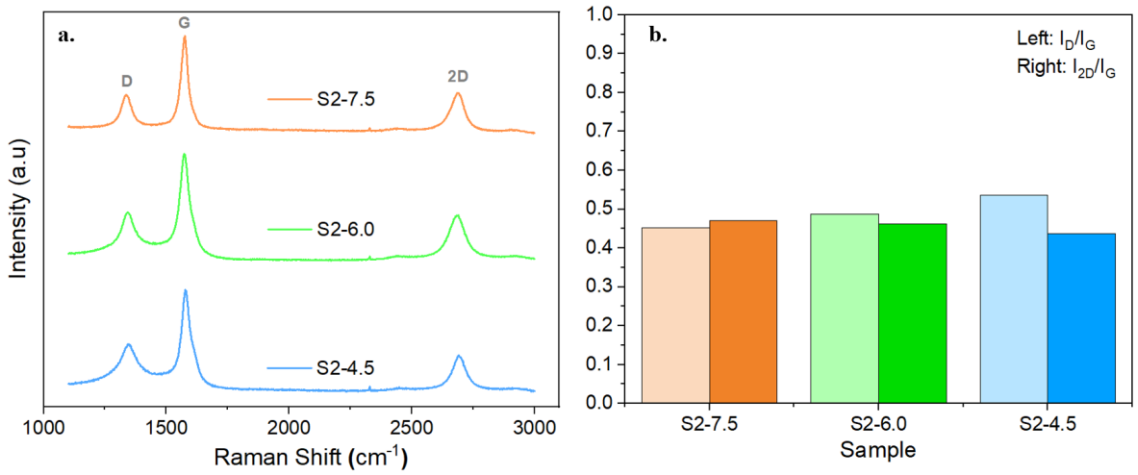

Figure 4.6: *(a) Stacked Raman spectra of the three samples selected to represent the influence of defocus. All the spectra are at the same scale, just displaced vertically to ease their visualization. Positions of D, G and 2D peaks are indicated. (b) Raman peak intensity ratios for each sample: I_D/I_G and I_{2D}/I_G.*

The Van der Pauw method was used to assess the sheet resistivity of the obtained samples. Three samples were tested for each condition to account for sample-to-sample variation. In *Figure 4.7* the mean sheet resistivity is displayed in colored squares and standard deviations are represented with black error bars.

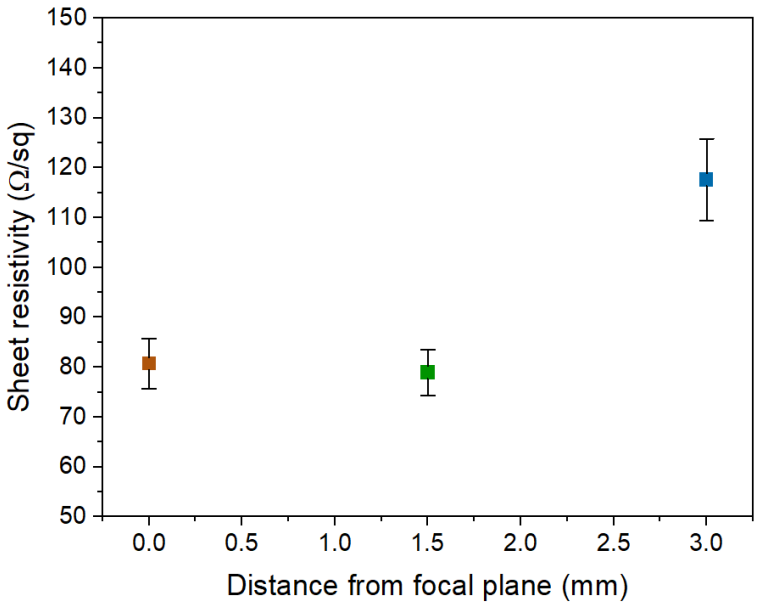

Figure 4.7: *The sheet resistivity of LIG samples was assessed using the Van der Pauw method. Error bars represent the standard deviation of the measurements.*

As expected from the I_D/I_G ratios, samples produced 3 mm below the focal plane are more resistive due to the lower fluence: the same power is spread over a larger spot size, delivering lower energy density to the substrate surface. For material obtained at the focal plane compared to that at -1.5 mm, the sheet resistivity is almost identical; however, a slight defocus results in slightly better conductivity. This could be explained by the fact that, even though the I_D/I_G ratio is higher for marginally defocused irradiated materials, the resulting surface is more homogeneous due to multiple irradiations of the same spot.

Power analysis

SEM images for samples illustrating the influence of lasing power on the resulting material are presented in *Figure 4.8*. Comparing *Figures 4.8 (a)*, *(b)* and *(c)* it can be argued that as the power decreases, the samples appear less homogeneous but also less damaged, with the laser-scribing direction and the characteristic C-shape derived from the laser spot that become more apparent. The degassing process in samples S-5.0-70 and S-6.0-70 appears to have been less intense than in sample S-7.0-70, as evidenced by the higher magnification images (*Figure 4.8 (g), (h), (i)*). The sample fabricated with higher laser power exhibits larger pores and more pronounced material removal. Since samples S-5.0-70 and S-6.0-70 were observed to be highly inhomogeneous, further imaging was conducted in the less porous areas (*Figure 4.8 (i), (k)*). At a magnification of 2000x, the denser regions of S-6.0-70 (*Figure 4.8 (i)*) display small pores, while S-5.0-70 (*Figure 4.8 (k)*) shows a thin layer of material covering underlying porosity. This difference can be attributed to the lower fluence at lower powers, resulting in reduced degassing.

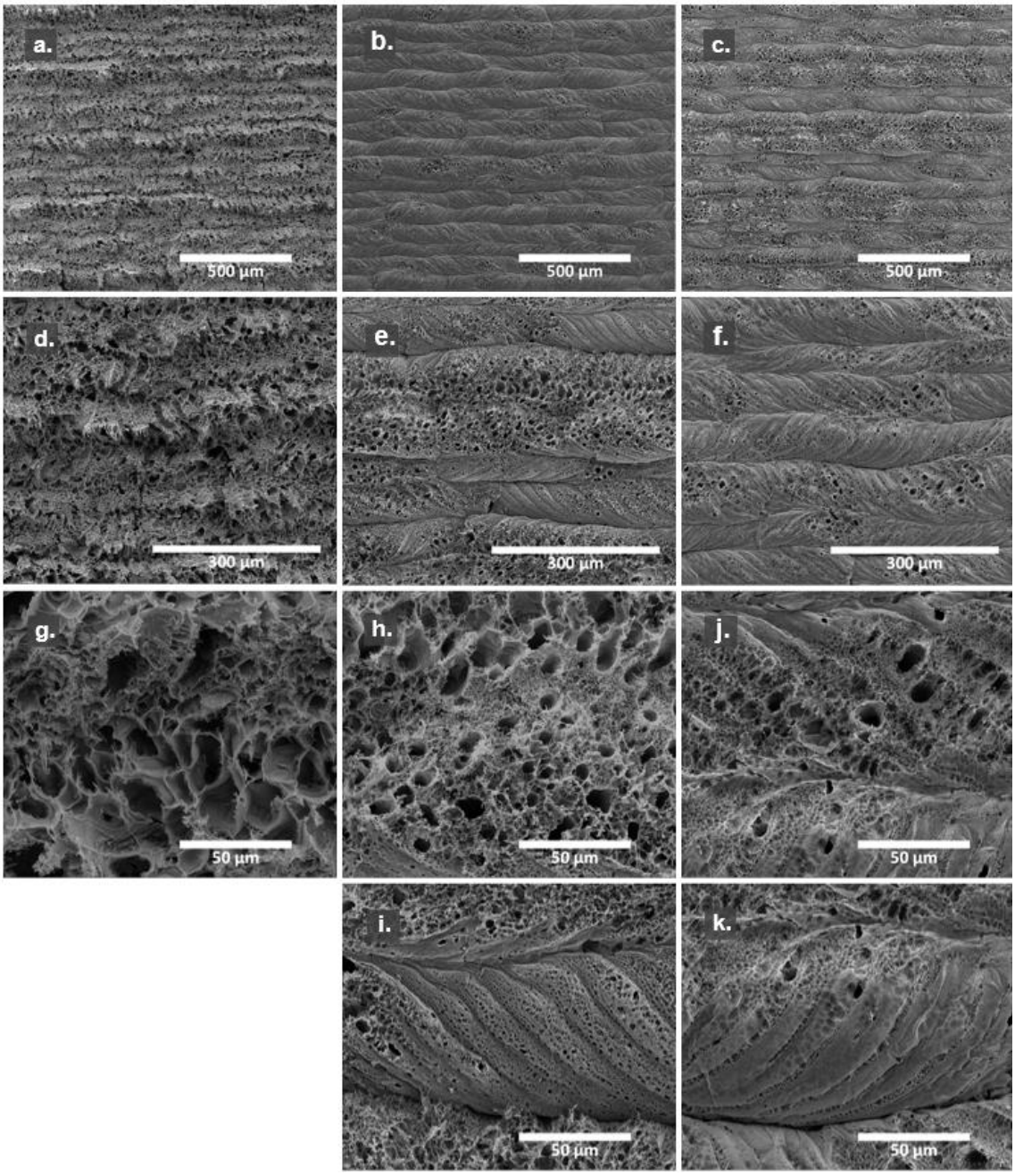

Figure 4.8: *SEM images of LIG samples produced at the same plane of irradiation using the same speed and varying only the power. (a) S-7.00-70, (b) S-6.0-70, (c) S-5.0-70. Magnification of 200x. (d) S-7.00-70, (e) S-6.0-70, (f) S-5.0-70. Magnification of 500x. (g) S-7.00-70; (h), (i) S-6.0-70; (j), (k) S-5.0-70. Magnification of 2000x.*

To evaluate the impact of lasing power on the LIG structure produced, Raman spectroscopy (*Figure 4.9 (a)*) was performed on samples fabricated at varying power levels while maintaining a constant rastering speed and distance from the focal plane. As indicated by the I_D/I_G and I_{2D}/I_G ratios (*Figure 4.9 (b)*), the lowest I_D/I_G ratio is observed for sample S-6.0-

70, indicating a higher quality of LIG compared to the other two samples. This could be because lower power levels introduce less damage to the material while still achieving a good degree of transformation. Conversely, increasing the power results in a higher degree of ablation and material damage due to structural degradation. This observation aligns with the SEM images, where sample S-7.0-70 (*Figure 4.8 (a), (d)*) is visibly more damaged than the other two samples processed at lower powers (*Figure 4.8 (b), (e)* and *Figure 4.8 (c), (e)*). Furthermore, considering the fraction of high-quality graphene, looking at I_{2D}/I_G ratios, sample S-6.0-70 again appears to be superior.

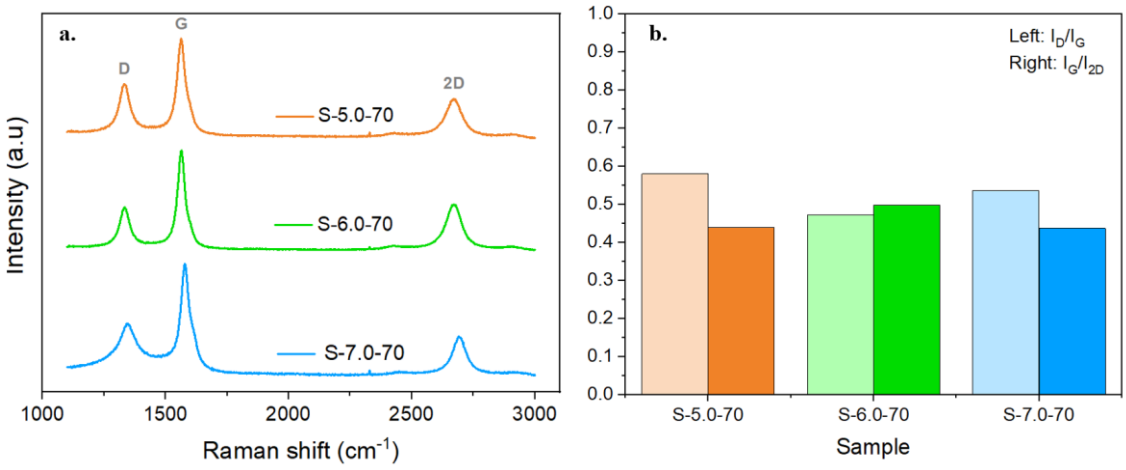

Figure 4.9: *(a) Stacked Raman spectra of the three samples selected to represent the influence of power. All the spectra are at the same scale, just displaced vertically to ease their visualization. Positions of D, G and 2D peaks are indicated. (b) Raman peak intensity ratios for each sample: I_D/I_G and I_{2D}/I_G.*

In terms of sheet resistivity, displayed in *Figure 4.10*, the values obtained at lasing powers of 6% and 7% are very similar. The lower conductivity observed for S-5.0-70 was expected due to the reduced graphitization resulting from lower energy densities delivered to the sample surface, as predicted by the I_D/I_G ratios in *Figure 4.9 (b)*. When comparing S-6.0-70 and S-7.0-70, the similar conductivities can be explained by their comparable degrees of graphitization.

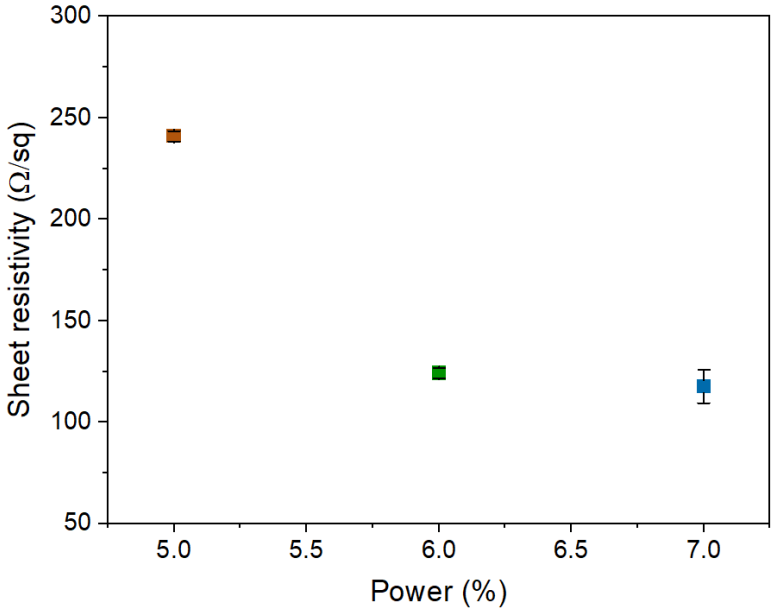

Figure 4.10: *The sheet resistivity of LIG samples was assessed using the Van der Pauw method. Error bars represent the standard deviation of the measurements.*

Speed analysis

The next step involved an analysis of the effect of rastering speed. For this purpose, samples fabricated at varying rastering speeds, while maintaining the same lasing power and focal plane distance, were characterized. *Figure 4.11* presents SEM images of the selected samples at various magnifications, highlighting the microstructural differences of LIG produced by varying scanning speeds while maintaining constant the lasing power and the defocus plane of -3 mm. At lower magnifications (*Figures 4.11 (a), (b),* and *(c)*), laser induced lines are visible in all samples. However, at lower scanning speeds, the characteristic C-shape indicating movement direction is absent. In all samples, the fluence was sufficient to graphitize the material and induce degassing, as evidenced by the visible porosity in *Figures 4.11 (j), (k),* and *(l)*. Additionally, the more porous areas cover larger regions, as observed in *Figures 4.11 (d), (e),* and *(f)*. The transformed material is continuous, yet each sample displays different degrees of heterogeneity. As the scanning speed decreases, the material appears more damaged and jagged, as clearly seen in *Figures 4.11 (f)* and *(i)*. Comparing *Figures 4.11 (g), (h)*, and *(i)*, the denser areas exhibit porosity covered by increasingly thicker layers of material as the speed decreases and fluence increases. This phenomenon could be attributed to a faster energy release on the surface at lower speeds, resulting in a higher substrate temperature. In the more porous areas (*Figures 4.11 (j), (k),* and *(l)*),

morphological changes are evident. The material transitions from well-defined pores to a string-like appearance with thinner walls separating the pores, and by *Figure 4.11 (l)*, the structure exhibits flake-like formations and larger cells, indicating more intense degassing.

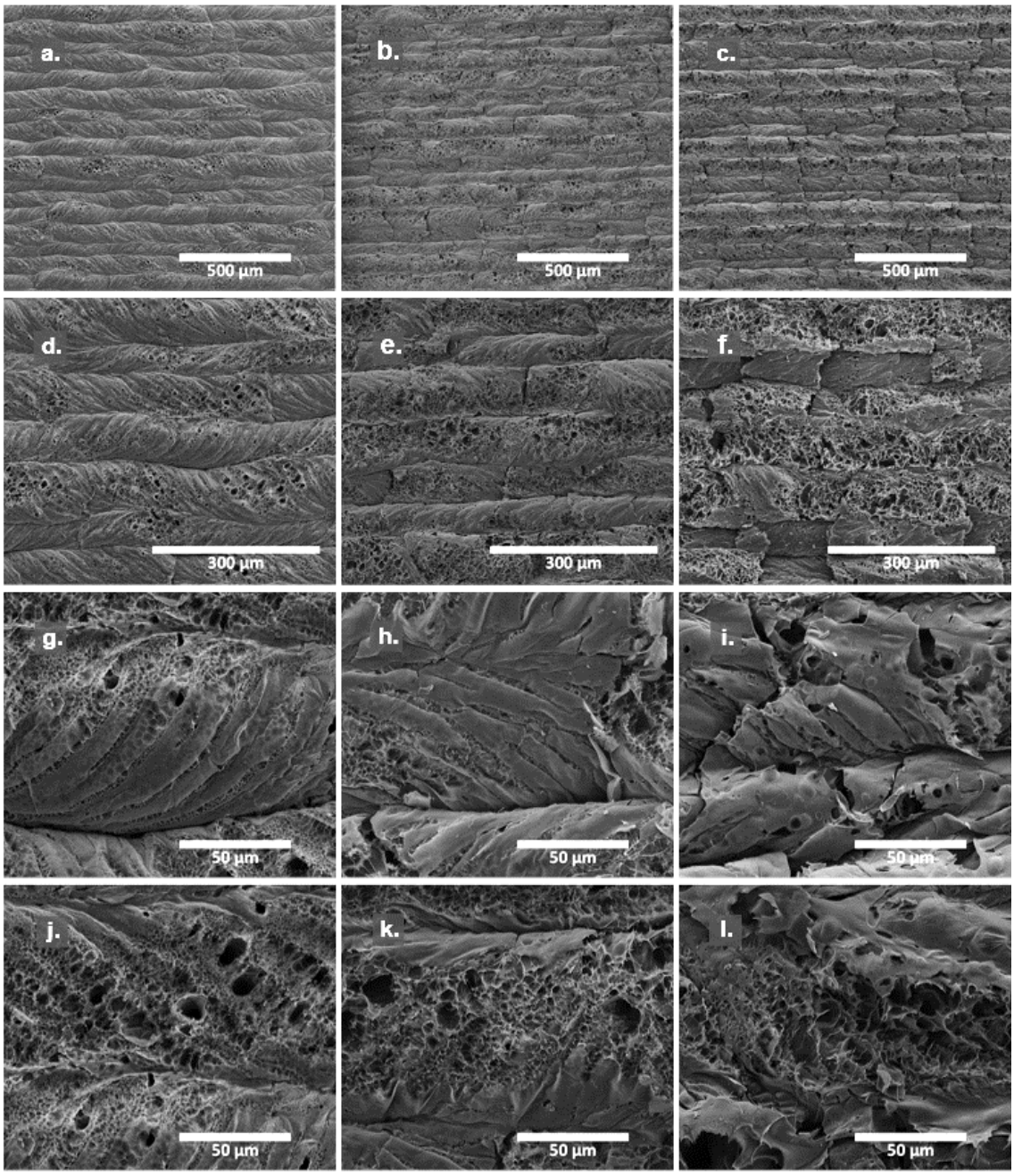

Figure 4.11: *SEM images of LIG samples produced at the same irradiating plane and at the same lasing power varying the scanning speed. (a) S-5.0-70, (b) S-5.0-40, (c) S-5.0-10. Magnification of 200x. (d) S-5.0-70, (e) S-5.0-40, (f) S-5.0-10. Magnification of 500x. (g) S-5.0-70, (h) S-5.0-40, (i) S-5.0-10. Lower porosity regions, magnification of 2000x. (j) S-5.0-70, (k) S-5.0-40, (l) S-5.0-10. Higher porosity regions, magnification of 2000x.*

Lower scanning speeds allow for longer irradiation times, resulting in higher energy delivery to the same spot and increased levels of graphitization, as seen in the Raman spectra in *Figure 4.12 (a)* and I_D/I_G, I_{2D}/I_G ratios in *Figure 4.12 (b)*. In all three Raman spectra, the three characteristic peaks of LIG can be observed, namely the D peak, the G peak, and the 2D peak. The I_D/I_G ratios suggest that higher graphitization degree is obtained in sample S-5.0-10 compared to other LIGs. This could be due to the prolonged exposure to the laser's energy flux achieved at lower speeds. The I_{2D}/I_G ratios also indicate that S-5.0-10 produces thicker, high-quality graphene. Comparing samples produced at 40 mm s^{-1} and 70 mm s^{-1}, it appears that higher quality graphene is achieved at faster speeds, possibly due to fewer defects being introduced into the material. The I_{2D}/I_G ratio around 0.5 across all samples anyway indicates the formation of high-quality multilayer graphene.

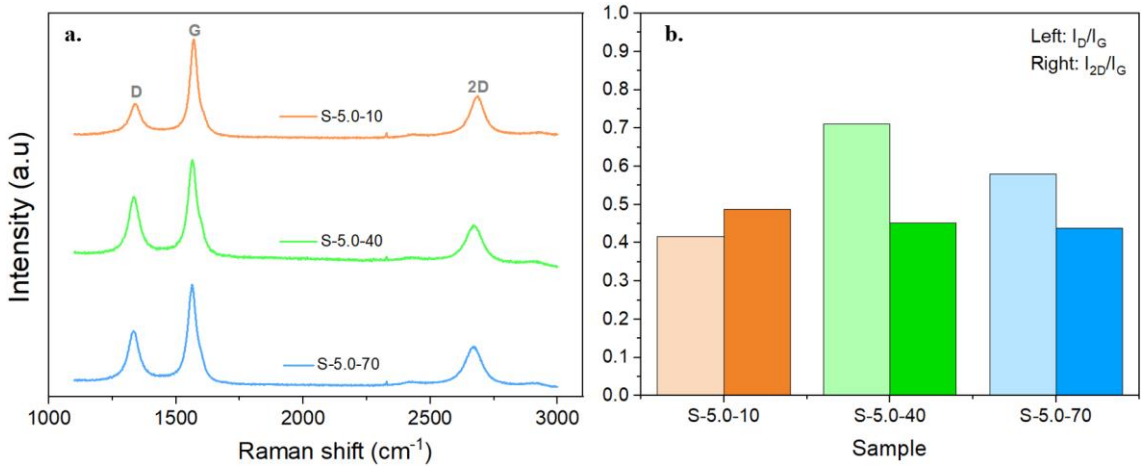

Figure 4.12: *(a) Stacked Raman spectra of the three samples selected to represent the influence of speed. All the spectra are at the same scale, just displaced vertically to ease their visualization. Positions of D, G and 2D peaks are indicated. (b) Raman peak intensity ratios for each sample: I_D/I_G and I_{2D}/I_G.*

Further measurements of sheet resistivity (*Figure 4.13*) confirm the best performance of LIG produced at lower speeds. Sample S-5.0-10 exhibits the lowest sheet resistivity, indicating superior quality. Conversely, sample S-5.0-40 has a lower sheet resistivity than sample S-5.0-70 but shows higher results dispersion. This may be due to lower speeds resulting in less ablation and fewer defects, though at the cost of reducing sample homogeneity, leading to variable performance.

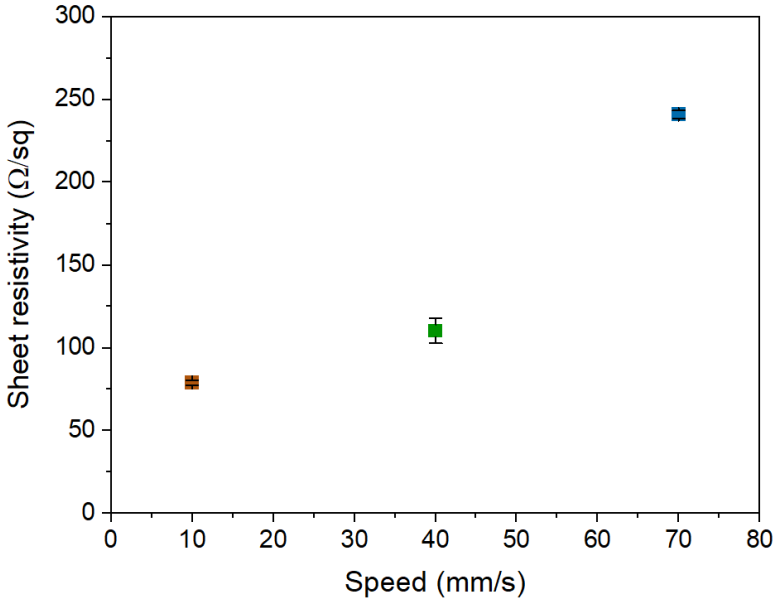

Figure 4.13: *The sheet resistivity of LIG samples was assessed using the Van der Pauw method. Error bars represent the standard deviation of the measurements.*

The key aspect of the initial part of this study was to investigate the effect of changes in fluence on the LIG produced through the lasing process, and how the various parameters determining fluence could impact the final properties, particularly morphology, structure, and electrical properties. It is important to emphasize the Gaussian shape characterizing the laser's intensity profile. This means that during scanning, the central part of the laser-scanned line is subjected to the highest peak energy density, while the periphery receives lower fluence. In the case of defocusing, this results in a secondary exposure of an area previously irradiated to an additional energy flux. Essentially, defocusing allows for irradiating the same point multiple times without altering the line separation or making additional laser passes. This approach yielded more homogeneous samples without the typical laser scribing lines, as shown in the SEM images in *Figure 4.5*. While a slight improvement in sheet resistivity was achieved with a minor defocus of -1.5 mm (78.9 ± 4.6 Ω/sq vs 80.7 ± 5.0 Ω/sq), as shown in *Figure 4.7*, higher defocus levels (-3 mm) did not yield similar results, indicating excessive material damage, possibly due to ablation, as suggested by Raman spectroscopy results (*Figure 4.6*).

Consequently, the decision was made to vary the laser power on this defocused plane and further investigate its effect, particularly by lowering power values while maintaining constant speed. The Raman spectroscopy results (*Figure 4.9*) indicated higher quality

graphene for sample S-5.0-70, but better electrical properties for samples produced at higher power, with comparable sheet resistivity of 124.2 ± 2.5 Ω/sq and 117.6 ± 8.2 Ω/sq (*Figure 4.10*) for samples S-6.0-70 and S-7.0-70 respectively.

Therefore, another parameter, speed, was investigated. This led, in sample S-5.0-10, to an improvement in graphene quality, as indicated by the I_D/I_G and I_{2D}/I_G ratios in *Figure 4.12 (b)*, and in electrical properties, with better sheet resistivity of 79.0 ± 1.6 Ω/sq (*Figure 4.13*), although there was a slight loss in sample homogeneity, as observed in the SEM images in *Figure 4.11*.

4.2 Laser induced graphene from cellulose acetate

4.2.1 Film and membranes fabrication

Initial attempts were made to fabricate cellulose acetate (CA) substrates in the laboratory for subsequent laser treatment. The films produced via spin coating, shown in *Figure 4.14 (a)*, were found to be extremely thin despite the ability to vary the thickness by adjusting the initial solution concentration and doing multiple spin coating processes. The films exhibited no changes following exposure to the CO_2 laser, indicating the absence of photothermal effects. Moreover, once power levels reached or exceeded 4%, the glass substrate began to be affected, which is not a desired effect. Attempts to soak these thin films in H_3PO_4 failed due to their minimal thickness and the high viscosity of the flame retardant, which further prevented laser interaction or material transformation.

In contrast, membranes produced via casting interacted effectively with the laser beam, as shown in *Figure 4.14 (b)*. These membranes were fabricated through a straightforward drop-casting technique using cellulose acetate solutions at varying concentrations in acetone, as previously described in Section 3. Two different drying processes were employed:

- Single-Step Drying: in this approach, the samples were left at room temperature for different durations, ensuring complete solvent evaporation within at least 6 hours. When exposed to laser power up to 4%, the material transitioned from complete transparency to partial opacity, which was attributed to laser-induced crystallization, causing partial reorganization of the material's structure [103]. At higher power

levels, the material exhibited melting and degradation, resulting in the formation of holes with black-brownish edges.

- Two-Step Drying Process: this method involved a two-stage drying process, with the first stage aimed at solvent removal and the second intended to induce chain reorganization [104]. The goal was to transform the material into a carbon phase rather than merely achieving polymer chain reorganization upon laser exposure. In this case, after initial air drying, the membranes were placed on a hot plate. Direct placement on the hot plate led to the formation of porous and inhomogeneous films (*Figure 4.14 (b-II)*).

Membranes only subjected to solvent evaporation underwent a change in opacity, shifting from transparent to opaque in areas exposed to the laser source. This phenomenon was attributed to the reorganization of polymer chains induced by the absorption of laser energy, as discussed earlier in Section 3. Conversely, membranes that underwent an additional annealing process were already translucent or opaque. When exposed to the CO_2 laser, these membranes exhibited a color change in the irradiated areas, transitioning from a translucent/white opaque to a yellowish/brownish hue.

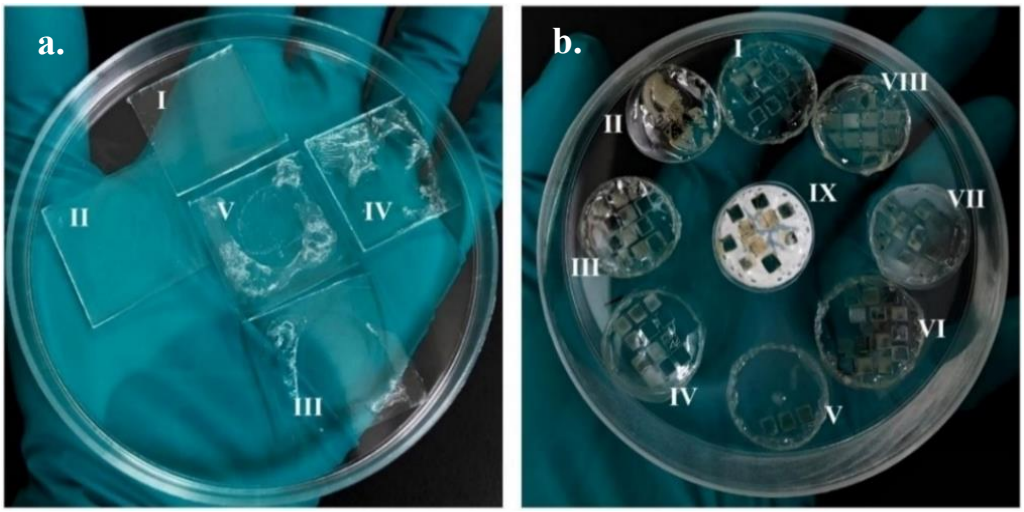

Figure 4.14: *(a) Films produced via spin coating with one (I, II), two (III) and three spin coating layers (IV, V). (b) Membranes produced via casting technique only dried (I, II, III, IV, V) and annealed (VI, VII, VIII, IX).*

Attempts to utilize phosphoric acid were unsuccessful due to the uncontrollable porosity of the membranes, which hindered laser-induced transformations. Additional challenges

included poor control over the thickness and uniformity of the cast films, limiting their effectiveness for laser processing.

4.2.2 Laser induced graphene from cellulose acetate commercial membranes

Manual drop casting often suffers from issues with reproducibility and deposition uniformity. For this reason, commercially available membranes were subsequently used to ensure more consistent and comparable results. Initially, laser writing was performed without any pretreatment, resulting in material degradation. Under varying lasing conditions, the untreated membranes exhibited holes and brown edges (*Figure 4.15*). Notably, the minimum power required for the material to display changes upon interaction with the laser was 3.5% (1.4 W).

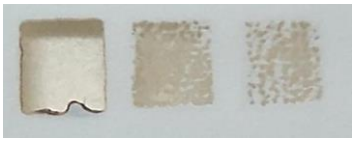

Figure 4.15: *Untreated cellulose acetate membranes exposed to laser irradiation at different lasing powers. It is possible to notice how the obtained material is characterized by holes and, at excessive power (on the left), by brownish edges due to the ablation and combustion of the material.*

When exposed to CO_2 laser radiation, the substrate undergoes photothermal processes, with local temperatures reaching up to 2000°C. In such conditions, untreated cellulose acetate degrades and volatilizes into CO_2, CO, and gaseous hydrocarbons. Since the process occurs in an ambient atmosphere with the presence of oxygen, the use of a fire retardant is the only effective way to prevent combustion of the material. Indeed, immersing the membranes in the flame retardant significantly improved their thermal properties.

The treated membranes were placed on laboratory glass slides previously cleaned with isopropanol, and then subjected to laser writing. It was observed that the minimum power required to achieve material transformation was 4% (1.6 W). Lasing conditions on the focal plane were varied, with power settings ranging from 4% (1.6 W) to 6% (2.4 W) in 0.5% increments and speeds from 10 to 100 mm s^{-1} in 10 mm s^{-1} increments. Samples produced in the most promising window of parameters in the focal plane are showed in *Figure 4.16*. A power setting of 4.5% at a speed of 10 mm s^{-1} yielded the best results, producing black squares with minimal damage to the glass substrate.

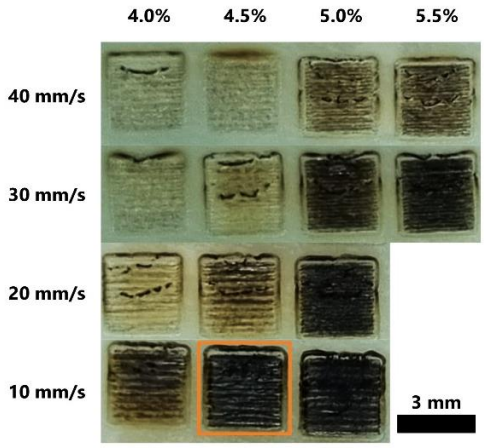

Figure 4.16: *Some of the samples produced at the focal plane during the dosing test. The lasing conditions were varied in terms of power (ranging from 4% to 6%) and speed (ranging from 10 to 100 mm s^{-1}, adjusted to achieve material transformation without complete ablation). The sample that yielded the optimal result, characterized by maximal blackness and substrate integrity, is highlighted by an orange square.*

A further increase in scan speed over 40 mm s^{-1} resulted in incomplete material transformation, though the material was still affected by laser interaction because of photothermal effects. Subsequently, the focal plane was changed to assess the quality of the material obtained under these conditions. The lasing plane was adjusted using aluminum bases of 4.5 mm and 3.5 mm thickness, and finally using the laser's own plane, positioned 7.5 mm below the focal plane. Samples to be analyzed were produced taking as writing conditions the ones that led to the blackest samples on the focal plane. *Table 4.2* shows the conditions and the corresponding names of the samples produced with only one pass.

Table 4.2: *Detailed laser parameters for samples fabricated in a single pass. All samples were irradiated at a power of 4.5% and speed of 10 mm s^{-1}. Sample names indicate lasing plane and speed of scribing.*

Sample	Power (%)	Speed (mm s^{-1})	Base thickness (mm)
S1-7.5-10	4.5	10	7.5
S1-4.5-10			4.5
S1-3.5-10			3.5
S1-0-10			0

Following these tests, the double pass technique was implemented. To understand the effect of irradiating energy on the material, several tests were conducted. For each plane considered, the first and second passes were performed at the same power (4.5%) while

varying the speeds. In each series, the speed of the first pass was varied between 10 and 30 mm s^{-1} in 10 mm s^{-1} increments, while the speed for the second pass was kept constant. The employed conditions are shown in *Table A2*. Preliminary observations with naked eye revealed that samples produced with a single pass were black only at a speed of 10 mm s^{-1}. In the case of double pass technique, several factors were considered:

- The material transformation was assessed by the black color, indicating a successful qualitative transformation into a porous, graphene-like or carbonaceous material;
- The quality and homogeneity of the material were evaluated at the optical microscope, ensuring that the material remained intact without breaking;
- The extent of damage to the glass substrate was considered by means of optical microscopy inspection. Given the extreme thinness of the membranes, it was nearly impossible to avoid affecting the support, but minimizing this aspect was crucial for LIG synthesis.

Based on these considerations and for the sake of consistency, the selected conditions for further characterizations were, for each plane: 4.5% of power, 10 mm s^{-1} for the first pass, and 30 mm s^{-1} for the second pass, as flagged by the asterisk (*) in *Table A2* and an orange square in *Figure 4.17*.

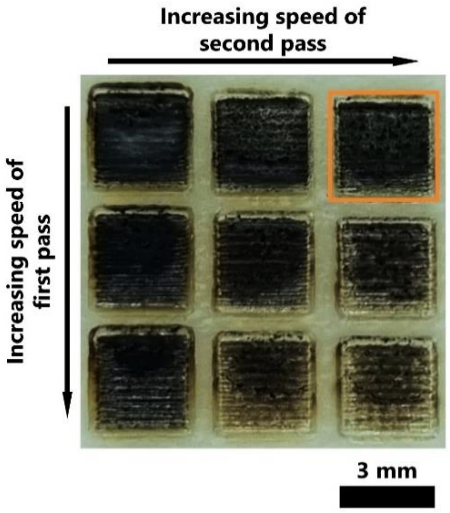

Figure 4.17: *Samples obtained at the focal plane using the double pass technique. The arrows indicate the direction and sequence of speed variation for either the first or second pass. For each set of samples produced by altering the lasing plane, the selected sample was fabricated with the first pass at the minimum speed (10 mm s^{-1}) and the second pass at the maximum speed (30 mm s^{-1}). These conditions are highlighted by an orange square in the figure.*

One of the initial characteristics observed in the obtained material is its ease of being peeled off, as demonstrated in *Figure 4.18*. Following the lasing process, the untransformed membrane can be easily and immediately separated from the transformed portion without the use of any release agents or solvents.

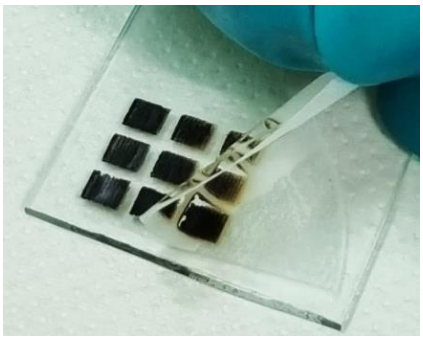

Figure 4.18: *Easy peel-off of the untransformed CA membrane from the lased parts.*

SEM and Raman samples were prepared as 3 mm x 3 mm squares. For the SEM samples, space between squares was filled with conductive silver paste to mitigate the accumulation of electrostatic charge induced by beam illumination. This step was crucial to minimize imaging issues, particularly given the presence of a glass insulating substrate and thin LIG structures. Copper adhesive tape was then applied to ensure efficient discharge of the charge onto the metallic sample holder. The sample setup is depicted in *Figure 4.19*.

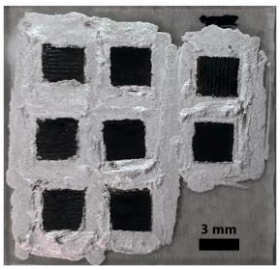

Figure 4.19: *LIG samples obtained from CA used to perform SEM imaging. Silver paste was used to minimize charging and imaging issues while copper tape was used to discharge the charge onto the sample holder. Scalebar corresponds to 3 mm.*

For Raman analysis, each sample was initially provided with a metallic contact with the substrate using copper tape to prevent thermal energy accumulation from laser exposure. Due to the extreme thinness of the material, the resulting spectra were dominated by signals from the glass substrate. To accurately assess material quality, a spatula was used to reduce the samples into powder. To avoid contamination, the spatula was cleaned with isopropanol

before processing each sample. The powdered samples were then placed on a copper substrate (*Figure 4.20*), as previously reported in the literature [77, 102]. This approach enabled the acquisition of sharp material signals and efficient thermal energy dissipation.

Figure 4.20: *Sample reduced into powder placed on a copper substrate to minimize background signal and thermal energy accumulation. A cleaned spatula was used to reduce each sample into powder.*

The samples for the Van der Pauw method were prepared as previously described and are shown in *Figure 4.21*. Silver paste was used to minimize the contact resistance between the

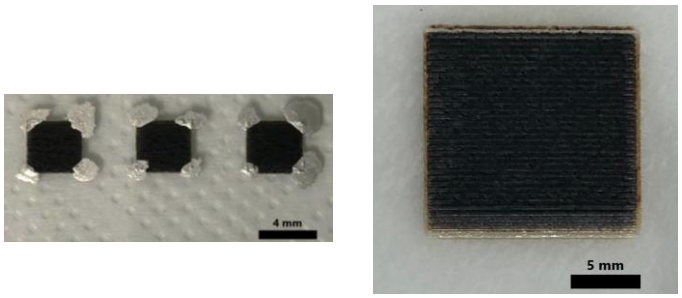

a. **b.**

probe and the sample. The wettability test samples were prepared as 1.5 cm x 1.5 cm squares to provide a sufficiently large area to accommodate the droplet. An example of wettability test sample is shown in *Figure 4.21 (b)*.

Figure 4.21: *(a) LIG samples in square shape used to perform the Van der Pauw measurement. Silver paste was used to minimize the resistance at probe-sample contact. (b) Sample for wettability test. Scalebar corresponds to 5 mm.*

4.2.3 Characterizations

The samples produced after narrowing the parameter range to achieve material continuity without substrate ablation were characterized using various techniques. The lasing conditions for these samples involved a laser power of 4.5%, with a scanning speed of 10 mm s^{-1} for the first pass and 30 mm s^{-1} for the second pass, while the distance from the focal

plane was varied from 0 to 7.5 mm. A first assessment of the quality of the material was performed through Raman spectroscopy, then morphological analyses were conducted using scanning electron microscopy (SEM). The electrical properties were evaluated using Van der Pauw measurements, and the hydrophobicity/hydrophilicity of the material was tested through wettability measurements.

The Raman spectra of samples produced with a single laser pass are shown in *Figure 4.22 (a)*, while the corresponding I_D/I_G ratios are displayed in *Figure 4.22 (b).* As observed from the Raman spectra, none of the samples exhibit the 2D peak characteristic of graphene-like structures. However, distinct and well-defined D and G peaks are evident in samples S1-3.5-10 and S1-4.5-10, which were fabricated at distances of -3 mm and -4 mm from the focal plane, respectively, as well as in sample S1-7.5-10, which was fabricated directly at the focal plane. Based on the literature [94, 105-106], these findings suggest that the resulting material is graphene oxide (GO), a two-dimensional carbon material featuring oxygen-containing functional groups (e.g., =O, -OH, -O-, -COOH) attached to both the basal planes and the edges of the layers [107]. In contrast, the spectrum of the sample S1-0-10, obtained with greater defocus, shows a higher convolution of the D and G peaks, suggesting the formation of a material with a higher content of amorphous carbon than sp^2-hybridized carbon in an ordered structure [94]. In order to compare the different structures obtained, the I_D/I_G ratio (*Figure 4.22 (b)*) must be taken into consideration. It is possible to observe that for the GO structures obtained, the ratio is roughly equal to 1 with very small fluctuations. While GO is a highly disordered system with both sp^2 and sp^3 C atoms, a comparison can still be performed between the different samples. Lower I_D/I_G ratios indicate a higher order in the stacked GO sheets, making S1-45-10 the best one with a value of I_D/I_G ratio of 0.94. In the case of S1-0-10 sample, even if the I_D/I_G ratio results to be lower, the quality of the material obtained can be said to be the worst compared to the others because of the higher convolution of the D and G peaks which make the resulting spectrum more similar to the amorphous-carbon spectrum than GO. This might be due to the fact that at the focal plane the energy density delivered onto the sample surface is higher, thus introducing a greater concentration of defects. When defocusing, instead the spot size increases thus decreasing the areal energy density, giving a better-quality material as a result. Eventually, the lowering in the energy density caused by a farther distance from the focal plane results in a less transformed material, as it happens with sample S1-0-10.

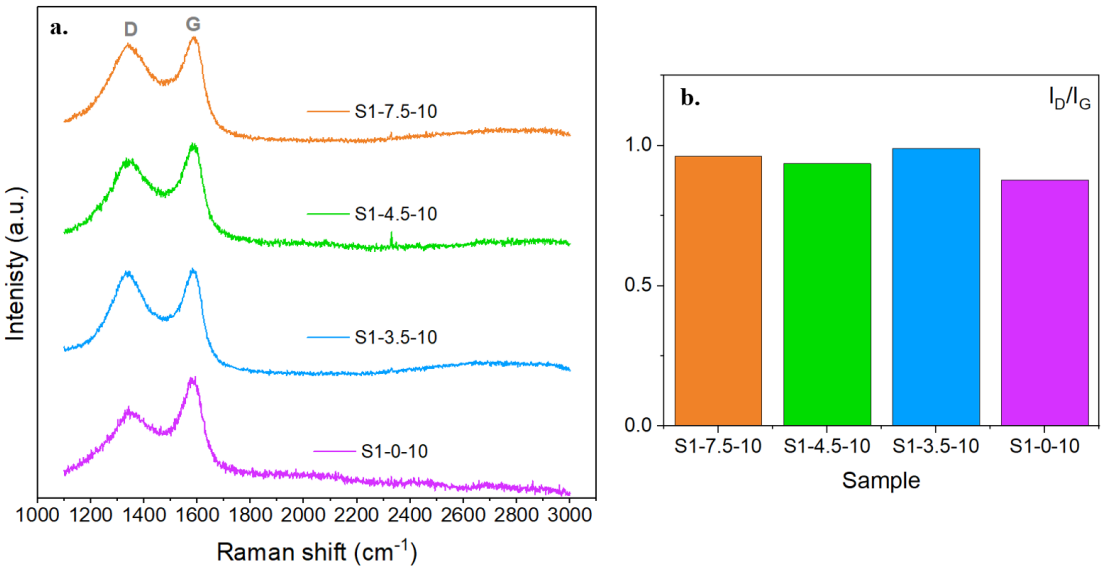

Figure 4.22: *(a) Stacked Raman spectra of samples produced lasing a CA commercial membrane with a power of 4.5% and speed of 10 mm s^{-1} at different distances from the focal plane. All the spectra are at the same scale, just displaced vertically to ease their visualization. Positions of D and G peaks are indicated. (b) Raman I_D/I_G peak intensity ratios for each sample.*

A more thorough understanding of the transformation process can be derived from scanning electron microscopy images. *Figure 4.23* illustrates the CA membrane prior to laser scribing process. Initially, the membrane exhibits a net structure with elements approximately 200 nm in size, characterized by spherical components of 500 nm. These structures do not appear to be highly compressed and exhibit a uniformly distributed porosity ranging from 500 nm to 1 µm.

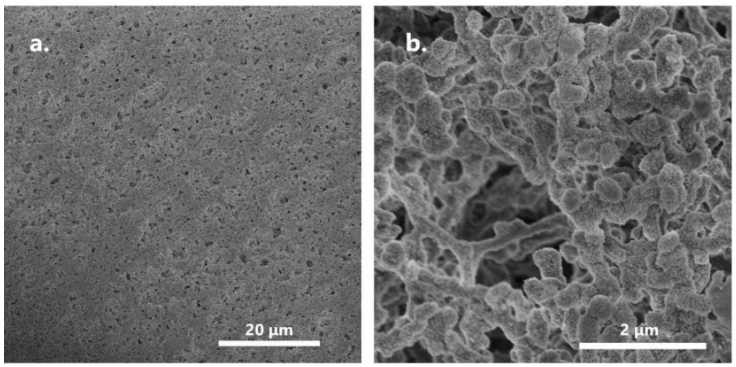

Figure 4.23: *SEM images of untreated cellulose acetate (CA) membranes. (a) 1200x magnification (b) 15000x magnification*

However, after the initial laser irradiation, the structure becomes denser (*Figure 4.24*). Notably, the morphology of samples S1-7.5-10, S1-4.5-10, and S1-3.5-10 is remarkably similar, corroborating the similarities observed in their Raman spectra. Conversely, sample S1-0-10, which exhibits a distinct Raman spectrum, also shows a different morphology. This can be explained by suggesting the formation of graphene oxide, rich in functional groups containing hydrogen and oxygen, near the focal plane. These functional groups facilitate inter- and intramolecular forces, such as hydrogen bonds, between different layers. At greater distances from the focal plane, the lower energy absorbed by the material precludes the formation of such chemical species, resulting instead in a carbon-rich material poorer in oxidized groups. Nevertheless, the aggregation in these conditions is higher than in the untreated sample, indicating that the material begins to transform even at reduced fluency levels.

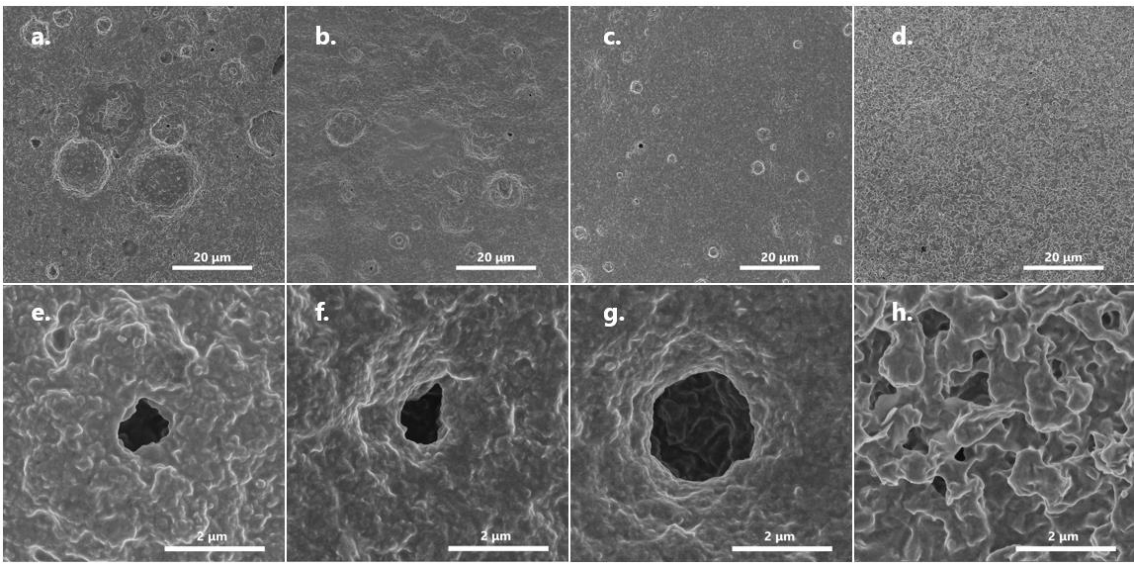

Figure 4.24: *SEM images at different magnifications of samples produced with single pass technique on cellulose acetate commercial membranes. Power (4.5%) and speed (10 mm s^{-1}) are the same for all the samples while the lasing plane was varied. Base thickness: 7.5 mm (a)1200x, (e) 15000x; 4.5 mm (b) 1200x; (f)15000x; 3.5 mm (c) 1200x, (g) 15000x; 0 mm (d) 1200x, (h) 15000x.*

Figure 4.25 (a) presents the Raman spectra of samples obtained with the double pass technique at different distances from the focal plane. The presence of a well-defined G-peak and the further presence of a distinguished D-peak in all the samples suggests the successful transformation of the sp^3 bonds present in the starting material into sp^2-type bonds and the formation of a 2D hexagonal structure [108]. Notably, samples S2-3.5-13, S2-4.5-13, and

S2-7.5-13 exhibit sharp, well-defined peaks with minimal overlap. Additionally, the appearance of the 2D and D+G peaks indicate the proper formation of laser induced graphene (LIG). The 2D peak is characteristic of graphene structures, while the D+G peak is indicative of highly disordered graphene-like structures [92]. In contrast, sample S2-0-13, produced at greater defocus conditions, exhibits greater overlap of the D and G peaks and a broad, indistinct 2D peak, suggesting the formation of a less ordered, graphene-like two-dimensional structure, more akin to graphene oxide (GO) at greater defocus. Examining the I_D/I_G ratios in *Figure 4.25 (b)*, it is evident that sample S2-4.5-13, produced with a defocus of -3 mm, has the lowest ratio of 1.01, indicating the highest degree of order and suggesting significant reordering and reduction upon the second irradiation process [106]. When analyzing the I_{2D}/I_G ratio for samples with a sharp and well-defined 2D peak, the highest ratio of 0.57 is found in sample S2-4.5-13. This suggests that these conditions produce the thickest and highest-quality graphene-like material. The optimal synthesis conditions strike a balance between introducing fewer defects into the structure and ensuring the proper transformation of the material. This can be achieved by increasing the spot size to distribute the laser beam energy over a larger area. The resulting spectra obtained, and the I_D/I_G ratios are comparable with the ones in literature obtained from the work of Jung et al. [108].

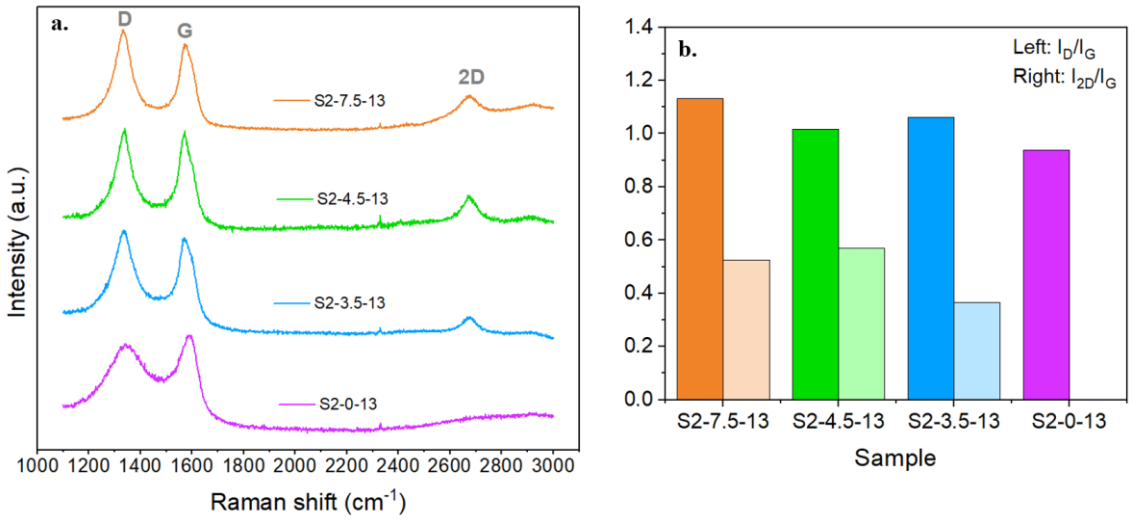

Figure 4.25: *(a) Stacked Raman spectra of samples obtained from the lasing process of CA commercial membranes with a power of 45% and double pass technique. All the spectra are at the same scale, just displaced vertically to ease their visualization. Positions of D, G and 2D peaks are indicated. (b) Corresponding Raman I_D/I_G peak intensity ratios for each sample and when possible, I_{2D}/I_G ratio.*

The morphological analysis conducted through SEM imaging is presented in *Figure 4.26.* The SEM images confirm the transformation of the substrate into LIG, as they reveal a high degree of porosity induced by the degassing process, particularly in samples produced at or near the focal plane (*Figures 4.26 (a), (b)*, and *(c)*). In contrast, the morphology of the sample processed at a greater defocus distance (-7.5 mm) exhibits a randomly and uniformly distributed porosity, ranging from 2 to 10 μm, along with a granular structure (*Figure 4.26 (d)*).

Sample S2-7.5-13 produced at the focal plane appears denser with less pronounced porosity compared to S2-4.5-13 and S2-3.5-13, fabricated under defocus conditions. At lower magnifications, samples lased close to the focal plane (*Figures 4.26 (b)* and *(c)*) display notable similarities, characterized by a highly porous structure with thin, interconnected, network-like features. At higher magnifications, the sample produced at the focal plane exhibits a smoother surface (*Figure 4.26 (e)*) compared to samples S2-4.5-13 and S2-3.5-13, which demonstrate increased surface roughness (*Figures 4.26(f)* and *(g)*). Conversely, sample S2-0-13, produced under greater defocus conditions, shows a homogeneous and smooth surface with visible particle agglomerates at higher magnification (*Figure 4.26 (h)*), corroborating the successful formation of graphene oxide (GO).

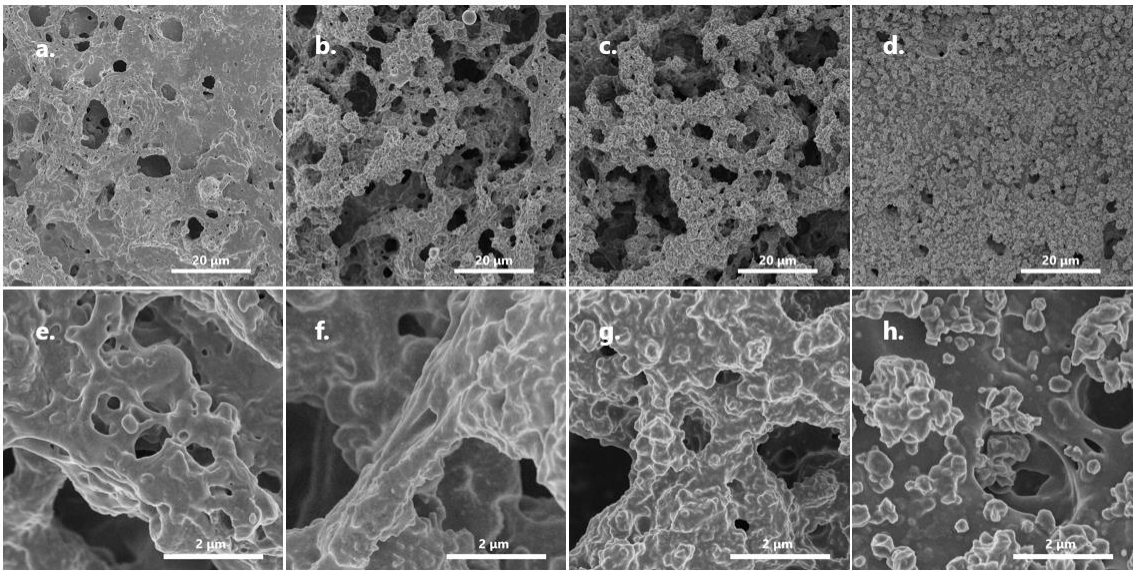

Figure 4.26: *SEM images taken at different magnifications of samples produced with the double pass technique. All samples were obtained at lasing power of 4.5% and scanning speed of 10 mm s^{-1} for the first pass and 30 mm s^{-1} for the second one. The base thickness was varied to change the lasing plane. Magnification of 1200x: (a) 7.5 mm (b) 4.5 mm, (c) 3.5 mm, (d) 0 mm. Magnification of 15000x: (e) 7.5 mm, (f) 4.5 mm, (g) 3.5 mm, (h) 0 mm.*

Comparing the Raman spectroscopy results with the morphological analysis of samples produced by single and double passes allows for a description of the material's evolution. *Figures 4.22 (a)* and *Figure 4.25 (a)* reveal that when the material is closer to the focal plane, it undergoes a more effective transformation: the graphene oxide (GO) formed during the first pass is subsequently reduced to LIG in the second pass. Additionally, the GO characterized by a high degree of order formed in a single pass with a 3 mm defocus (S1-4.5-10) facilitates the production of a more ordered structure in the second pass. Conversely, material produced further from the focal plane yields lower quality in both single and double passes.

These findings were corroborated by the SEM images. Samples showing the highest particle aggregation, with continuous surfaces characterized by few open pores and some protrusions likely resulting from closed porosity, can be retraced to GO formation (*Figure 24 (e)-(g)*). In contrast, the formation of amorphous carbon in sample S1-0-10 results in a morphology very similar to the initial one (*Figure 23 (b)* and *Figure 24 (h)*) and similar to the amorphous carbon morphologies reported in literature [109]. Following the double pass, the formed GO is reduced, with gasification producing significantly elevated porosity. Notably, sample S2-7.5-13 exhibits a lower degree of porosity compared to S2-4.5-13 and S2-3.5-13 (*Figure 26 (a)-(c)*), and is also characterized by a higher degree of disorder, indicating a lesser extent of material reduction. This is further evidenced by the thicker structures observed at a 4 mm defocus (approximately 2 μm), compared to those at 3 mm below the focal plane (roughly 700 nm), which also displayed a lower I_D/I_G ratio. At greater defocus distances, sample produced at -7.5 mm of defocus is characterized by particle aggregates that emerge from a relatively smooth surface, likely due to the formation of graphene oxide following the second radiation exposure.

To assess the macroscopic electrical properties of the samples, the Van der Pauw method was employed. The minimal thickness of the LIG achieved coupled with the high resistance of the material hindered the extraction of significant curves for evaluating the sheet resistivity. However, the conductivity of the LIG produced at -3 mm from the focal plane, designated as sample S2-4.5-13, was successfully measured. The results are shown in *Figure 4.27*.

It is important to note that, using the previously described analysis configurations (Section 3.2.4), sheet resistivities of 416.0 ± 41.5 Ω/sq in the direction parallel to the laser writing and of 1758.6 ± 49.5 Ω/sq in the perpendicular direction were detected. Both of these results are aligned with values found in the literature for other non-aromatic green substrates [62] [108, 110]. This indicates that the writing direction is crucial, resulting in substantial inhomogeneity in the conductive pathways within the material. The significantly higher resistivity perpendicular to the writing direction suggests a lack of effective conductive networks between successive written lines. The laser's passage and the induced photothermal effects lead to the formation of graphene-like material in the second writing pass; however, the peripheral areas of the spot size probably do not undergo the same transformation as the center, resulting in decreased electrical connectivity between successive written lines.

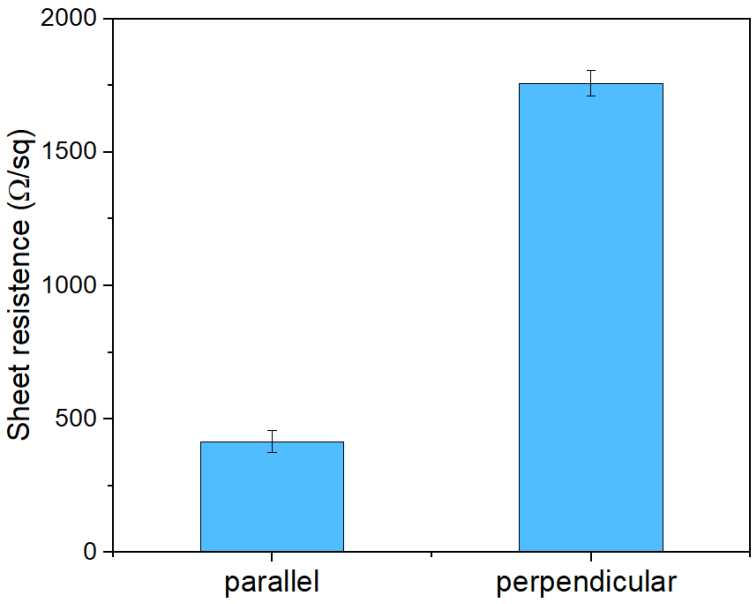

Figure 4.27: *Sheet resistivity resulting from Van der Pauw measurement. Very different values are obtained when considering the parallel direction to the laser writing process and the normal one. Standard deviation is also reported.*

To evaluate the surface properties of the carbonaceous materials obtained through laser writing, the static sessile drop method was used. All conditions exhibited hydrophilic behavior, with contact angles below 90°, as it is possible to observe in *Figure 4.28*.

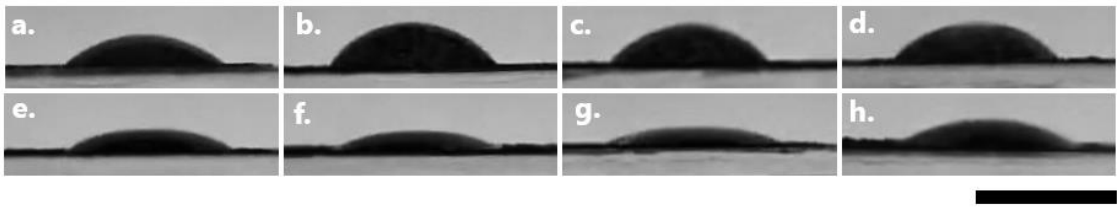

Figure 4.28: *De-ionized water drops onto LIG samples produced in different lasing conditions. Samples produced with single pass, 4.5% of power, 10 mm s^{-1} of scan speed while varying the lasing plane: (a) S1-7.5-10, (b) S1-4.5-10, (c) S1-3.5-10, (d) S1-0-10. Samples produced with the double pass technique, 4.5% of power, 10 mm s^{-1} of scan speed for the first pass, 30 mm s^{-1} for the second pass: (e) S2-7.5-13, (f) S2-4.5-13, (g) S2-3.5-13, (h) S2-0-13. Scalebar correspond to 5 mm.*

Figure 4.29 shows the contact angle trends following the first and second laser writing. The values obtained after the first writing pass were higher for all samples compared to the second pass. Since cellulose acetate is a hydrophilic material with a contact angle of 37.6° [111] the hydrophilicity of the resulting LIG is not surprising. Furthermore, laser writing in ambient conditions typically produces hydrophilic/super-hydrophilic LIG, as confirmed in the literature [112-114]. For each series, the analyzed samples were produced using the same power (4.5 %) and speed conditions (10 mm s^{-1} for single pass; 10 mm s^{-1} for the first pass, 30 mm s^{-1} for the second pass in the case of double pass technique) while varying the base thickness and, hence, the distance from the focal plane.

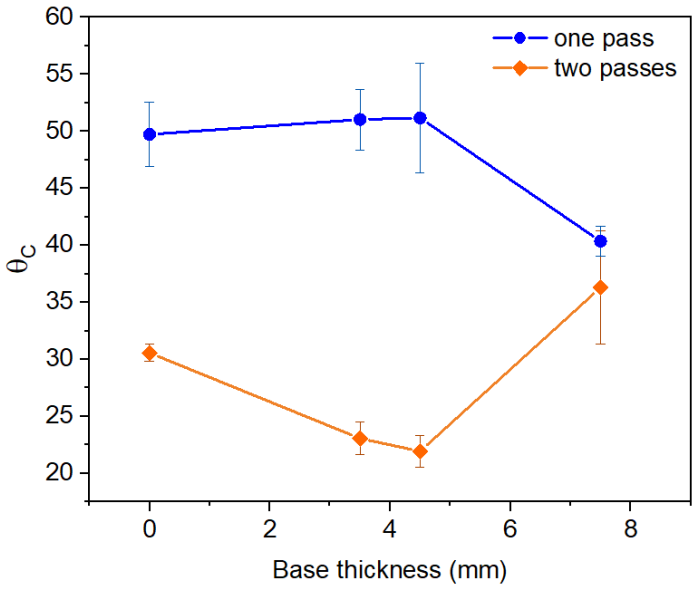

Figure 4.29: *Trend of the contact angles measured through static sessile drop method. The blue dots and orange squares illustrate the average values obtained from three distinct. Error bars represent the standard deviation of the measurements.*

For samples produced up to 4 mm below the focal plane, the decrease in contact angle after the second writing can be attributed to the dual effects of the laser: while, on one hand, the high temperatures induced by photothermal effects induce graphitization of the material by reducing it, the oxygen in the air reacts with the carbon atoms, leading to the formation of new oxygen-containing, hydrophilic groups. Notably, similar values were obtained for the three samples after the first pass, around 50° [115]; after the second pass, samples S2-4.5-13 and S2-3.5-13 exhibited very similar contact angles (21.9° ± 1.4 and 23.0° ± 1.4 respectively), about 10° lower than the sample produced on the focal plane. This is mainly due to the material's morphology, which is much more porous in these two samples than in the other, as seen in the SEM images in *Figure 4.26 (a), (b), (c)*. This increased porosity enhances the wettability in samples S2-4.5-13 and S2-3.5-15, as according to Wenzel's derivation, greater surface roughness increases hydrophilicity (or hydrophobicity if the material is initially hydrophobic) [116-117].

For the sample produced at the base of the laser (S2-7.5-13), 7.5 mm below the focal plane, the contact angle significantly differs from the other samples in both the first and second passes. The first pass results in amorphous carbon, as suggested by the Raman spectra and corroborated by a contact angle of about 40° (36.3° ± 4.9), consistent with literature values for measurements at room temperature [109]. The second pass leads to minimal changes in the contact angle. From the Raman spectrum in *Figure 4.25 (a)*, the formation of GO is evident in the sample obtained with two passes at 7.5 mm below the focal plane. Therefore, a contact angle similar to those of samples S1-7.5-13, S1-4.5-13, and S2-3.5-13 would be expected. The difference with these values can be reasonably explained by the varying morphologies of the obtained materials: the sample produced with two passes at farther distance from the focal plane (*Figure 4.26 (d)*) is more porous than the ones produced with a single pass closer to the focal plane (*Figure 4.24 (a), (b), (c)*), and this enhances the wettability as previously stated.

The characterization of materials obtained using different lasing parameters provided significant insights into the transformation mechanisms of the polymeric substrate under laser irradiation at various distances from the focal plane. It is essential to highlight the lasing conditions employed for the two laser writing passes: the first pass was conducted at a lower

scanning speed (10 mm s^{-1}), followed by a second pass at a higher scanning speed (30 mm s^{-1}). Both scribing processes were executed at 4.5% of power.

This dual-pass approach was necessary to initially supply sufficient energy to transform the sp^3-hybridized carbons in the hexagonal cyclic structures of cellulose acetate (CA) into sp^2-hybridized carbons during the first lasing pass. Closer to the focal plane, the more intense photothermal effects of the initial raster induce a reorganization of carbons into ordered clusters of aromatic rings, although with a high number of defects and sp^3 carbons bonded to oxygen-containing groups, resulting in the formation of graphene oxide, as inferred from Raman spectra and confirmed by SEM images and wettability tests. The second laser pass delivers lower energy to avoid introducing significant damage to the material. Nevertheless, the energy provided is adequate to further order and reduce the structure, as evidenced by morphological and quality studies. Moreover, the wettability tests suggest that, alongside the reduction process indicated by the increased porosity of the resulting laser induced graphene (LIG), new oxygen-containing groups are introduced. The photothermal effects induce a surface temperature rise, causing the oxygen in the air to react with the carbon in the substrate, leading to a decrease in the contact angle of the material.

Instead, farther from the focal plane a lower energy is delivered onto the surface of the precursor. The initial pass thus results in a completely amorphous material containing both sp^3 and sp^2 hybridized carbon atoms. The subsequent, faster pass supplies the necessary thermal energy to reorganize the material into a more ordered structure, ultimately producing graphene oxide.

However, it is important to stress the distinction between cellulose acetate and synthetic aromatic polymers in the context of LIG production. Cellulose acetate does not inherently contain sp^2-hybridized carbon atoms. In this substrate, the formation of sp^2 bonds (carbonization) and organization into hexagonal aromatic rings (graphitization) solely occurs due to the laser interaction and the induced heating effects. In contrast, polymers like Kapton®, already possessing aromatic rings in their polymer backbone, facilitate the process. In these cases, laser writing primarily removes functional groups, allowing for the formation of a graphenic 2D material with greater ease and efficiency. This fundamental difference is the reason why, in the case of CA, the double-pass laser technique was necessary to achieve effective graphitization.

4.3 Supercapacitor proof-of-concept

As discussed in the previous section, the optimal distance from the focal plane for producing high-quality LIG was determined to be -3 mm. This material exhibited not only superior quality, as evidenced by Raman spectroscopy, but also significant porosity, as evidenced by SEM imaging, making it highly suitable for supercapacitive applications. The porous structure facilitates effective ion accommodation, and its hydrophilic nature enhances electrode wettability when using a water-based electrolyte. For application as a supercapacitor electrode, the design was developed to maximize the contact area between the electrode and the electrolyte. In the case of a symmetric supercapacitor, the geometry that best achieves this is an interdigitated configuration. The samples were laser-written so that the fingers were oriented parallel to the lasing direction, as previous measurements using the Van der Pauw method indicated that this alignment minimized the resistivity of the material.

4.3.1 First supercapacitor proof-of-concept

The initial tests on proof-of-concept supercapacitors were performed at the ISOM laboratories using cyclic voltammetry (CV) and galvanostatic charge-discharge (GCD) in a two-electrode configuration. The device was fabricated following the procedure detailed in Section 3.1.5. Briefly, silver paste was applied to the symmetric interdigitated CA-LIG electrodes to establish electrical contacts. Conductive copper adhesive tape was then placed on the contact pads, and a protective pool of epoxy adhesive was applied to prevent copper exposure to the electrolyte and its corrosion. H_2SO_4 1M was subsequently introduced.

The device was connected to a potentiostat / galvanostat using alligator clips, as shown in the zoom-in of *Figure 4.30*. Cyclic voltammetry (CV) tests were conducted with scan rates ranging from 0.01 V s^{-1} to 0.2 V s^{-1}, and galvanostatic charge-discharge (GCD) tests were performed with current densities varying from 0.015 mA cm^{-2} to 0.030 mA cm^{-2}.

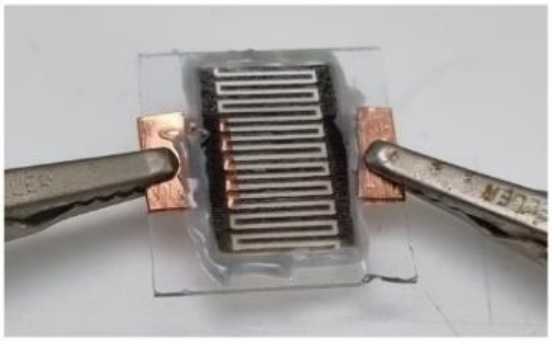

***Figure 4.30**: Zoomed top view of the supercapacitor prototype connected to the testing machine. It is possible to see the pool made of epoxy adhesive used to prevent any electrolyte contact with the metallic collectors made of copper tape.*

The cyclic voltammetry (CV) curves of the fabricated device, as presented in *Figure 4.31*, demonstrate that the current response increases proportionally with the scan rate. This behavior is attributed to a greater number of ions being driven toward and accumulating within the porous electrodes. Despite this, the CV curves retain a pseudo-rectangular shape, characteristic of electric double-layer capacitance behavior. However, at higher scan rates, the resistive contribution becomes more significant, as evidenced by the delayed current response at the extremes of the chosen potential window, particularly at the points of potential reversal.

The experimental measurements were initially presented with current on the vertical axis. In supercapacitor research, parameters such as capacitance, energy density, and power are typically expressed per unit area. Therefore, the current was normalized by the total electrode area, which was measured as 1.87 cm^2 using an optical microscope. This step was essential due to the transfer of the electrode geometry onto the cellulose acetate membrane and the subsequent removal of unconverted membrane material. As a result, the vertical axis of the CV curves represents the current density.

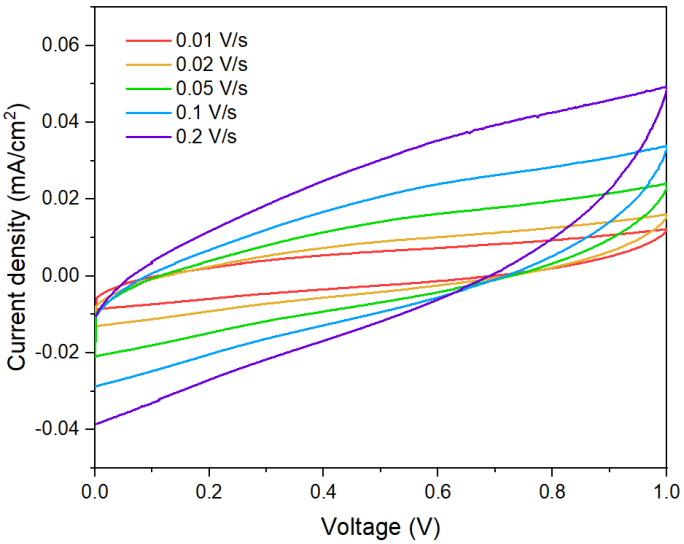

Figure 4.31: *Cyclic voltammetry graphs at different scan speeds, from 0.01 V s^{-1} to 0.2 V s^{-1}.*

This performance is consistent with that expected from bare LIG electrodes. However, the inclined shape and noticeable deviation from the ideal rectangular profile of CV curves reveal the presence of significant resistive characteristics, in line with sheet resistivity results obtained via the Van der Pauw method. A similar behavior was found in literature for flexible supercapacitors obtained from kraft lignin [110].

The galvanostatic charge-discharge (GCD) curves obtained at various current densities, shown in *Figure 4.32*, display a near-triangular shape, confirming effective ion deposition at the electrolyte-electrode interface.

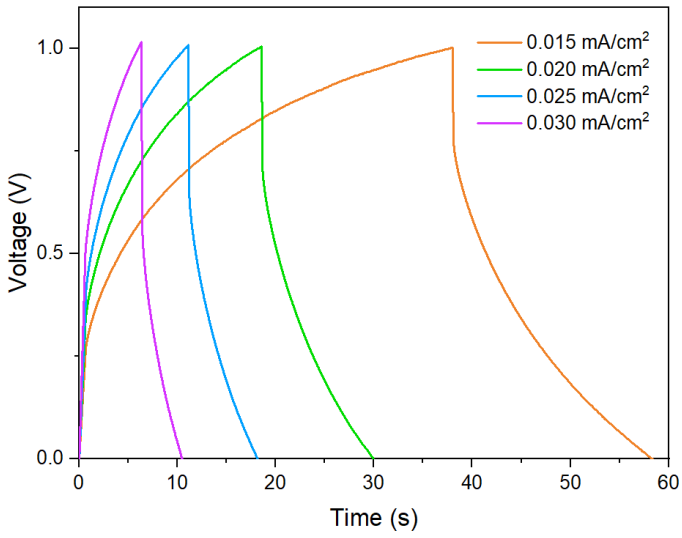

Figure 4.32: *Galvanostatic charge and discharge curves obtained at different current densities.*

The nearly linear charge and discharge profiles confirm the capacitive behavior of the device. However, this linearity diminishes more and more when increasing the current density due to the influence of non-negligible leakage currents. The curves deviate from an ideal triangular form, showing asymmetry due to the intrinsic resistance of the electrodes, particularly visible in the voltage drop at the beginning of each discharge process.

Areal capacitance (C_A) values were extrapolated from the GCD curves as described by *Equation 7* (Section 3.2.6). The device initially exhibits an average capacitance of 0.42 mF cm^{-2} at the lowest current density, decreasing to 0.25 mF cm^{-2} at a current density of 0.03 mA cm^{-2}. These values, plotted as a function of current density in *Figure 4.33*, demonstrate a clear trend: C_A decreases with increasing current density. This behavior is primarily attributed to the resistive characteristics of the electrodes, which dissipate more energy and reduce the stored energy. Additionally, it should be noted that slower measurements, which reduce the current passing through the device, allow more time for ions within the device to migrate and arrange, thus resulting in higher capacitance values. The decline in capacitance with increasing current density underscores the impact of resistive losses and ion transport limitations within the electrode material, highlighting areas for potential optimization in future device designs.

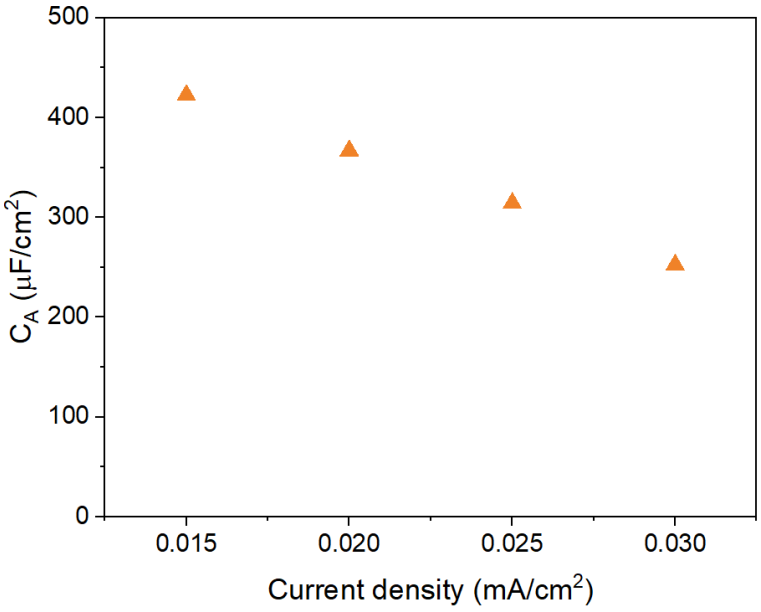

Figure 4.33: *Specific areal capacitance as a function of current density.*

By applying *Equations 8* and *9* from Section 3.2.5, the areal energy density and areal power density values were derived from the GCD curves, as illustrated in the Ragone plots in *Figure 4.34.*

This behavior is primarily attributed to the resistive characteristics of the electrodes, which dissipate more energy and reduce the stored energy. Additionally, it should be emphasized that slower measurement rates, which result in a lower current passing through the device, provide more time for ions to migrate and arrange within the electrode structure. This leads to the observation of phenomena that are not detectable at higher scan rates and results in higher capacitance values. The decline in capacitance with increasing current density underscores the impact of resistive losses and ion transport limitations within the electrode material, highlighting areas for potential optimization in future device designs.

By applying *Equations 8* and *9* from Section 3.2.5, the areal energy density and areal power density values were derived from the GCD curves, as illustrated in the Ragone plots in *Figure 4.34.*

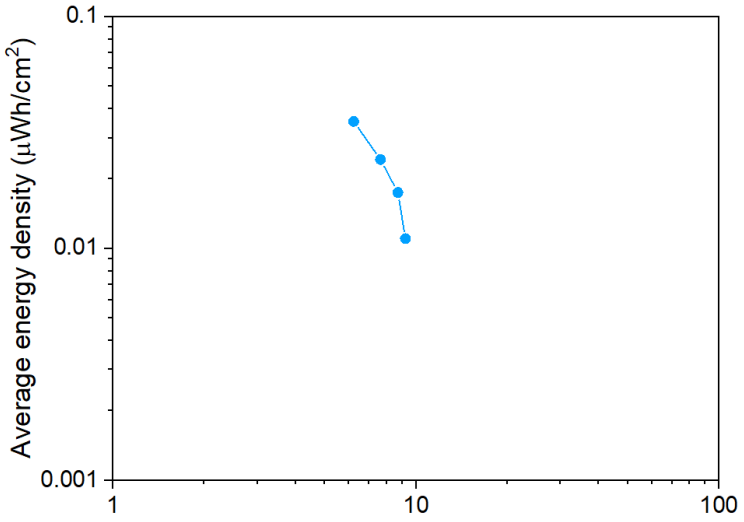

Figure 4.34: *Areal-specific Ragone plot for the realized prototype. Areal energy and power densities were extracted from the GCD curves.*

These metrics enable a comparative analysis of the device performance in terms of energy density and power output against some values reported in the literature for green substrates, as it will be presented in the next sections.

4.3.2 Device optimization and electrolyte selection

At the DISAT laboratories, it was subsequently possible to optimize the device by improving the contacts between the electrodes and the current collector, reducing resistance, and testing various aqueous electrolytes. A titanium mesh was used as the current collector, positioned over the non-active area of the electrodes. Additionally, to prevent the evaporation of the electrolyte solvent, a piece of glass fiber soaked in the electrolyte was employed. Before conducting electrochemical tests on the devices using a two-electrode method, three-electrode tests were performed to determine the potential window for the devices operation. Similarly, a titanium mesh was employed as the current collector, with the contact being ensured through the application of pressure.

Three-electrodes configuration: electrode characterization

The electrochemical performance of the electrode material was assessed in a 1 M H_2SO_4 aqueous solution, using a platinum electrode as the counter electrode and a Ag/AgCl electrode saturated with 3 M KCl as the reference electrode.

The EIS results, presented in *Figure 4.35*, indicate a series resistance of 10.89 Ω, as determined by the high-frequency intercept on the Nyquist plot. The inset of the expected linear vertical trend displayed a shift, with a significant mass-diffusion deviation resulting from the electrolyte resistance within the electrode pores in the acidic environment.

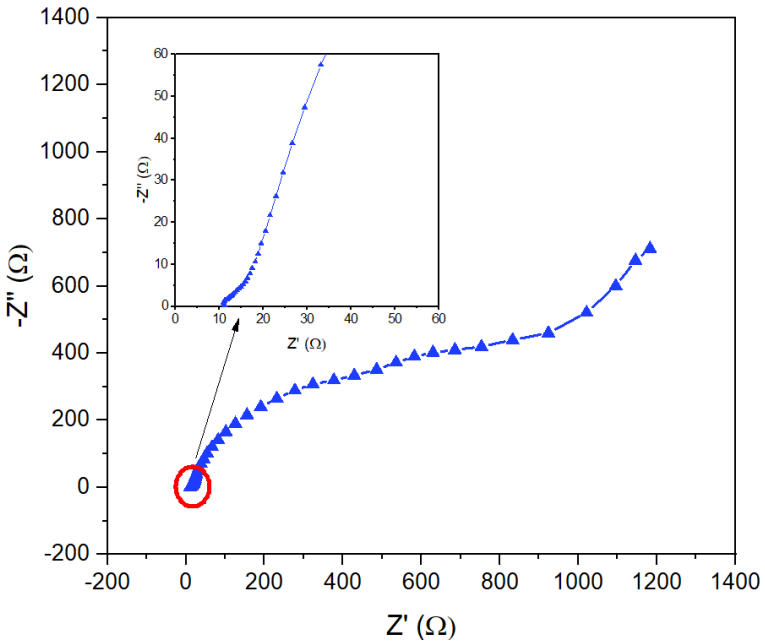

Figure 4.35: *Nyquist plot of a three-electrodes measurement of a supercapacitor in 1M H_2SO_4.*

In order to define the working voltage window of the electrode material, cyclic voltammetry was performed. The voltage window was varied while maintaining a constant scanning rate of 1 mV s^{-1} to ensure the system completed all possible reactions at the electrode/electrolyte interface. *Figure 4.36* displays the obtained curves. A significant drop in current at negative voltages indicates hydrogen evolution while the positive peak at voltages higher than 0.8 V corresponds to oxygen accumulation. To avoid parasitic reactions, the operational window for the system was chosen to be between 0 and 0.8 V.

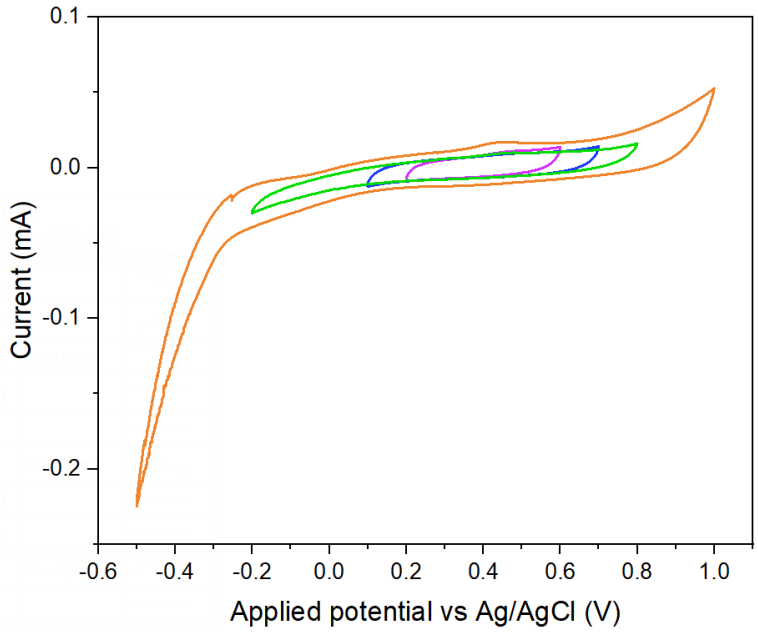

***Figure 4.36**: Cyclic voltammetry curves in three-electrodes configuration at scan rate 1 mV s^{-1} of a supercapacitor in 1M H_2SO_4.*

Two-electrode configuration: device characterization

To assess the performance of the assembled device, a two-electrodes configuration was employed to carry out EIS, CV and GCD techniques. In this setup, the tested system was a symmetrical supercapacitor, with identical reference and working electrodes.

EIS is a valuable technique that help elucidate the interactions between the electrode and the electrolyte in supercapacitors. *Figure 4.37* demonstrates the behavior of supercapacitors in different aqueous electrolytes (1 M KOH, 0.5 M H_2SO_4, and 0.5 M Na_2SO_4) over the applied frequency range. The intercept of the Nyquist plot with the x-axis in the high-frequency region reveals the ohmic resistance known as series resistance R_S. The values obtained for each of the tested electrolytes is displayed in *Table 4.3*. The near-vertical trends observed in the low-frequency region suggest strong capacitive behavior in both basic and acidic

aqueous electrolytes, though some deviations arise due to electrolyte resistance within the electrode pores in the mass-diffusion area. In contrast the device operating in neutral environment shows a less pronounced vertical trend at lower frequencies, indicating weaker capacitive behavior.

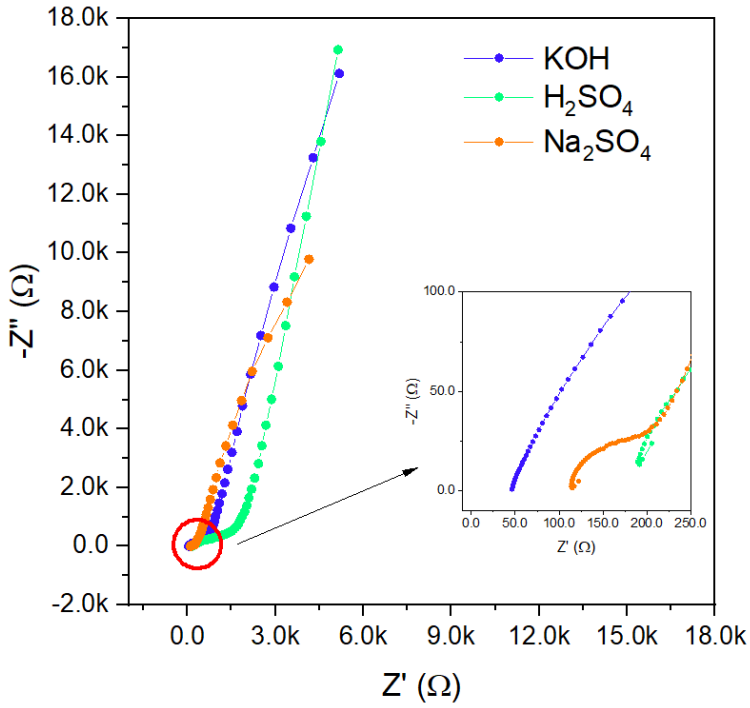

***Figure 4.37**: Nyquist plot of CA-LIG based supercapacitors in different electrolytes, namely 1M KOH, 0.5 H_2SO_4 and 0.5 Na_2SO_4. The inset shows the Nyquist plot magnification.*

***Table 4.3:** Series resistance of the equivalent circuit found for supercapacitors in different electrolytes as the intercepts with the x-axis.*

Electrolyte	R_S (Ω)
1M KOH	44.16
0.5 M H_2SO_4	146.80
0.5 M Na_2SO_4	110.50

In the case of H_2SO_4, the primary distinction compared to the three-electrode configuration is the lower electrolyte concentration, leading to a decreased number of free H^+ and SO_4^{2-} ions available for transport. Furthermore, the influence of factors introduced during device assembly, particularly at the current collector/electrode interface, must be considered, as these can contribute to the overall impedance and consequently impact the electrochemical

performance observed in these measurements. Additionally, the intrinsic resistance of the electrode material itself must be taken into account when evaluating the system's overall behavior.

CVs were performed at scan rates from 5 mV s^{-1} to 100 mV s^{-1} for symmetric supercapacitors in various electrolytes, within the selected voltage window of 0–0.8 V. *Figure 4.38* shows the CV curves for each electrolyte. Within their operating voltage range, supercapacitors exhibit a characteristic rectangular capacitive response. The resistive behavior of H_2SO_4 is evident in the CV curves, displaying slow current responses at the extremities of the voltage window, a behavior similarly observed for Na_2SO_4. In contrast, for KOH the voltage reversal is marked by a more rapid current change, indicating a less resistive response. This is consistent with the results obtained from the EIS spectra.

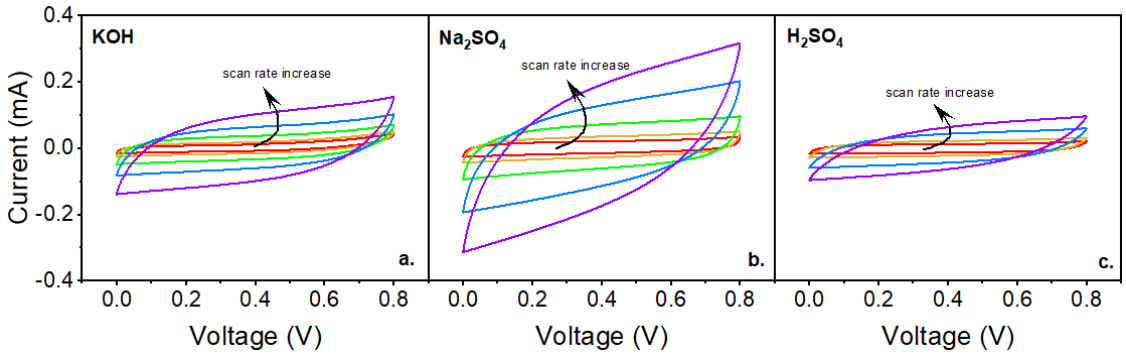

***Figure 4.38**: Cyclic voltammetry curves of supercapacitors at scan rates from 10 mV s^{-1} to 200 mV s^{-1} in various aqueous electrolytes: (a) KOH, (b) Na_2SO_4 (c) H_2SO_4.*

Figure 4.39 compares the CV responses at scan rates of 10 mV s^{-1} and 50 mV s^{-1}. It is evident that increasing the scan rate leads to a slower current response at the voltage reversal points, as seen when comparing *Figure 4.39 (a)* and *Figure 4.39 (b)*. This behavior is consistent across the different electrolytes tested. At slower scan rates, more acidic and neutral electrolytes (H_2SO_4 and Na_2SO_4) exhibited a more rectangular CV shape, while KOH, being more basic, showed a slight peak at positive voltages, likely due to oxygen accumulation. This peak diminished at higher scan rates due to the reduced time available for such reactions. Overall, Na_2SO_4 provided the highest current responses during potential charging. Both H_2SO_4 and Na_2SO_4 demonstrated slower current responses at the reversal points compared to KOH, which maintained a more rectangular CV shape.

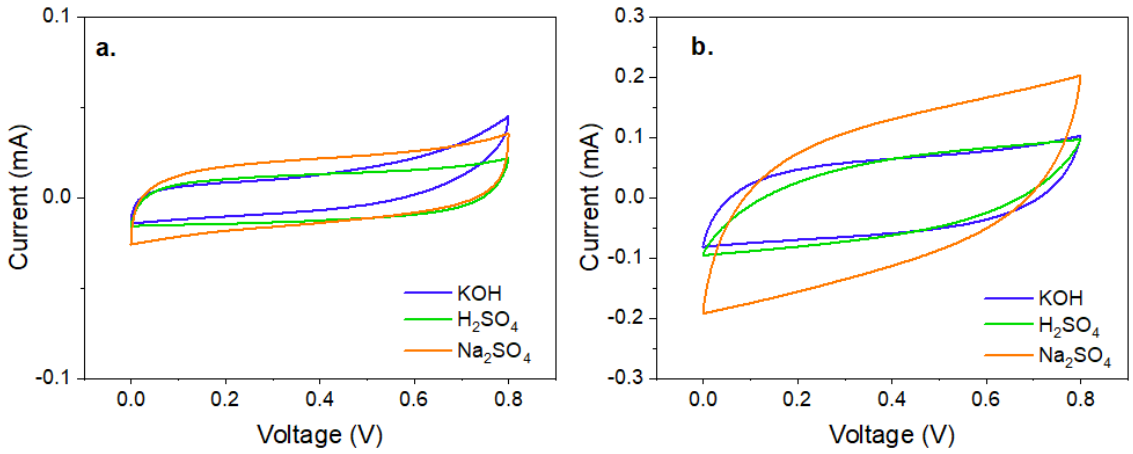

Figure 4.39: *Cyclic voltammetry curves of supercapacitors in various electrolytes at scan rate of (a) 10 mV s^{-1}, (b) 50 mV s^{-1}.*

Figure 4.40 presents the typical galvanostatic charge/discharge (GCD) curves for supercapacitors in various electrolytes, showing almost linear profiles characteristic of capacitive systems, confirming the capacitive nature of the devices. The experiments were conducted using the same current densities across all electrolytes. However, in some cases, the charge/discharge curves at low current densities are not presented due to the extended charging times of the device, where leakage currents became significant relative to the charging process. The galvanostatic charge/discharge (GCD) curves for all three electrolytes exhibit evident asymmetry, which can be attributed to parasitic reactions occurring at the electrode/electrolyte interface. Notably, in the Na_2SO_4 system, a parasitic phenomenon, possibly electrode corrosion resulting from unintended electrolyte contact, was observed.

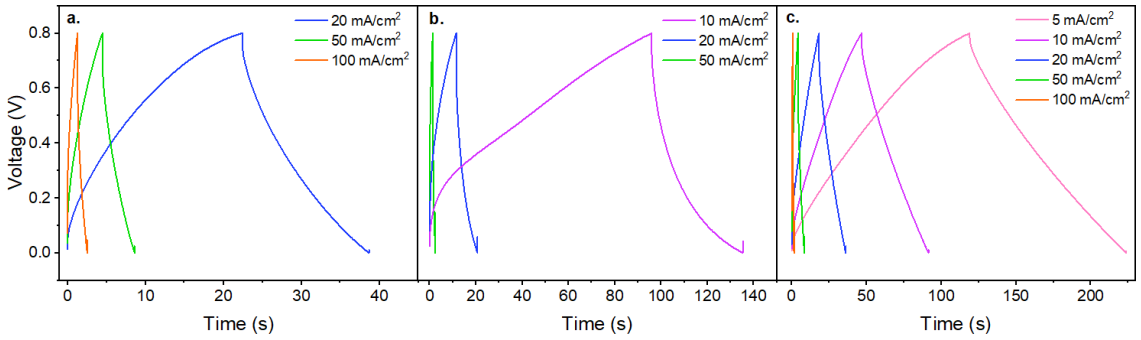

Figure 4.40*: Galvanostatic charge-discharge curves of supercapacitors at different current densities in: (a) 1M KOH, (b) 0.5 Na_2SO_4, (c) 0.5 H_2SO_4.*

A comparison of GCD curves across the three electrolytes at a current density of 50 mA cm^{-2} is shown in *Figure 4.41*. The most symmetric curve corresponds to the basic electrolyte KOH, while Na_2SO_4 exhibited the most significant losses, possibly due to leakage affecting the results, making a direct comparison with the other two systems challenging.

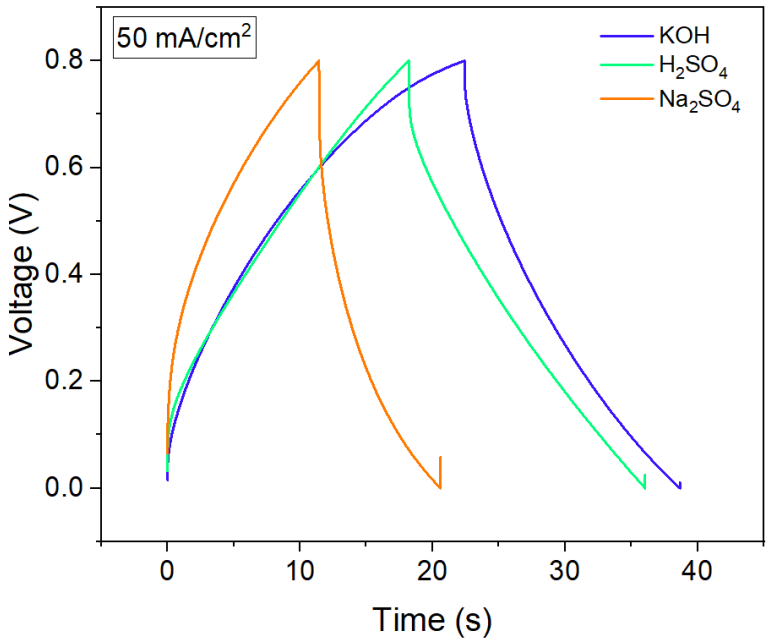

Figure 4.41: *Comparison between galvanostatic charge-discharge curves of supercapacitors in different electrolytes at the current density of 50 mA* cm^{-2}

Using the EC-Lab software, the discharge energy and charge were extracted. From these quantities, the areal capacitance was determined using *Equation 10* from Section 3.2.6. The results are presented in *Figure 4.42*. The neutral environment provided by Na_2SO_4 appears to lead to a significant reduction in device capacitance. It is important to highlight that the experiments conducted with this electrolyte were affected by unwanted contact between the electrolyte and the current collector, as previously discussed. In contrast, when comparing the basic (KOH) and acidic (H_2SO_4) environments, it is evident that the areal capacitance is nearly comparable, with only a slight difference observed at a current density of 50 mA cm^{-2}.

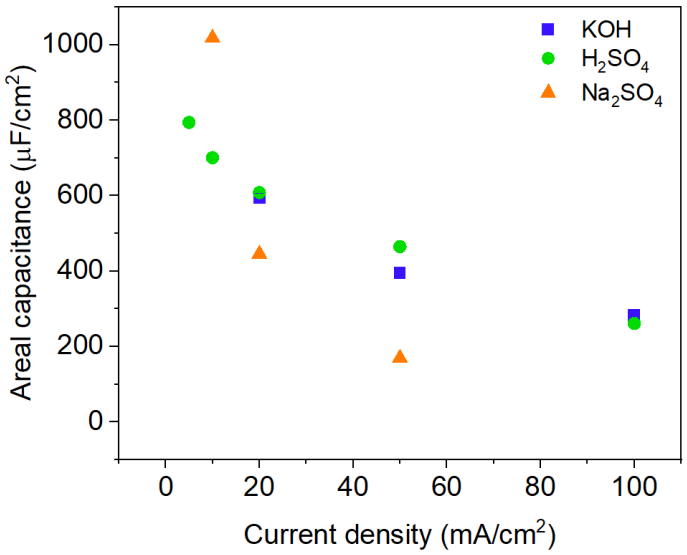

Figure 4.42: *Areal capacitance versus current densities of supercapacitors in different electrolytes.*

By using the discharge time extracted through the software and incorporating it into *Equation 11* in Section 3.2.6, it was possible to determine the power density. This enabled the construction of a Ragone plot, as shown in *Figure 4.43*, through which a comparison of the performance of supercapacitors using different electrolytes was performed. It can be observed that in a basic environment, the device exhibits lower performance in both power density and energy density. In contrast, when comparing KOH and H_2SO_4, very similar trends can be observed. This similar behavior can be attributed to the high ionic mobilities and conductivities of these two electrolytes, which likely play a significant role in the observed electrochemical performance

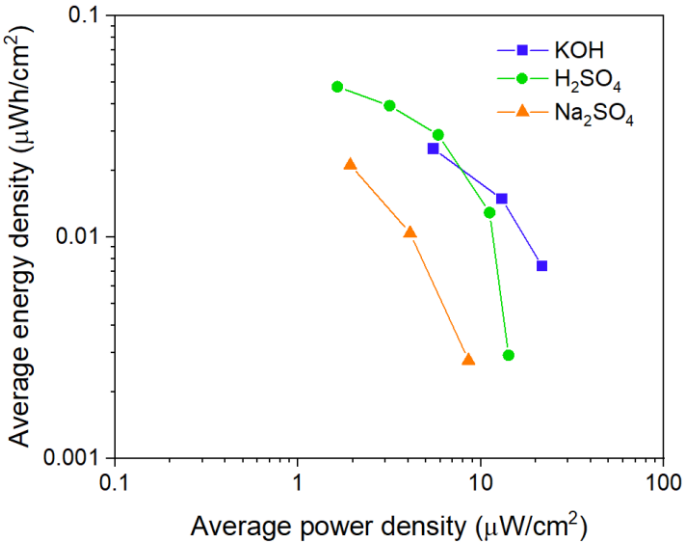

Figure 4.43: *Ragone plot for supercapacitors using different aqueous electrolytes.*

4.3.3 Comparison

Power density and energy density are fundamental parameters for evaluating and comparing the performance of electrochemical devices. In this case, these values allowed for a comparison between the results obtained from two configurations: the first one developed at ISOM and the second at DISAT using different electrolytes, along with data from supercapacitors reported in the literature that were fabricated with LIG sourced from natural resources. The data collected from the literature are presented in *Table 4.4*.

Table 4.4: *Performances of LIG-based supercapacitors produced from sustainable substrates. [a] PEO: Poly (ethylene oxide); PVA: Poly (vinyl alcohol); fs: femtosecond; N.A.: not available. [b] extracted from figures.*

Precursor	Laser type	Electrolyte	C_A (mF cm^{-2})	E_A (µWh cm^{-2})	P_A (µW cm^{-2})	Ref.
Kraft lignin + PEO[a]	CO_2 (10.6 µm)	H_2SO_4/ PVA[a]	2.51	0.31	13.8	[110]
Agglomerated cork	Fiber laser (1.06 µm)	H_2SO_4/ PVA[a]	≈ 2[b]	≈ 0.2[b]	≈ 10[b]	[56]
Bamboo	fs[a] laser (522 nm)	Agarose/ NaCl	2.8	0.3	N.A.[a]	[117]
Chromatography paper	CO_2 (10.6 µm)	H_2SO_4/ PVA[a]	4.6	0.3	4.5	[118]

Ragone plot is shown in *Figure 4.44*. As it can be immediately observed from the Ragone plot, the performance of the supercapacitors fabricated using LIG derived from CA is approximately one order of magnitude lower than the values reported in the literature. However, it is important to consider the use of aqueous electrolytes in this case, which consequently limit the working potential window. Nevertheless, this comparison also highlights the significant potential for improvement that this material and system can offer.

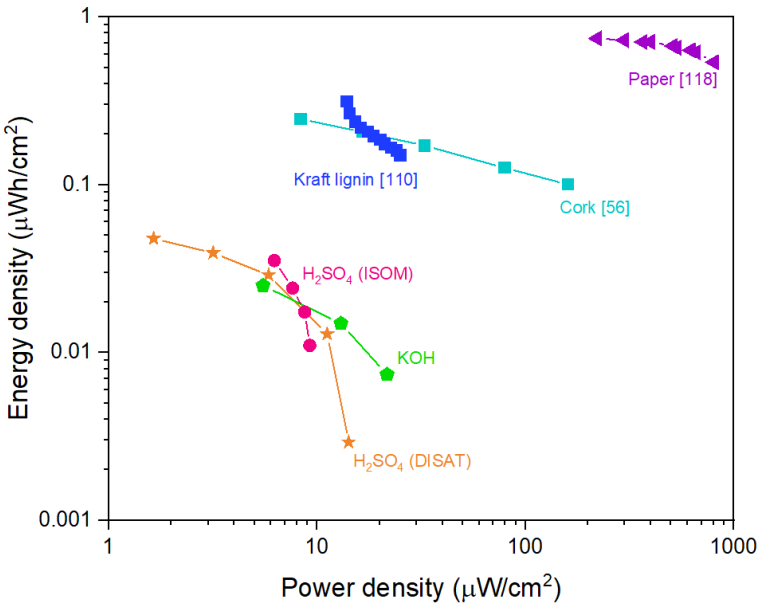

Figure 4.44: *Ragone plot for supercapacitors reported in the literature and for the devices developed in this study.*

5. Conclusions and future prospects

This thesis demonstrated a comprehensive approach for the fabrication and characterization of laser induced graphene (LIG) produced from a novel, green precursor, cellulose acetate, using a hobby-grade CO_2 laser. Additionally, it was shown that this material can be utilized in real applications by providing a prototype supercapacitor as proof-of-concept.

The initial phase involved using a known polymeric substrate, commercially known as Kapton®, to conduct a tilted angle test. This test accurately determined the focal plane distance from the base of the laser to be 7.5 ± 0.05 mm. Establishing this distance was crucial as the substrate distance from the focal plane significantly influences the energy delivered per unit area on the sample surface. To understand the impact of focal distance, laser power, and scanning speed on the material properties, tests were conducted on Kapton® by varying one parameter at a time while keeping the others constant. Results indicated that varying speed and power at different lasing planes optimizes material properties based on desired characteristics. Greater distances from the focal plane yielded more homogeneous LIG, while closer distances resulted in lower sheet resistivity (45 Ω/sq). Higher powers and lower scanning speeds induced greater transformation and better electrical properties, but excessive parameters led to material damage and defect introduction.

Insights from Kapton® studies enabled a better understanding of the transformation mechanism when applying the laser writing process to cellulose acetate, a new sustainable substrate. Commercial membranes demonstrated that cellulose acetate can be effectively converted to LIG. Given its cellulosic nature, using a flame retardant and a double-pass technique was crucial, confirming literature findings from similar precursors. Raman spectroscopy, scanning electron microscopy, Van der Pauw method, and wettability tests clarified the conversion process. The flame retardant prevented material combustion and the formation of volatile carbonaceous by-products. The initial writing pass converted sp^3-hybridized carbon in CA's cyclic structures to sp^2-sp^3 hybridized carbon clusters, with a degree of order that depended on the proximity to the focal plane. Higher energy densities produced more ordered, dense, and less porous material resembling graphene oxide. Greater distances, instead, resulted in more disordered, amorphous carbon. The second, faster writing pass further ordered and reduced the material, resulting in LIG near the focal plane.

Ambient atmosphere with oxygen led to the introduction of new oxygen-containing groups, indicated by the high hydrophilicity of samples produced in the second pass near the focal plane. The most promising material was produced 3 mm below the focal plane, with laser power at 4.5%, 10 mm s^{-1} for the first pass, and 30 mm s^{-1} for the second pass. The need for defocusing indicates a compromise between sufficient energy for material transformation and maintaining structural integrity with minimal defect introduction, achievable only if energy density is not too high.

Electrical characterizations highlighted a fundamental issue: the thin nature of the samples. This material exhibited non-homogeneous electrical properties in the parallel and perpendicular directions to the writing, producing a sheet resistivity of 416.0 ± 41.5 Ω/sq parallel and 1758.6 ± 49.5 Ω/sq perpendicular to the writing direction.

A proof-of-concept supercapacitor was fabricated using the conditions that produced the material with the best properties. Its performances were evaluated through cyclic voltammetry (CV) and galvanostatic charge-discharge (GCD) tests. Both CV and GCD curves indicated capacitive behavior but deviated from ideal performance due to significant resistive losses. One primary issue may be the incomplete and non-uniform graphitization of the material. Additionally, high porosity, while beneficial for ion accommodation, might decrease conductive pathways within the material. Other factors contributing to device resistivity included the type of electrolyte used and the electrode-electrolyte and electrode-metal collector interfaces. These issues were partially addressed by changing the type of contact between the current collector and the electrode and performing tests in different aqueous electrolytes. This approach led to an improved capacitive behavior with reduced resistive components and revealed distinct behaviors across the various electrolyte solutions.

Using Ragone plots, it was possible to conclude that the system exhibiting the highest power development was the one operating in a basic environment, achieving a power density of approximately 20 μW cm^{-2}. Comparison through this type of representation with similar devices found in the literature further demonstrated the potential of this material as an electrode material for supercapacitors.

Finally, this comprehensive approach highlighted the potential of cellulose acetate-derived LIG for energy storage applications while identifying key areas for further optimization to enhance performance. The primary topics worth investigating include:

- **Material Optimization:** To achieve higher capacitance, energy, and power values, it is crucial to minimize resistive losses by improving the quality of the electrode material. Further optimization of LIG, possibly using thicker membranes, could enable higher power usage and result in a more homogeneous material.
- **Device Design:** Optimizing electrode design and electrolyte selection is vital. In supercapacitors, electrode design significantly impacts device performance, and the ionic mobility and viscosity of the electrolyte are crucial for device capacitance. A potential approach for future optimization would involve increasing the thickness of the electrode fingers and reducing the distance between them, thereby minimizing parasitic resistances. Additionally, employing a gel electrolyte could enhance performance by expanding the working potential window.
- **Flexibility:** Future research should focus on optimizing LIG on flexible substrates. While the solid glass support plates facilitated easy manipulation and reduced sample variability in this work, they eliminated the inherent flexibility of LIG. Transferring LIG to stretchable and deformable substrates, such as PDMS, could enable the development of devices that combine energy storage with deformation or bending sensing capabilities.

6. Appendix

A1: *Detailed laser conditions for samples fabricated in the second phase of experimentation. All samples were irradiated 3 mm below the focal plane. Samples marked with (*) are the ones that were fully characterized with Raman spectroscopy, SEM imaging and Van der Pauw conductivity measurements.*

Sample	Power (%)	Speed (mm s^{-1})	Sample	Power (%)	Speed (mm s^{-1})
S-4.5-10	4.5	10	S-6.0-40 (*)	6.0	40
S-4.5-20	4.5	20	S-6.0-50	6.0	50
S-4.5-30	4.5	30	S-6.0-60	6.0	60
S-4.5-40	4.5	40	S-6.0-70	6.0	70
S-4.5-50	4.5	50	S-6.0-80	6.0	80
S-4.5-60	4.5	60	S-6.0-90	6.0	90
S-4.5-70	4.5	70	S-6.0-100	6.0	100
S-4.5-80	4.5	80	S-6.0-110	6.0	110
S-4.5-90	4.5	90	S-6.0-120	6.0	120
S-5.0-10 (*)	5.0	10	S-6.5-40	6.5	40
S-5.0-20	5.0	20	S-6.5-50	6.5	50
S-5.0-30	5.0	30	S-6.5-60	6.5	60
S-5.0-40 (*)	5.0	40	S-6.5-70	6.5	70
S-5.0-50	5.0	50	S-6.5-80	6.5	80
S-5.0-60	5.0	60	S-6.5-90	6.5	90
S-5.0-70 (*)	5.0	70	S-6.5-100	6.5	100
S-5.0-80	5.0	80	S-6.5-110	6.5	110
S-5.0-90	5.0	90	S-6.5-120	6.5	120
S-5.5-10	5.5	10	S-7.0-40 (*)	7.0	40
S-5.5-20	5.5	20	S-7.0-50	7.0	50
S-5.5-30	5.5	30	S-7.0-60	7.0	60
S-5.5-40	5.5	40	S-7.0-70	7.0	70
S-5.5-50	5.5	50	S-7.0-80	7.0	80
S-5.5-60	5.5	60	S-7.0-90	7.0	90
S-5.5-70	5.5	70	S-7.0-100	7.0	100
S-5.5-80	5.5	80	S-7.0-110	7.0	110
S-5.5-90	5.5	90	S7.0-120	7.0	120

Table A2: *Detailed laser conditions for samples fabricated using commercial CA membranes. All samples were irradiated with a lasing power of 4.5% (1.8 W). Sample names indicate the plane of irradiation and scanning speed used for first and second pass. Samples marked with (*) are the ones that were fully characterized with Raman spectroscopy, SEM imaging, Van Der Pauw measurements and contact angle measurement.*

Sample	Speed		Base thickness (mm)
	1st pass	2nd pass	
S2-7.5-11	10		
S2-7.5-21	20	10	
S2-7.5-31	30		
S2-7.5-12	10		
S2-7.5-22	20	20	7.5
S2-7.5-32	30		
S2-7.5-13	10 (*)		
S2-7.5-23	20	30	
S2-7.5-33	30		
S2-4.5-11	10		
S2-4.5-21	20	10	
S2-4.5-31	30		
S2-4.5-12	10		
S2-4.5-22	20	20	4.5
S2-4.5-32	30		
S2-4.5-13	10 (*)		
S2-4.5-23	20	30	
S2-4.5-33	30		

Sample	Speed		Base thickness (mm)
	1st pass	2nd pass	
S2-3.5-11	10		
S2-3.5-21	20	10	
S2-3.5-31	30		
S2-3.5-12	10		
S2-3.5-22	20	20	3.5
S2-3.5-32	30		
S2-3.5-13	10 (*)		
S2-3.5-23	20	30	
S2-3.5-33	30		
S2-0-11	10		
S2-0-21	20	10	
S2-0-31	30		
S2-0-12	10		
S2-0-22	20	20	0
S2-0-32	30		
S2-0-13	10 (*)		
S2-0-23	20	30	
S2-0-33	30		

7. References

[1] United Nations, Causes and Effects of Climate Change, *Climate Action*: https://www.un.org/en/climatechange/science/causes-effects-climate-change

[2] United Nations, For a livable climate: Net-zero commitments must be backed by credible action, *Climate Action*: https://www.un.org/en/climatechange/net-zero-coalition

[3] United Nations, The Paris Agreement, *Climate Action*: https://www.un.org/en/climatechange/paris-agreement

[4] United Nations, A Beginner's Guide to Climate Neutrality, *Climate Change*: https://unfccc.int/news/a-beginner-s-guide-to-climate-neutrality

[5] European Commission, Energy storage: https://energy.ec.europa.eu/topics/research-and-technology/energy-storage_en

[6] F. Bu, W. Zhou, Y. Xu, Y. Du, C. Guan, W. Huang, 2024, Recent Developments of Advanced Micro-Supercapacitors: Design, Fabrication and Applications, *npj Flexible electronic* **4**, 31.

[7] K.C.S. Lakshmi, B. Vedhanarayanan, 2023, High-Performance Supercapacitors: A Comprehensive Review on Paradigm Shift of Conventional Energy Storage Devices, *Batteries* **9** (4), 202.

[8] Z. Sun, S. Fang, 2020, 3D Graphene Materials: from Understanding to Design and Synthesis Control, *Chemical Reviews* **120** (18), 10336-10453.

[9] Y. Wang, Z. Shi, Y. Huang, Y. Ma, C. Wang, M. Chen, Y. Chen, 2009, Supercapactor Devices Based on Graphene Materials, *The Journal of Physical Chemistry* **113** (30), 13103-13107.

[10] K. Avinash, F. Patolsky, 2023, Laser-Induced Graphene Structures: from Synthesis and Applications to Future Prospects, *Materials today* **70**, 104-136.

[11] A.C. Bressi, A. Dallinger, Y. Steksova, F. Greco, 2023, Biodervied Laser-Induced Graphene for Sensors and Supercapacitors, ACS *Applied Materials and Interfaces* **15** (30), 35788-35814.

[12] Y. Chyan, R. Ye, Y. Li, S. P. Singh, C. J. Arnusch, J.M, Tour, 2018, Laser-Induced Graphene by Multiple Lasing: Toward Electronics on Cloth, Paper, and Food, *ACS Nano* **12** (3), 2176-2183.

[13] European Commission, Circular economy action plan: https://environment.ec.europa.eu/strategy/circular-economy-action-plan

[14] World Health Organization: https://www.who.int/news/item/31-05-2022-who-raises-alarm-on-tobacco-industry-environmental-impact

[15] M. Conradi, J. E. Sánchez-Moyano, 2022, Towards a Sustainable Circular Economy for Cigarette Butts, the Most Common Waste Worldwide on the Coast, *Science of the Total Environment* **847,** 157634.

[16] D.S. Green, B.C. Almroth, R. Altman, M. Bergmann, S. Gündoğdu, A.K. Warrier, B Boots, T.R. Walker, A. Krieger, K. Syberg, 2023, Time to Kick the Butt of the Most common Litter Item in the World: Ban Cigarette Filters, *Science of the Total Environment* **865**, 161256.

[17] A.C. Ferrari, F. Bonaccorso, V. Fal'ko, KS. Novoselov, S. Roche, P. Bøggild, S. Borini, F.H.L. Koppens, V. Palermo, N. Pugno, J.A. Garrido, R. Sordan, A. Bianco, L. Ballerini, M. Prato, E. Lidorikis, J. Kivioja, C. Marinelli, T. Ryhänen, A. Morpurgo, J.N. Coleman, V. Nicolosi, L. Colombo, A. Fert, M. Garcia-Hernandez, A. Bachtold, G.F. Schneider, F. Guinea, C. Dekker, M. Barbone, Z. Sun, C. Galiotis, A.N.G. Konstantatos, A. Kis, M. Katsnelson, L. Vandersypen, A. Loiseau, V. Morandi, D. Neumaier, E. Treossi, V. Pellegrini, M. Polini, A. Tredicucci, G.M. Williams, B.H. Hong, J.H. Ahn, J.M. Kim, H. Zirath, B.J. van Wees, H. van der Zant, L. Occhipinti, A. Di Matteo, I.A. Kinloch, T. Seyller, E. Quesnel, X. Feng, K. Teo, N. Rupesinghe, P. Hakonen, S.R.T. Neil, Q. Tannock, T. Löfwanderaq, J. Kinaretba, 2015, Science and Technology Roadmap for Graphene, Related Two-Dimensional Crystals, and Hybrid Systems, *Nanoscale* **7** (11), 4598-4810.

[18] C. Backes, A.M. Abdelkader, C. Alonso, A. Andrieux-Ledier, R. Arenal, J. Azpeitia, N. Balakrishnan, L. Banszerus, J. Barjon, R. Bartali, 2020, Production and Processing of Graphene and Related Materials, *2D Materials* **7** (2), 022001.

[19] P.I.C. Claro, T. Pinheiro, S.L. Silvestre, A.C. Marques, J. Coelho, J.M. Marconcini, E. Fortunato, L.H. Mattoso, R. Martins, 2022, Sustainable Carbon Sources for Green Laser-Induced Graphene: A Perspective of Fundamental Principles, Applications and Challenges, *Applied Physics Reviews* **9**, 041305.

[20] J. Zhu, X. Huang, W. Song, 2021, Physical and Chemical Sensors on the Basis of Laser-Induced Graphene: Mechanisms, Applications, and Perspectives, *ACS Nano* **15** (12), 18708-18741.

[21] S. Nasir, M.Z. Hussein, Z. Zainal, N.A. Yusof, 2018, Carbon-Based Nanomaterials/Allotropes: A Glimpse of their Synthesis, Properties and Some Applications, *Materials* **11** (2), 295.

[22] H.W. Kroto, J.R. Heath, S.C. O'Brien, R.F. Curl, R.E. Smalley, 1985, C60: Buckminsterfullerene, *Nature* **318**, 162–163.

[23] S. Iijima, 1991, Helical Microtubules of Graphitic Carbon, *Nature* **354**, 56–58.

[24] K.S. Novoselov, A.K. Geim, S.V. Morozov, D. Jiang, Y. Zhang, S.V. Dubonos, I.V. Grigorieva, A.A. Firsov, 2004, Electric Field Effect in Atomically Thin Carbon Films. *Science* **306** (5696), 666-669.

[25] N.D. Mermin, 1968, Crystalline Order in Two Dimensions. *Physical Review* **176**, 1, 250-253.

[26] F. M. Vivaldi, A. Dallinger, A. Bonini, N, Poma, L. Sembranti, D. Biagini, P. Salvo, F. Greco, F. Di Francesco, 2021, Three-Dimensional (3D) Laser-Induced Graphene: Structure, Properties, and Application to Chemical Sensing, *ACS Applied Materials & Interfaces* **13** (26), 30245-30260.

[27] C. Lee, X. Wei, J.W. Kysar, J. Hone, 2008, Measurement of Elastic Properties and Intrinsic Strength of Monolayer Graphene, *Science* **321** (5887), 385-388.

[28] J. Kang, W. Cao, X. Xie, D. Sarkar, W. Liu, K. Banerjee, 2014, Graphene and Beyond-graphene 2D Crystals for Next Generation Green Electronics, *Micro- and Nanotechnology Sensors, Systems, and Applications VI* **9083**, 908305.

[29] A.A. Balandin, S. Ghosh, 2008, Superior Thermal Conductivity of Single-Layer Graphene, *Nano Letters* **8**, 3, 902-907.

[30] Z. Sun, D.K. James, J.M. Tour, 2011, Graphene Chemistry: Synthesis and Manipulation, *The Journal of Physical Chemistry Letters* **2** (19), 2380-2510.

[31] P.T. Araujo, M. Terrones, M.S. Dresselhaus, 2012, Defects and Impurities in Graphene-like Materials, *Materials Today* **15**, 3, 98-109.

[32] L. Jiang, Z. Fan, 2014, Design of Advanced Porous Graphene Materials: from Graphene Nanomesh to 3D Architectures, *Nanoscale* **6**, 1922-1945.

[33] N. Kumar, R. Salehiya, V. Chauke, O.J. Botlhoko, K. Setshedi, M. Scriba, M. Masukume, S.S. Ray, 2021, Top-down Synthesis of Graphene: A Comprehensive Review, *FlatChem* **27**, 100224.

[34] A. L. Olatomiwa, T. Adam, S.C.B. Gopinath, S.Y. Kolawole, O.H. Olayinka, U. Hashim, 2022, Graphene Synthesis, Fabrication, Characterization based on Bottom-up and Top-down Approaches: An Overview, *Journal of Semiconductors* **43** (6), 061101.

[35] C. Botas, P. Alvarez, C. Blanco, R. Santamaría, M. Granda, M.D. Gutierrez, F. Rodríguez-Reinoso, R. Menéndez, 2013, Critical Temperatures in the Synthesis of Graphene-like materials by Thermal Exfoliation-Reduction of Graphite Oxide, *Carbon* **52**, 476-485.

[36] J. Lin, Z. Peng, Y. Liu, F. Ruiz-Zepeda, R. Ye, E.L.G. Samuel, M.J. Yacaman, B.I. Yakobson & J.M. Tour 2014, Laser-Induced Porous Graphene Films Commercial from Polymers. *Nature communications*, **5**, 5714.

[37] A. Vashististh, M. Kowalik, J.C. Gerringer, C. Ashraf, A.C.T. van Duin, M.J. Green, 2020, ReaxFF Simulations of Laser-Induced Graphene (LIG) Formation for multifunctional Polymer Nanocomposites, *ACS Applied Nano Materials* **3** (2), 1881-1890.

[38] Z.T. Johnson, N. Jared, J.K. Peterson, J. Li, E.A. Smith, S.A. Walper, S.L. Hooe, J.C. Breger, I.L. Medintz, C. Gomes, J.C. Claussen, 2022, Enzymatic Laser-Induced Graphene Biosensor for Electrochemical Sensing of the Herbicide Glyphosate, *Global Challenges* **6** (9), 2200057.

[39] A. Beherent, C. Griesche, P. Sippel, A.J. Baeumner, 2021, Process-Property Correlations in Laser-Induced Graphene Electrodes for Electrochemical Sensing, *Microchimica Acta* **188**, 159.

[40] C. Fenzl, P. Nayak, T. Hirsch, O.S. Wolfbeis, H.N. Alshareef, A.J. Baeumner, 2017, Laser-Scribed Graphene Electrodes for Aptamer-Based Biosensing, *ACS Sensors* **2** (5), 616-620.

[41] M.G. Standford, K. Yang, Y. Chyan, C. Kittrell, J.M. Tour, 2019, Laser Induced Graphene for Flexible and Embeddable Gas Sensors, *ACS Nano* **13** (3), 3474-3482.

[42] A. Tiliakos, C. Ceaus, S.N. Iordache, E. Vasile, I. Stamatin, 2016, Morphic Transitions of Nanocarbons via Laser Pyrolysis of Polyimide Films, *Journal of Analytical and Applied Pyrolysis* **121**, 275-286.

[43] H. Tariq, S. U. Awan, D. Hussain, S. Rizwan, S.A. Shah, S. Zainab, M.B. Riaz, 2023, Enhancing Supercapacitor Performance Through Design Optimization of Laser-Induced Graphene and MWCNT Coatings for Flexible and Portable Energy Storage, *Scientific Reports* **13**, 21116.

[44] M. Reina, M. Serrapede, P. Zaccagnini, A. Pedico, M. Castellino, S. Bianco, T. Ouisse, H. Pazniak, J. Gonzalez-Julian, A. Lamberti, 2023, Decoration of Laser Induced Graphene with MXene and Manganese Oxide for Fabrication of a Hybrid Supercapacitor, *Electrochimica Acta* **468**, 143163.

[45] C. Griesche, K. Hoecherl, A.J. Baeumner, 2021, Substrate-Independent Laser-Induced Graphene Electrodes for Microfluidic Electroanalytical Systems, *ACS Applied Nano Materials* **4** (3), 3114-3121.

[46] M. D. Wagh, S. K. Sahoo, S. Goel, 2022, Laser-Induced Graphene Ablated Polymeric Microfluidic Device with Interdigital Electrodes for Taste Sensing Application, *Sensors and Actuators: A. Physical* **333**, 113301.

[47] A. Kaidarova, J. Kosel, 2021, Physical Sensors Based on Laser-Induced Graphene: A Review, *IEEE Sensors Journal* **21**, 11.

[48] T.S.D. Le, H.P. Phan, S. Kwon, S. Park, Y. Jung, J. Min, B.J. Chun, H. Yoon, S.H. Ko, S.-W. Kim, Y.J. Kim, 2022, Recent Advances in Laser-Induced Graphene: Mechanism, Fabrication, Properties, and Applications in Flexible Electronics, *Advanced Functional Materials* **32** (48), 2205158.

[49] Z. Zhang, M. Song, J. Hao, K. Wu, C. Li, C. Hu, 2018, Visible Light Laser-Induced Graphene from Phenolic Resin: A New Approach for Directly Writing Graphene-based Electrochemical Devices on Various Substrates**,** *Carbon* **127,** 287-296.

[50] A. Kothuru, S. Goel, 2020, Laser Induced Graphene on Phenolic Resin and Alcohol Composite Sheet for Flexible Electronics Applications, *Flexible and Printed Electronics* **5**, 042001.

[51] A. K. Thakur, B. Lin, F.H. Nowrin, M. Malmali, 2022, Comparing Structure and Sorption Characteristics of Laser-Induced Graphene (LIG) from Various Polymeric Substrates, *ACS EST Water* **2** (1), 75-87.

[52] J.L. Beckham, J. T. Li, M.G. Stanford, W. Chen, E.A. McHugh, P.A. Advincula, K.M. Wyss, Y. Chyan, W.L. Boldman, P.D. Rack, J.M. Tour, 2021, High Resolution Laser-Induced Graphene from Photoresist, *ACS Nano* **15** (5), 8976-8983.

[53] S. Bai, L. Ruan, H. Chen, Y. Du, H. Deng, N. Dai, Y. Tang, 2024, Laser-Induced Graphene: Carbon Precursors, Fabrication Mechanisms, Material Characteristics, and Applications in Energy Storage, *Chemical Engineering Journal,* **493**, 152805.

[54] BioRender library: https://www.biorender.com/library

[55] S. K. Lengger, L. Neumaier, L. Haiden, M. Feuchter, T. Griesser, J. Kosel, 2024, Laser-Induced Graphene Formation on Different Wood Species: Dependence of Electronic

Performances on Intrinsic Features of Certain Types of Wood, *Sustainable Materials and Technologies*, **40**, 00936.

[56] S. L. Silvestre, T. Pinheiro, A.C. Marques, J. Deuermeier, J. Coelho, R. Martins, L. Pereira, E. Fortunato, 2022, Cork Derived Laser-Induced Graphene for Sustainable Green Electronics, *Flexible and Printed Electronics* **7**, 035021.

[57] X. Zang, C. Shen, Y. Chu, B. Li, M. Wei, J. Zhong, M. Sanghadasa, L. Lin, 2018, Laser-Induced Molybdenum Carbide–Graphene Composites for 3D Foldable Paper Electronics, *Paper Electronics* **30** (26), 1800062.

[58] Z. Ismail, 2022, Laser Writing of Graphene on Cellulose Paper and Analogous Material for Green and Sustainable Electronic: A Concise Review, *Carbon Letters* **32**, 1227-1245.

[59] B. Kulyk, B.F.R. Silva, A.F. Carvalho, S. Silvestre, A.J.S. Fernandes, R. Martins, E. Fortunato, F.M. Costa, 2021, Laser-Induced Graphene from Paper for Mechanical Sensing, *ACS Applied Materials and Interfaces* **13** (8), 10210-10221.

[60] Y. Yao, X. Duan, M. Niu, J. Luo, R. Wang, T. Liu, 2019, One-step Process for Direct Laser Writing Carbonization of $NH_4H_2PO_4$ Treated Cellulose Paper and its Use for Facile Fabrication of Multifunctional Force Sensors with Corrugated Structures, *Cellulose* **26**, 7423-7435.

[61] Y. Chyan, J. Cohen, W. Wang, C. Zhang, J.M. Tour, 2019, Graphene Art, *ACS Applied Nano Materials* **2** (5), 3007-3011.

[62] B. Kulyk, M. Matos, B.F.R. Silva, A.F. Carvalho, A.J.S. Fernandes, D.V. Evtuguin, E. Fortunato, F.M. Costa, 2022, Conversion of Paper and Xylan into Laser-Induced Graphene for Environmentally Friendly Sensors, *Diamond and related materials* **123**, 108855.

[63] L. Dubrovina, O. Naboka, V. Ogenko, P. Gatenholm, P. Enoksson, 2014, One-pot Synthesis of Carbon Nanotubes from Renewable Resource: Cellulose Acetate, *Journal of Material Science* **49**, 1144-1149.

[64] D. Kim, J. Y. Han, D. Lee, Y. Lee, D.Y. Jeon, 2022, Facile Conversion of a Cellulose Acetate Laminate Film to Graphene by a Lamination Process and Post-annealing, Journal of Materials Chemistry 22, 20026-20031.

[65] J. Fischer, Katrin Thümmler, S. Fischer, I.G. Gonzalez Martinez, S. Oswald, D. Mikhailova, 2021, Activated Carbon Derived from Cellulose and Cellulose Acetate Microspheres as Electrode Materials for Symmetric Supercapacitors in Aqueous Electrolytes, *Energy Fuels* **35** (15), 12653-12665.

[66] M. Chen, J. Li, J. Zhang, Y. Ma, H. Dong, W. Li, E. Bekyarova, Y.F. Al-Hadeethi, L. Chen, M.N. Hedhli, B. Tian, X. Zhang, 2021, Evolution of Cellulose Acetate to Monolayer Graphene, *Carbon* **174**, 24-35.

[67] M. Abdulhafez, G. N. Tomaraei, M. Bedewy, 2021, Fluence-dependent Morphological Transitions in Laser-Induced Graphene Electrodes on Polyimide Substrates for Flexible Devices, *ACS Applied Nano Materials* **4** (3), 2973-2986.

[68] A. Lamberti, F. Perrucci, M. Caprioli, M. Serrapede, M. Fontana, S. Bianco, S. Ferrero, E. Tresso, 2017, New Insights on Laser-Induced Graphene Electrodes for Flexible

Supercapacitors: Tunable Morphology and Physical Properties, *Nanotechnology* **28** (17), 174002.

[69] Y. Li, D. X. Luong, J. Zhang, Y. R. Tarkunde, C. Kittrell, F. Sargunaraj, Y. Ji, C.J. Arnush, J.M. Tour, 2017, Laser-Induced Graphene in Controlled Atmospheres: From Superhydrophilic to Superhydrophobic Surfaces, *Advanced Materials* **29**, 1700496.

[70] L.-Q. Tao, H. Tian, Y. Liu, Z.-Y. Ju, Y. Pang, Y.-Q. Chen, D.-Y. Wang, X.-G. Tian, J.-C. Yan, N.-Q. Deng, T.-L. Ren, 2017, An Intelligent Artificial Throat with Sound-sensing Ability Based on Laser Induced Graphene, *Nature Communications* **8***,* 14579.

[71] R. Drummond, C. Huang, P.S. Grant, S.R. Duncan, 2019, Overcoming Diffusion Limitations in Supercapacitors using Layered Electrodes, *Journal of Power Sources* **433**, 126579.

[72] A. S. Velasco, 2023, Graphene Devices for Renewable Energy Generation and Storage, Doctoral Thesis, Universidad Politécnica de Madrid, Madrid, Spain.

[73] N. Liu, R. Chen*,* Q. Wan, 2019, Recent Advances in Electric-Double-Layer Transistors for Bio-Chemical Sensing Applications, *Sensors* **19** (15), 3425.

[74] J. Zhang, M. Gu, X. Chen, 2023, Supercapacitors for Renewable Energy Applications: A Review, *Micro and Nano Engineering* **21**, 100229.

[75] A. Rao, S. Bhat, S. De, 2024, Binder-free Laser Induced Graphene-MnO_2 Composite Electrodes for High Areal Energy Density Flexible Supercapacitors, *Electrochimica Acta* **487**, 144152.

[76] N. Liu, Y. Gao, 2017, Recent Progress in Micro-supercapacitors with In-plane Interdigital Electrode Architecture, *Small* **13**, 1701989.

[77] S. G. Jo, R. Ramkumar, J.W. Lee, 2024, Recent Advances in Laser-Induced Graphene-Based Materials for Energy Storage and Conversion, *ChemSusChem* **17** (5), e202301146.

[78] M.G. Standford, J.T. Li, Y. Chyan, Z. Wang, W. Wang, J.M. Tour, 2019, Laser-Induced Graphene Triboelectric Nanogenerators, *ACS Nano* **13** (6), 7166-7174.

[79] J. Yi, J. Chen, Z. Yang, Y. Dai, W. Li, J. Cui, F. Ciucci, Z. Lu, C. Yang, 2019, Facile Patterning of Laser-Induced Graphene with Tailored Li Nucleation Kinetics for Stable Lithium-Metal Batteries, *Lithium Metal Batteries* **9** (38), 1901796.

[80] T.R. Cui, Y. C. Qiao, J.-W. Gao, C.-H. Wang, Y. Zhang, L. Han, Y. Yang, T.L. Ren, , 2021, Ultrasensitive Detection of COVID-19 Causative Virus (SARS-CoV-2) Spike Protein Using Laser Induced Graphene Field-Effect Transistor, *Molecules* **26** (22), 6947.

[81] R.R.A. Soares, R.G. Hjort C.C. Pola, K. Parate, E.L. Reis, N.F.F. Soares, E.S. McLamore, J.C. Claussen, C.L. Gomes, 2020, Laser-Induced Graphene Electrochemical Immunosensors for Rapid and Label-Free Monitoring of *Salmonella enterica* in Chicken Broth, *ACS Sensors* **5**, 1900-1911.

[82] S.Y. Xia, Y. Long, Z. Huang, Y. Zi, L.Q. Tao, C.H. Li, J. Li, 2022, Laser-Induced Graphene (LIG)-based Pressure Sensor and Triboelectric Nanogenerator towards High-performance Self-powered Measurement-control Combined System, *Nano Energy* **96** (1), 107099.

[83] Y. Zou, M. Zhong, S. Li, Z. Qing, X. Xing, G. Gong, R. Yan, W. Qin, J. Shen, H. Zhang, Y. Jiang, Z. Wang, C. Zhou, 2023, Flexible Wearable Strain Sensors Based on Laser-Induced Graphene for Monitoring Human Physiological Signals, *Polymers* **15** (17), 3553.

[84] H. Wang, X. Li, X. Wang, Y. Qin, Y. Pan, X. Guo, 2024, Somatosensory Electro-Thermal Actuator through the Laser-Induced Graphene Technology, *Small* **20** (21), 2310612.

[85] A. Kramar, I. R. Ortega, G. González-Gaitano, J. González-Benito, 2023, Solution Casting of Cellulose Acetate Films: Influence of Surface Substrate and Humidity on Wettability, Morphology and Optical Properties, *Cellulose* **30**, 2037-2052.

[86] A. Tenorio-Alfonso, M. C. Sánchez, J.M. Franco, 2017, Preparation, Characterization and Mechanical Properties of Bio-Based Polyurethane Adhesives from Isocyanate-Functionalized Cellulose Acetate and Castor Oil for Bonding Wood, *Polymers* **9** (4), 132.

[87] S. Gaan, L. Mauclaire P. Rupper, V. Salimova, T.T. Tran, M. Heuberger, 2011, Thermal degradation of cellulose acetate in presence of bis-phosphoramidates, *Journal of Analytical and Applied Pyrolysis* **90** (1), 33-41.

[88] L. Wang, S. Su, D. Chen, C.A. Wilkie, 2009, Fire Retardancy of Bis[2-(methacryloyloxy)ethyl] Phosphate Modified Poly(methyl methacrylate) Nanocomposites Containing Layered Double Hydroxide and Montmorillonite, *Polymer Degradation and Stability* **94** (7), 1110-1118.

[89] J. Jang, Y. K. Jeong, 2008, Synthesis and Flame-Retardancy of UV-curable Methacryloyloxy Ethyl Phosphates, *Fibers and Polymers* **9**, 667-673.

[90] ImageJ open-source software: https://imagej.net/ij/

[91] J.R. Ferraro, K. Nakamoto, C.W. Brown, 2003, Introductory Raman Spectroscopy, Chapter 1, 2nd edition, *Elsevier Science & Technology*.

[92] I. Childres, L.A. Jauregui, W. Park, H. Cao, Y.P. Chen, 2013, Raman Spectroscopy of Graphene and Related Materials, Chapter 19.

[93] A. Radoń, P. Włodarczyk, D. Łukowiec, 2018, Structure, Temperature and Frequency Dependent Electrical Conductivity of Oxidized and Reduced Electrochemically Exfoliated Graphite, *Physica E: Low-dimensional Systems and Nanostructures* **99**, 82-90.

[94] J.B. Wu, M.L. Lin, X. Cong, H.N. Liu, P.H. Tan, 2018, Raman Spectroscopy of Graphene-based Materials and its Applications in Related Devices, *Chemical Society Reviews* **47**, 1822-1873.

[95] G. Cummins, M.P.Y. Desmulliez, 2012, Inkjet Printing of Conductive Materials: A Review, *Circuit World* **38**, 4, 193-213.

[96] L.J. Van der Pauw, 1958, A Method of Measuring the Resistivity and Hall Coefficient on Lamellae of Arbitrary Shape, *Philips Technical Review* **20**, 220-224.

[97] L.J. Van Der Pauw, 1958, A Method of Measuring Specific Resistivity and Hall Effect of Discs of Arbitrary Shape, *Philips Research Reports* **13**, 1-9.

[98] D.W. Koon, 1989, Effect of Contact Size and Placement, and of Resistive Inhomogeneities on van der Pauw Measurement, *Review of Scientific Instruments* **60**, 2.

[99] S. Dsoke, X. Tian, C. Täubert, S. Schlüter, M. Wohlfahrt-Mehrens, 2013, Strategies to Reduce the Resistance Sources on Electrochemical Double Layer Capacitor Electrodes, *Journal of Power Sources* **238**, 422-429.

[100] P. Giannakou, 2020, Printed Transition Metal Oxide Electrochemical Capacitors for Energy Harvesting Applications, Doctoral Thesis, University of Surrey, Guildford.

[101] A. Velasco, Y.K. Ryu, A. Hamada, A. de Andrés, F. Calle, J. Martinez, 2023, Laser-Induced Graphene Microsupercapacitors: Structure, Quality, and Performance, *Nanomaterials* **13**, 788.

[102] G. Anemone, E.C. Pascual, H.K. Yu, A. Al Taleb, F. Jiménez-Villacorta, C. Prieto, A.M. Wodtke, A. De André, D. Farías, 2016, Quality of Graphene on Sapphire: Long-Range Order from Helium Diffraction Versus Lattice Defects from Raman Spectroscopy, *RSC Advances* **6**, 21235-21245.

[103] M. F. Sonnenschein, A. M. Kotliar, C. M. Roland, 1990, Poly(Ethylene Terephtalate) Crystallization as a Method for Microlithography, *Polymer Engineering and Science* **30**, 18, 1165-1170.

[104] J. Amim Jr, P. M. Kosaka, D.F.S. Petri, 2008, Characteristics of Thin Cellulose Ester Films Spin-Coated Form Acetone and Ethyl Acetate Solutions, *Cellulose* **15**, 527-535.

[105] S. Stankovich, D.A. Dikin, R.D. Piner, K.A. Kohlhaas, A. Kleinhammes, Y. Jia , Y. Wu, S.B.T. Nguyen, R.S. Ruoff, 2007, Synthesis of Graphene-based Nanosheets via Chemical Reduction of Exfoliated Graphite Oxide, *Carbon* **45**, 1558-1565.

[106] V. Scardaci, G. Compagnini, 2021, Raman Spectroscopy Investigation of Graphene Oxide Reduction by Laser Scribing, *Journal of Carbon Research* **7**, 48.

[107] A. Jiříčková, O. Jankovský, Z. Sofer, D. Sedmidubský, 2022, Synthesis and Applications of Graphene Oxide, *Materials* **15**, 3, 92.

[108] Y. Jung, J. Min, J. Choi, J. Bang, S. Jeong, K. R. Pyun, J. Ahn, Y. Cho, S. Hong, S. Hong, J. Lee, S. H. Ko, 2022, Smart Paper Electronics by Laser-Induced Graphene for Biodegradable Real-Time Food Spoilage Monitoring, *Applied Materials Today* **29**, 101589.

[109] Y. Zhou, B. Wang, X. Song, E. Li, G. Li, S. Zhao, H. Yan, 2006, Control Over the Wettability of Amorphous Carbon Films in a Large Range from Hydrophilicity to Super-Hydrophobicity, *Applied Surface Science* **253**, 2690-2694.

[110] F. Mahmood, H. Zhang, J. Li, C. Wan, 2020, Laser-Induced Graphene Derived from Kraft Lignin for Flexible Supercapacitors, *ACS Omega* **5**, 14611-14618.

[111] M. Iqhrammullah, M. Marlina, H.P.S.A. Khalil, K.H. Kurniawan, H. Suyanto, R. Hedwig, I. Karnadi, N.G. Olaiya, C.K. Abdullah, S.N. Abdulmadjid, 2020, Characterization and Performance Evaluation of Cellulose Acetate–Polyurethane Film for Lead II Ion Removal, *Polymers* **12**, 1317.

[111] B. Chen, Z.T. Johnson, D. Sanborn, R.G. Hjort, N.T. Garland, R.R.A. Soares, B. Van Belle, N. Jared, J. Li, D. Jing, E.A. Smith, C.L. Gomes, J.C. Claussen, 2022, Tuning the Structure, Conductivity, and Wettability of Laser-Induced Graphene for Multiplexed Open Microfluidic Environmental Biosensing and Energy Storage Devices, *ACS Nano* **16**, 15-28.

[112] A. Dallinger, F. Steinwender, M. Gritzner, F. Greco, 2023, Different Roles of Surface Chemistry and Roughness of Laser-Induced Graphene: Implications for Tunable Wettability, *ACS Applied Nano Materials* **6**, 16201-16211.

[113] Y. Li, D. X. Luong, J. Zhang, Y.R. Tarkunde, C. Kittrell, F. Sargunaraj, Y. Ji, C.J. Arnusch, J. M. Tour, 2017, Laser-Induced Graphene in Controlled Atmospheres: from Superhydrophilic to Superhydrophobic Surfaces, *Advanced Materials* **29**, 1700496.

[115] S. Samantha, S. Singh, R.S. Sahoo, 2015, Simultaneous Chemical Reduction and Surface Functionalization of Graphene Oxide for Efficient Lubrication of Steel-Steel Contact, *RSC Advances,* **5**, 61888-61899.

[115] R.N. Wenzel, 1936, Resistance of Solid Surfaces to Wetting by Water, *Industrial & Engineering Chemistry* **28**.

[116] B. Xiong, J. Li, C. He, X. Tang, Z. Lv, X. Li, X. Yan, 2020, Effect of Pore Morphology and Surface Roughness on Wwettability of Porous Titania Films, *Material Research Express* **7**, 115013.

[117] R. Miyakoshi, S. Hayashi, M. Terakawa, 2022, Simultaneous Laser-Based Graphitization and Microstructuring of Bamboo for Supercapacitors Derived from RenewablerResources, *RSC Advances* **12**, 29647.

[118] J. Coelho, R.F. Correia, S. Silvestre, T. Pinheiro, A.C. Marques, M.R.P. Correia, J.V. Pinto. E. Fortunato, R. Martins, 2023, Paper Based Laser Induced Graphene for Sustainable and Flexible Micro-Supercapacitor Applications, *Microchimica Acta* **40**, 190.